Coupling light to periodic nanostructures

Driessen, E.F.C.

Coupling light to periodic nanostructures

Eduard Driessen

Coupling light to periodic nanostructures

Proefschrift

ter verkrijging van
de graad van Doctor aan de Universiteit Leiden,
op gezag van Rector Magnificus prof. mr. P. F. van der Heijden,
volgens besluit van het College voor Promoties
te verdedigen op donderdag 24 september 2009
klokke 13:45 uur

door

Eduard Frans Clemens Driessen

geboren te Utrecht
in 1979

Promotiecommissie:

Promotor:	Prof. Dr. J. P. Woerdman	Universiteit Leiden
Copromotor:	Dr. M. J. A. de Dood	Universiteit Leiden
Leden:	Prof. Dr. G. W. 't Hooft	Philips Research/ Universiteit Leiden
	Dr. Ir. H. L. Offerhaus	Universiteit Twente
	Prof. Dr. M. A. G. J. Orrit	Universiteit Leiden
	Prof. Dr. J. M. van Ruitenbeek	Universiteit Leiden

The work presented in this thesis has been made possible by financial support from the Dutch Organization for Scientific Research (NWO) and is part of the scientific program of the Foundation for Fundamental Research of Matter (FOM).

Casimir PhD Series, Delft-Leiden, 2009-008
ISBN/EAN: 978-90-8593-056-3

Contents

Chapter 1

Introduction

Already since ancient history, mankind has tried to manipulate light and use it for their purpose. The fact that a piece of glass can be used to manipulate light was known by the ancient Greeks, as reports Aristophanes in his comedy "The Clouds" [1], first performed in 423 B.C.:

> Strepsiades You know in a chemist's shop... that round thing... clear, like a pretty stone you can see right through... For fires...
>
> Socrates You mean a magnifying glass?
>
> Strepsiades That's it. I'll take one with me in court... Stand behind the clerk with the wax tablets... And when he writes down the fine, melt it away.
>
> Socrates That's clever. I like it.

Ever since then, a better and better understanding of light went hand in hand with new inventions, that marked new eras of using and manipulating light. The microscope made it possible to look at ever smaller objects, and the invention of the laser marked the era of using light as an information carrier. A final step was made with the advent of nanotechnology. This technology made it possible to structure materials on a scale of hundreds of nanometers, smaller than the wavelength of light.

On the one hand, this possibility opened new routes for fundamental physics research. The (theoretical) invention of the photonic crystal by John [2] and Yablonovitch [3] paved the way for slowing down and localizing pulses of light [4]. Photonic-crystal defect cavities [5] gave a possibility to combine high-Q resonators with small modal volumes. This boosted the study of new regimes of light-matter interaction [6]. The possibility to engineer the dispersion of light led to studies of nonlinear optics in photonic crystals [7, 8], and even a proposal for a nano-source of entangled photon pairs [9].

On the other hand, a technology-centered route was taken. Plasmonics has taken a renewed interest, because of its promise to focus light on a nanometer scale [10], and multitudes of nanostructures were conceived to steer and guide light [11]. The strong wavelength dependence of several resonant effects inspired people to make photon sorters [12], and the sensitivity for minute changes in refractive index paved the way for nanostructured sensors [13].

1.1 Periodic nanostructures

In this thesis, we study a specific class of nanostructures, that is formed by structures that have a periodic variation of material, and therefore of the refractive index. The simplest example of such a structure is the so-called Bragg stack, a periodic variation of thin layers of different materials. At each interface between two adjacent layers, light is scattered. The reflected waves will interfere, and if the wavelength λ and the lattice vector $\vec{k}$ are tuned, such that all reflected waves add constructively, the reflection can add up to unity, and transmission through the structure is forbidden.

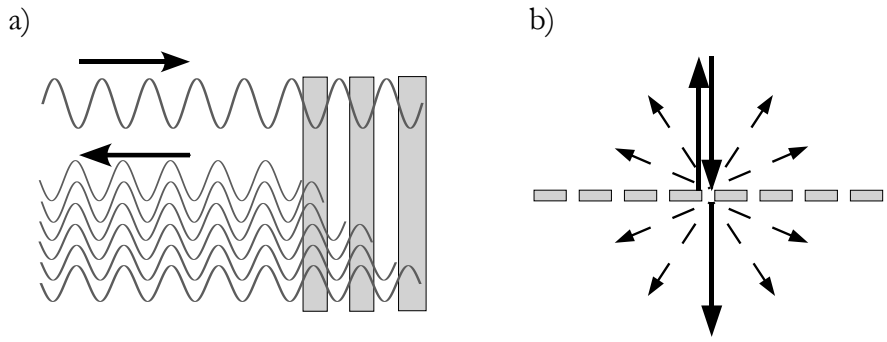

Figure 1.1. (a) Bragg stack. A periodic structure of layers of different refractive index. If the thickness and index difference are tuned right, all reflected waves will interfere constructively and the stack will give unit reflectivity. (b) Diffraction grating. Waves scattered from the periodic structure will interfere constructively in the directions of the dashed arrows. The solid arrows indicate the incident beam and the directly reflected and transmitted beams.

Another well-known example of a periodic structure used to control the propagation of light, is the diffraction grating, that consists of a series of adjacent slits. Each slit act as a line source of radiation that propagates in all directions. In certain directions, where the path length difference between the

light emerging from two adjacent slits equals an integer number of wavelengths, the contributions from all slits will interfere constructively. This will lead to a series of diffracted beams emerging from the slits. The directions θ_m in which this occurs are given by the condition

$$d \sin \theta_m = m\lambda, \tag{1.1}$$

where d is the distance between two slits, and m is an integer number defining the *diffraction order*.

The physics of the diffraction grating, or of any periodic structure, can be more easily understood by describing both systems in terms of their properties in reciprocal space. In this space, plane waves of light are described by their wave vector $k = 2\pi/\lambda$, and their angular frequency ω. For light in an unpatterned material, their relation is simply given by

$$\omega = ck/n, \tag{1.2}$$

where c is the speed of light in vacuo, and n the refractive index of the material.

The structure of the periodic lattice can also be described in reciprocal space. The reciprocal lattice of a periodic structure is periodic as well, and is described by reciprocal lattice vectors $\vec{G}$. Each diffraction process can now be described as adding a reciprocal lattice vector to the wave vector of the light, such that

$$\vec{k}_{\text{in}} + \vec{G} = \vec{k}_{\text{out}}, \tag{1.3}$$

where $\vec{k}_{\text{in}}$ and $\vec{k}_{\text{out}}$ are the wave vectors before and after the scattering process, respectively. In the case of the diffraction grating discussed before, at each interface, the component of the wave vector parallel to the interface, is conserved. The perpendicular component of the wave vector is adapted, such that the dispersion relation (1.2) is fulfilled. When $k_{\text{out}} > 2\pi n/\lambda$, with n the refractive index of the medium in which the scattered wave propagates, no propagating solution exists, and the field of the scattered wave will decay exponentially in the direction perpendicular to the interface.

1.2 Bound modes in slabs and at surfaces

In a planar material, that only has variation of material parameters in one direction (the z-direction), solutions of the wave equation can exist, that are bound to a certain region of z-space, but are propagating freely in the two remaining dimensions. Such a bound mode can be parametrized by a propagation constant (i.e. the component of the wave vector in the xy-plane), that

has to obey the following condition:

$$\beta > \frac{2\pi n_{\text{amb}}}{\lambda}, \tag{1.4}$$

where n_{amb} is the refractive index of the surrounding material. In this thesis, we study two kinds of bound waves: waveguide modes and surface plasmons.

1.2.1 Waveguide modes

The simplest guided modes in a planar structure are waveguide modes. A waveguide can be constructed by surrounding a high refractive index dielectric by media with a lower refractive index. Light in the high refractive index material is bound to this medium by total internal reflection from the interfaces. In a planar waveguide, the waveguide modes can be classified as having the electric field pointing parallel to the waveguiding plane (TE modes) or perpendicular to this plane (TM modes), and by the number of zeros the field has in the waveguide (the mode number). Figure 1.2(a) sketches the electric field distribution of the two first TE waveguide modes for a planar waveguide [14]. The dispersion relation of the different waveguide modes can be calculated numerically. This is done by imposing a wave solution that is exponentially decaying outside the slab, and sinusoidal inside the slab. Boundary conditions at each interface require that the parallel components of the fields are continuous across the interface, which allows us to numerically find solutions for the waveguide modes.

Figure 1.2(b) shows the dispersion relation of the first waveguide modes for a slab with refractive index $n_{\text{slab}} = 3.4$, surrounded by air. Note that both the frequency and the wave vector axis of this graph are scaled by the thickness d of the slab. This reflects the fact that Maxwell's equations are scale invariant. Three different regions can be identified in this graph. The grey area in this graph shows the light cone. In this region, a continuum of solutions exists for a chosen parallel wave vector $k_{\|}$. These solutions have a propagating component in directions away from the slab ($k_{\perp}$ is real everywhere), and are therefore not bound to the dielectric slab.

In the black region, $k_{\perp}$ is imaginary in all regions of space, and no propagating solutions to the wave equation exist at all. Propagation of light is forbidden in this region. In the region in between, light is bound to the slab by total internal reflection, and different waveguide modes exist. The solid curves indicate the dispersion of the TE waveguide modes, and the dashed curves the dispersion of the TM waveguide modes.

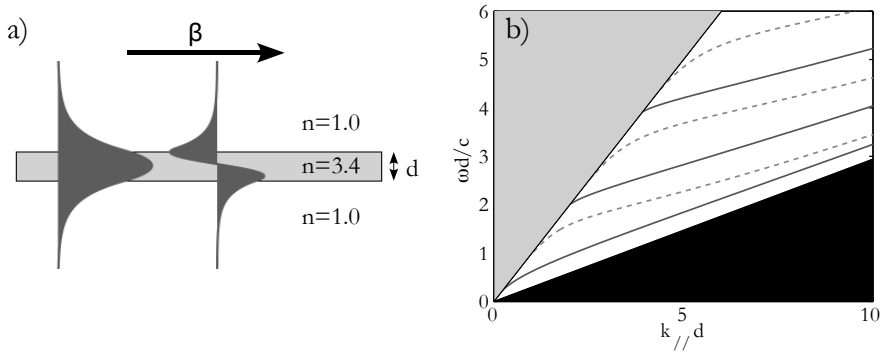

Figure 1.2. (a) Electric field distribution of the first two TE waveguide modes of a slab with refractive index $n = 3.4$, surrounded by air. (b) Dispersion diagram of this structure. The solid and dashed curves give the dispersion of the TE and TM waveguide modes, respectively. The grey area indicates the light cone, were propagating solutions exist that are not bound to the slab. The black area indicates the region where no propagating modes exist at all.

1.2.2 Surface plasmons

On a metal-dielectric interface, another kind of bound wave exists. This is the so-called surface plasmon polariton (surface plasmon for short) [15]. A surface plasmon is a collective oscillation of charges at the boundary between a metal and a dielectric. For a surface plasmon, the magnetic field points parallel to the surface, normal to the propagation vector β. It has a field distribution that is decaying exponentially in both the metal and the dielectric, as is shown in Fig. 1.3(a). Its dispersion relation is shown in Fig. 1.3(b) and is given by

$$\beta(\omega) = \frac{\omega}{c}\sqrt{\frac{\epsilon_{\mathrm{d}}\epsilon_{\mathrm{m}}(\omega)}{\epsilon_{\mathrm{d}} + \epsilon_{\mathrm{m}}(\omega)}}, \tag{1.5}$$

where ϵ_{d} and ϵ_{m} are the dielectric constants of the dielectric and the metal, respectively. Note that, contrary to a waveguide mode, there is no characteristic length scale in this equation, that can be tuned to change the surface-plasmon dispersion. The only length scale is defined by the frequency dependence of the dielectric constant of the gold.

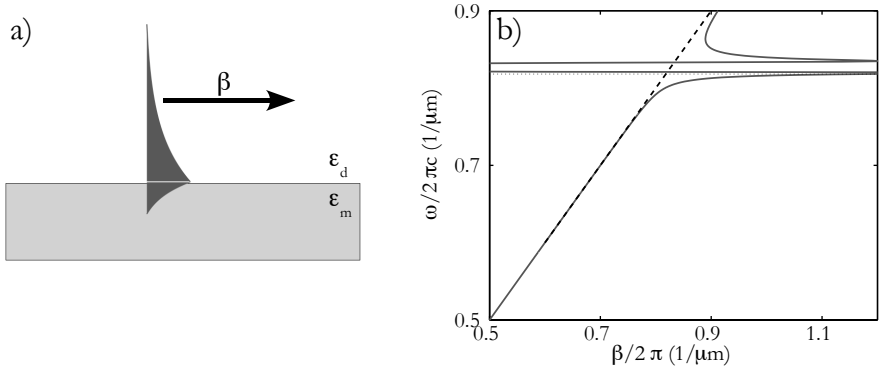

Figure 1.3. (a) Magnetic field distribution for a surface plasmon. (b) Dispersion relation for a surface plasmon on a gold-air interface. For low frequencies, the surface plasmon is close to the light line, indicated by the dashed line. The horizontal dotted line indicates the plasmon frequency.

1.3 Periodic guiding structures

When a planar material that contains guided modes, is patterned with a periodic structure, diffraction will allow light that is incident, to couple to the guided waves, and vice-versa. This is most easily visualized by considering the dispersion relation of the guided wave, and imposing the periodicity of the lattice to the dispersion relation. Figure 1.4 shows the dispersion diagram of the first two waveguide modes from Fig. 1.2, where a one-dimensional periodicity with reciprocal lattice vector G was imposed by repeating the dispersion relation.

A few things can be noticed in this figure. First, by repeating the dispersion relation every reciprocal lattice vector, the frequency ω of a particular mode with well-defined $k_{||}$ is not uniquely defined anymore. Moreover, different waveguide modes cross. At the crossing of two waveguide mode lines in this diagram, interaction between the modes can induce an avoided crossing between the curves, leading to a more complicated dispersion relation. This interaction is caused by the Fourier component of the dielectric function, at the reciprocal lattice vector that links the two crossing curves.

Finally, guided modes show up above the light line (grey area). Where this happens, diffraction from the periodic structure allows light that would otherwise be confined to the waveguide, to propagate away from the waveguiding

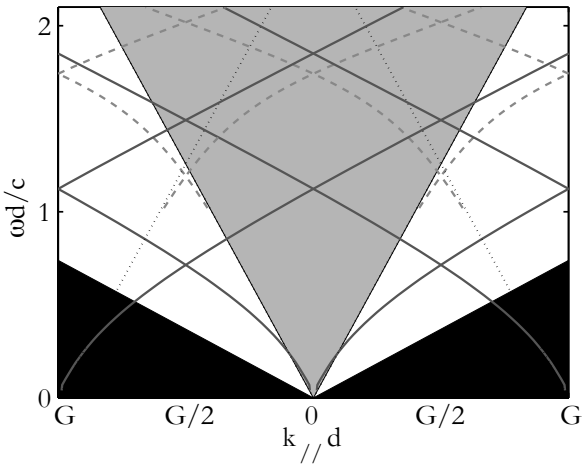

Figure 1.4. Construction of the dispersion relation of the dielectric waveguide of Fig. 1.2, that is patterned with a one-dimensional array of infinitesimal lines. The lattice period $a = 2.5d$, where d is the thickness of the slab. Only the two first waveguide modes are shown. The grey area indicates the light cone. The dash-dotted lines indicate diffraction orders into the surrounding air.

layer. The condition for such a resonance to occur is given by

$$\vec{k}_{\|} = \vec{\beta} + \vec{G}, \tag{1.6}$$

where $\vec{k}_{\|}$ is the parallel component of the wave vector of the incident light. Although this equation gives the frequencies at which resonances occur, the coupling strength, and therewith the width of the resonance, is determined by the Fourier spectrum of the dielectric function.

Just as a Bragg stack has certain wavelengths for which no reflection occurs, the reflection and transmission from a periodic nanostructure bears the signature of the resonances. There are two channels through which light can be transmitted (or reflected) through a patterned structure. First, there is a direct channel, where the light is just reflected or transmitted. Furthermore, there is a resonant channel, in which light is resonantly coupled to the leaky modes, and diffracted back again. Usually, the non-resonant channel is independent of, or slowly varying with, frequency. The reflection or transmission due to the resonant channel is sharply peaked at the resonance frequency, as shown in Fig. 1.5(a). The total transmission or reflection will be the coherent addition of the fields of the two channels, which results in an asymmetric peak

shape as in Fig. 1.5(b). The asymmetry of the peak will be determined by the relative phase of the two channels.

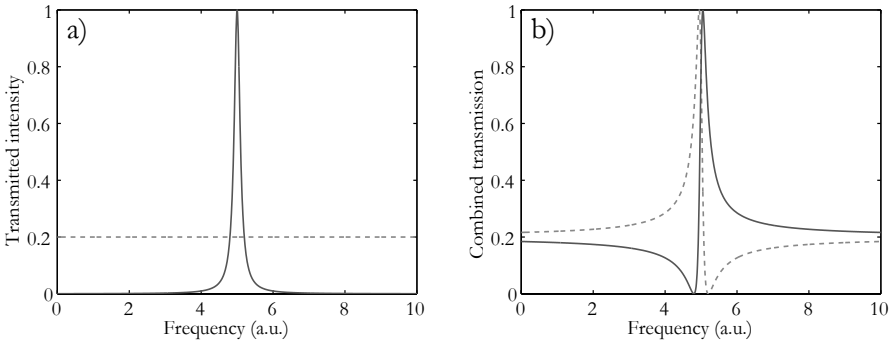

Figure 1.5. (a) Transmission intensity as function of frequency, for the direct (dashed line) and resonant (solid curve) transmission channel. When the two channels are combined, an asymmetric line shape arises due to the coherent addition of the two channels (b). The relative phase of the direct and resonant channel determines the asymmetry of the peak, either red-tailed (dashed curve), or blue-tailed (solid curve).

1.4 This thesis

In this thesis, we investigate how light couples to periodic nanostructures. We study different structures, and start out with dielectric structures. In chapter 2 we discuss the fabrication and reflection spectra of two-dimensional photonic-crystal slabs. We discuss the resonances in terms of a Fano model, and show that light can be coupled resonantly to waveguide modes in the slab. In chapter 3 we discuss the line shape of these resonances, and show that the line shape changes when the angle of incidence is tuned. In chapter 4 we study one of these resonances in more detail. For this, we change to a direct-imaging scheme, which allows us to show the propagation of the light through the resonant modes.

Chapters 5-7 describe experiments using metallic structures. The bound waves in these structures are surface plasmon polaritons, that propagate on either the gold-air or the gold-substrate interface of the hole arrays. Chapter 5 describes an experiment where a dielectric pillar was placed in each of the nanoholes. These pillars act as antennas and increase the coupling to specific surface plasmon modes. In chapter 6, we use a dielectric glass layer on top of the metal hole array to achieve index matching. Besides degenerating the

surface plasmon modes, this dielectric layer acts as a waveguide, which gives rise to extra resonances in the transmission spectra. Finally, in chapter 7, we study surface plasmon modes on both sides of the hole array, that are made degenerate by immersing it in an index-matching liquid, and discuss the coupling that is a result of this degeneracy.

The last two chapters discuss the optics of a new kind of single-photon detector, that consists of a very thin superconducting meander. We study the polarization dependence of these detectors in chapter 8, and we describe the absorption of light in this thin meander in terms of an optical impedance model. In chapter 9, we show that the absorption in a metallic film of only a few nanometers thickness can be as high as 95%, for one single polarization. Besides that, we extend these results to the geometry of the single-photon detectors, and show that it is equally possible to make a detector with such a high absorption efficiency.

1.5 Polarization convention

Throughout this thesis, I tried to consistently use the following classifications for the polarization of light in experimental setups and for the polarization of different modes. When a mirror symmetry is present, modes will have a profile that is either even or odd with respect to this symmetry plane. The polarization is also defined with respect to these symmetry planes:

- *s*- and *p*-polarization define a polarization with respect to the scattering plane of a reflection. Light that has its electric field perpendicular (*senkrecht*) to this plane (i.e., parallel to the reflecting surface) is denoted with *s*-polarization, whereas light that has the electric field parallel to the scattering plane, is denoted as being *p*-polarized.

- TE and TM polarization have another meaning. In two-dimensional periodic structures, they define the polarization with respect to the third dimension. When the electric field is perpendicular to the direction of translation symmetry, i.e. in the plane of the reciprocal lattice vectors, it has TE (transversally electric) polarization, otherwise it has TM (transversally magnetic) polarization. For slab waveguides, TE and TM are defined with respect to the waveguiding layer. TE waveguide modes have the electric field in the plane of the slab waveguide, whereas TM waveguide modes have the magnetic field in the plane of the slab.

Part I

Photonic-crystal slabs

Chapter 2

Fano resonances and waveguide modes in a two-dimensional photonic-crystal slab

The measured reflection spectra of two-dimensional photonic crystal slabs consist of an asymmetric peak on top of an oscillating background. For p-polarized light, this asymmetric peak changes shape, when the angle of incidence is tuned over Brewster's angle. We explain the observed line shapes with a Fano model that includes loss and use a waveguide model to predict the resonance frequencies of the photonic-crystal slab. Finite-difference time domain calculations support the model and show that resonances due to higher order waveguide modes disappear when the substrate refractive index is increased beyond $n_{\mathrm{s}} = 2.04$. This is readily explained by the cut-off condition of these modes, given by the waveguide model.

This chapter is based on E. F. C. Driessen, P. O. M. Heemskerk, D. Stolwijk, E. W. J. M. van der Drift, and M. J. A. de Dood, *Asymmetry reversal and waveguide modes in the reflection from a two-dimensional photonic-crystal slab*, Proc. SPIE **6989**, 69890G (2008).

2.1 Introduction

Resonant optical structures, in particular photonic crystals embedded in a waveguide, form an important class of optical materials. These photonic-crystal slabs contain a periodic arrangement of holes on a wavelength scale, and allow control of the propagation of light, guided in the plane of the waveguide [16]. For example, they enable wavelength-dependent steering [17], strong coupling of atoms to a cavity [18], and enhanced non-linear optical effects [8].

A measurement of the reflectivity as a function of the wavelength is a relatively easy way to characterize the optical properties of these slabs. At each angle of incidence, the reflectivity spectrum shows a number of resonant features related to coupling of incident radiation to a leaky waveguide mode of the photonic-crystal slab [19, 20]. The reflection spectra can be calculated numerically by solving Maxwell's equations using a scattering-matrix approach [21,22], Green's functions [23], or finite-difference time domain (FDTD) methods [19, 24]. Although these numerical solutions of Maxwell's equations predict the right frequencies and quality factors of the resonances observed in the measurements, they do not give physical insight into the origin of the spectral features. Therefore, it is important to develop simpler models to explain the measured resonances. Such models can be used as a diagnostic tool for fabricated structures, and can facilitate the first design of a photonic crystal structure.

Here, we present reflection measurements on a two-dimensional (2-D) photonic-crystal slab. We use an extended coupled-mode theory to describe the shape of the measured reflectivity spectra and the line shape of the resonant features. This theory explains the change in asymmetry that is observed when changing the angle of incidence, as resulting from the change of sign of the Fresnel reflection coefficient of the layered structure at Brewster's angle. We use a waveguide model [25, 26] to predict the resonance frequencies of a photonic-crystal slab and compare this model to FDTD calculations. The disappearance of modes from the spectra when increasing the refractive index of the substrate is explained by the model in terms of the cut-off condition of the guided modes.

2.2 Photonic crystal fabrication

The GaAs and AlGaAs photonic crystals in this study were fabricated using a combination of electron-beam lithography and reactive ion etching*. A square lattice of 1000×1000 holes, with a radius $r \approx 100$ nm and a lattice constant $a \approx$

*The detailed fabrication recipe can be found in Appendix A

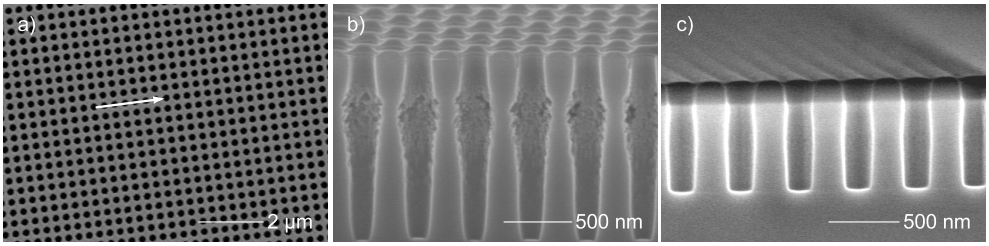

Figure 2.1. SEM images of photonic crystal structures fabricated by reactive ion etching in a Cl_2/N_2 plasma. (a) Top view of the photonic crystal structure used for the measurements in Sec. 2.4. The arrow corresponds to the direction of $k_{\parallel}$ in the reflection measurements. (b) Cross section (taken under an angle of 45°) of the etched holes when no N_2 is added. The non-passivated side walls are partially etched away by the plasma. (c) Cross section of the holes (taken under an angle of 55°) when 10 sccm of N_2 is added to passivate the side walls. The silicon nitride mask on top is still visible.

320 nm, was defined by electron-beam lithography in a $\sim$ 550 nm thick layer of ZEP 520 positive-tone resist* on top of a $\sim$ 300 nm layer of silicon nitride. After development, the pattern was transferred to the nitride by reactive ion etching using a low pressure (< 8 μbar) CHF_3:Ar (1:1) plasma. The remaining ZEP resist was removed with an oxygen plasma.

The resulting hole pattern in the nitride serves as a mask for reactive ion etching of the (Al)GaAs with a chlorine-based plasma [5, 27]. In this process, the chlorine ions etch the (Al)GaAs, while the nitrogen is used to passivate the side walls. We used a power of 100 W, a pressure < 5 μbar, and a flow of 15 sccm BCl_3 and 7.5 sccm Cl_2, and varied the N_2 flow to tune the profile of the side walls. The selectivity of the etching process is $> 10:1$, and the etch rate depends on the hole size and the nitrogen flow, i.e. $\sim$ 200 nm/min for holes with a diameter of 300 nm, and $\sim$ 1 μm/min for holes with a diameter of 1 μm, with N_2 added. Figure 2.1(a) shows a scanning electron microscope (SEM) image of the photonic crystal after the fabrication process. Figure 2.1(b) shows a cross section of the holes when using a plasma without N_2 added, showing damage to the side walls of the holes. In Fig. 2.1(c), we added a flow of 10 sccm N_2 to the plasma, resulting in straight holes. A slight curvature of the holes is observed in Fig. 2.1(c). The curvature is due to specular reflection of the ions from the slightly tapered nitride mask, and the depth at which it occurs depends on the hole diameter. This curvature is therefore not intrinsic to the

*ZEON corporation, http://www.zeon.co.jp

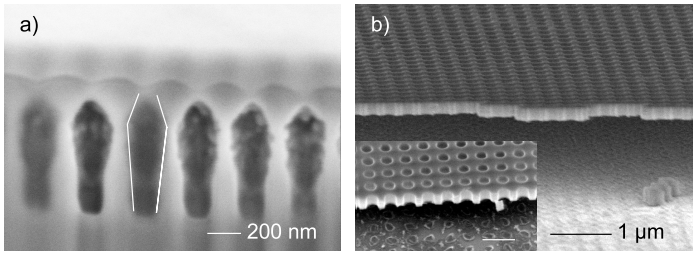

Figure 2.2. SEM images of (a) the cross section of the photonic crystal used for the measurements in section 2.4 (taken under an angle of 59°). The approximate shape of the holes is indicated with the white curves. (b) A large, high-quality, free-standing photonic-crystal membrane. The GaAs capping layer is not removed from the membranes in this picture. The inset shows an enlarged image of the holes. The length of the scale bar in the inset is 500 nm.

process and straight holes as deep as a few microns can easily be achieved. In the final stage, we selectively removed the silicon nitride mask using the same CHF_3:Ar reactive ion etch used to define the mask.

Figure 2.2 shows SEM images of photonic crystal samples that consist of a higher refractive index slab layer on top of a substrate with a lower index. The structure in Fig. 2.2(a) was fabricated in a GaAs substrate using a relatively low N_2 flow, leading to incomplete passivation of the side walls. The lines in the figure indicate the resulting tapering of the holes. The undercut effectively defines a waveguide structure that was used in the optical measurements of Sec. 2.4.

The same reactive ion etch can be used to define high quality photonic crystals in a free-standing membrane. Figure 2.2(b) shows a part of such a membrane structure, consisting of 1000×1000 holes ($\sim 300\times300\ \mu m^2$). To fabricate this structure, we used a GaAs substrate with a heterostructure consisting of a 1000 nm $Al_{0.7}Ga_{0.3}As$ sacrificial layer, a 300 nm thick $Al_{0.35}Ga_{0.65}As$ membrane layer, and a 100 nm thick GaAs capping layer to prevent oxidation. After transferring the photonic crystal pattern to the heterostructure, we selectively removed the GaAs capping layer, using a wet etch of peroxide and citric acid [28]. In the last step, a wet etch with hydrofluoric acid was used to selectively remove the aluminium-rich sacrificial layer [5], thus creating the free-standing photonic-crystal membrane in Fig. 2.2(b). Note that the curvature of the holes due to the tapered nitride mask occurs in the sacrificial layer in this case.

2.3 Theory

The reflection spectrum of a photonic-crystal slab typically consists of an oscillating background and a number of sharp resonances [19, 20] as shown in Fig. 2.4 and Fig. 2.6. The spectrum can be explained using a simple scattering model of a resonator coupled to a continuum of modes. The photonic-crystal slab, that acts as the resonator, is depicted in Fig. 2.3(a), together with the input and output ports. Part of the radiation incident on the slab is diffracted into a leaky waveguide mode (dashed arrows), whereas another part is directly reflected and transmitted (solid arrows). The radiation that is diffracted back from the waveguide mode interferes with the directly reflected and transmitted radiation, yielding the characteristic Fano line shape [29]. In Sec. 2.3.1 we extend a temporal coupled-mode theory [30] to include loss, and describe the reflection in terms of the parameters of the direct and resonant channels. After that, in Sec. 2.3.2, we introduce a waveguide model to predict the resonance frequency of the resonant channel.

2.3.1 Fano model

To calculate the spectrum of the transmitted and reflected light, we proceed as follows. For each angle of incidence and each wavelength, a scattering matrix links the amplitudes of the incident, reflected, and transmitted waves. The scattering matrix S of the system is the sum of the scattering matrices of the direct and the resonant channel. The direct channel is described by a scattering matrix C, given by

$$C = \begin{pmatrix} r_1 & t_{21} & \cdots \\ t_{12} & r_2 & \\ \vdots & & \ddots \end{pmatrix}, \tag{2.1}$$

that connects the amplitudes of the modes (ports) on both sides of the slab. When there are no propagating diffraction orders in the media above and below the guiding layer, the components of the scattering matrix are given by the Fresnel reflection and transmission coefficients for a homogeneous layered system. The contribution from the direct channel gives rise to typical oscillations in the reflectivity as a function of wavelength (Fabry-Perot fringes). If there are propagating diffraction orders in the media above or below the guiding layer, a more elaborate method is needed to calculate the matrix elements of C.

The resonant channel corresponds to a coupling of the incident radiation to a single leaky waveguide mode via diffraction from the periodic photonic

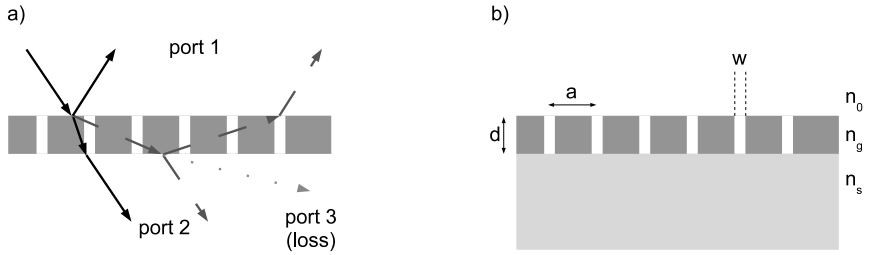

Figure 2.3. (a) Schematic drawing of the direct and resonant reflection and transmission in a photonic-crystal slab. The incident light in port 1 can be scattered via the direct channel (solid arrows) or diffracted into a waveguide mode (resonant channel, dashed line). The waveguide losses can be modeled by including a third port (dotted arrow) to the system. (b) Geometry of the photonic-crystal slab used in the FDTD calculations in section 2.3.2. The slab of thickness d and refractive index n_{g} contains a periodic array of air slits with a width w and a periodicity a. The slab is supported by a substrate with refractive index n_{s}, and covered by air ($n_0 = 1$) on the top.

crystal structure. For a fixed angle of incidence, the coupling to a specific waveguide mode p occurs at a resonance frequency ω_p and is characterized by an escape rate γ_p. This escape rate parametrizes the life time of light in the waveguide mode. The coupling to the waveguide mode is described by coupling constants $d_{j,p}$, where the index j corresponds to the different ports coupling to the waveguide mode. The coefficients γ_p, $d_{j,p}$, and the matrix elements C_{jk} are not independent. Time-reversal symmetry and energy conservation put the following constraints on the coupling constants (a derivation of these conditions is given in Ref. 30):

$$\sum_j |d_{j,p}|^2 = 2\gamma_p, \tag{2.2}$$

$$\sum_k C_{jk} d^*_{k,p} = -d_{j,p}, \tag{2.3}$$

where the indices j and k refer to the different ports, and C_{jk} are the elements of the direct transmission matrix connecting the different free-space modes. Equation (2.3) links the amplitude and phase of the coupling constants to the scattering matrix C of the direct process.

The matrix elements of the scattering matrix S for the combined system

of direct and indirect coupling are given by

$$S_{jk} = C_{jk} + \sum_p \frac{d_{j,p} d_{k,p}}{i(\omega - \omega_p) + \gamma_p}, \tag{2.4}$$

where ω is the angular frequency of the incident radiation. The reflection coefficients for the different ports are given by the diagonal elements of this matrix, and the transmission coefficients by the off-diagonal elements. This description which uses a Lorentzian line shape for the resonant channel, is a simplification which holds as long as $\omega_p \ll \Gamma_p + \gamma_p$. The small frequency shift that results from describing our resonance with a Lorentzian can be included in the resonance frequencies ω_p. It is important to stress that the equations derived here hold for the case of *uncoupled* waveguide modes only. For the modes to be uncoupled, it is necessary that the number of independent ports, i.e. the rank of the matrix C_{ij}, is larger than or equal to the number of waveguide modes p [31].

Losses can be included in the description in this model, by discriminating between losses in the direct channel, due to absorption or surface roughness, and losses in the resonant channel. Losses in the resonant channel can also be due to scattering of the waveguide mode to ports that are not incorporated in the scattering matrix description.

Absorption losses in the direct scattering channel can be adequately described by using a non-unitary scattering matrix C and the Fresnel coefficients of a layered system with complex-valued refractive index. This matrix can be made unitary by adding an extra port to the description. If we assume that the input in this extra port is zero, and that the loss port is not coupled to the resonator mode, then the scattering matrix S includes a block matrix describing the normal input and output ports of the system, that is not influenced by the parameters of the loss port. This makes it possible to use Eqs. (2.2)-(2.4), while using a non-unitary scattering matrix C for the direct channel.

Waveguide losses can be incorporated in a similar way, by extending the model with extra loss ports, which only couple to the specific waveguide modes. Each waveguide mode couples to its loss port with a coupling constant Γ_p. The direct scattering matrix for a two-port system with an additional loss port acquires the form

$$C = \begin{pmatrix} r_1 & t_{21} & 0 \\ t_{12} & r_2 & 0 \\ 0 & 0 & 1 \end{pmatrix}. \tag{2.5}$$

The loss rates Γ_p are incorporated in Eq. (2.2) in a straightforward way, by using the convention $\sum_j |d_{j,p}|^2 = 2\,(\gamma_p + \Gamma_p)$, where the index j now runs over

all ports.

For the symmetric case of two ports coupled to only one leaky waveguide mode, symmetry requires that $r_1 = r_2 = r$ and $t_{21} = t_{12} = it$, where r and t are real. Moreover, the coupling constants to the ports should be equal, except for a plus or minus sign determined by the odd or even symmetry of the waveguide mode with respect to the mirror plane. The reflectivity in this case is given by

$$R = \left| r + \gamma \frac{-r \mp it}{i(\omega - \omega_0) + \gamma + \Gamma} \right|^2, \tag{2.6}$$

where the $\mp$ is determined by the even or odd symmetry of the mode [30], and the parameters ω, γ, and Γ lost their subscripts since we are dealing with only one waveguide mode. This expression gives the typical asymmetric Fano line shape. The reflectivity has a distinct zero if the loss rate $\Gamma = 0$. To reach 100% reflectivity, the direct process has to be lossless as well (i.e. $|r|^2 + |t|^2 = 1$).

2.3.2 Waveguide modes

The model in the previous section gives a description of the line shape in the reflectivity of a photonic-crystal slab, but it does not predict the resonance frequencies ω_p. As we will show in this section, it is possible to calculate the resonance frequencies and the waveguide modes for a photonic-crystal slab using a simple model [25,26,32]. In this nearly-free photon approximation, the waveguide is treated as a uniform slab with an effective refractive index that depends on the filling factor of the air holes. For the TE waveguide modes, having the electric field in the plane of the slab, the dispersion relation for a uniform slab is implicitly defined as [14]

$$\sin(hd)\left(h^2 - pq\right) = \cos(hd)(p+q)h, \tag{2.7}$$

where p, q, and h denote the transverse components of the wave vector in the different media. They are defined as $q^2 = \beta^2 - \left(\omega^2/c^2\right) n_0^2$, $h^2 = \left(\omega^2/c^2\right) n_\mathrm{g}^2 - \beta^2$, and $p^2 = \beta^2 - \left(\omega^2/c^2\right) n_\mathrm{s}^2$, where n_0, n_g, and n_s are the refractive indices of the top, guiding, and bottom layer, respectively, and c is the speed of light in vacuo. The condition for coupling to a waveguide mode is given by the diffraction condition

$$\vec{k}_\parallel + \vec{G} = \vec{\beta}, \tag{2.8}$$

where $\vec{k}_\parallel$ is the parallel component of the incident wave vector, $\vec{\beta}$ is the parallel component of the wave vector of the waveguide mode, and $\vec{G}$ is a reciprocal lattice vector of the photonic crystal. For normal incidence, this reduces to

$\vec{\beta} = \vec{G}$, which can be used to numerically find the resonance frequencies ω_m from Eq. (2.7).

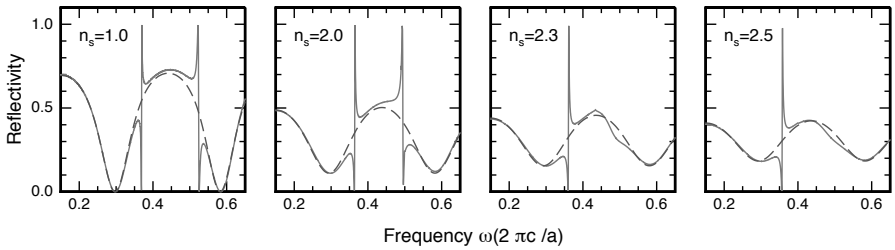

Figure 2.4. Reflectivity of a 1-D photonic-crystal slab, calculated using a FDTD method. The grating consists of air slits with $w/a = 0.1$ in a dielectric slab with $d/a = 0.5$ and refractive index $n_\mathrm{g} = 3.5$, on top of a substrate with increasing refractive index. Two resonances are visible, on top of an oscillating background. The dashed curve is a fit to the background of a refractive index of the form described in Eq. (2.9). The resonance around $\omega = 0.5$ disappears for $n_\mathrm{s} > 2.0$.

For simplicity, we calculated the reflectivity of an one-dimensional (1-D) array of slits, using a freely available FDTD package [33]. The cross section of the structure used in these calculations is given in Fig. 2.3(b). The slab of thickness d and refractive index $n_\mathrm{g} = 3.5$ contains an array of slits of width w and refractive index $n_0 = 1$. The array has a lattice constant a and we used $w/a = 0.1$ and $d/a = 0.5$. The substrate index n_s was varied between 1 and 3.0, and the reflection spectra were calculated at normal incidence for TE-polarized light (E-field parallel to the slits).

Figure 2.4 shows the reflectivity of the array as a function of frequency, for increasing substrate index n_s. Two distinct resonances are visible on top of an oscillating background. The Fresnel reflection coefficient for the layered system can be fitted to the spectra, using an effective refractive index of the form [24]

$$n_\mathrm{g} = c_0 + c_1\omega + c_2\omega^2, \tag{2.9}$$

with c_0, c_1, and c_2 as only fit parameters. Typical values for the fit parameters are $c_0 = 3.25$, $c_1 = 0.42$, and $c_2 = -0.21$, yielding an effective index between 3.25 and 3.46. The result of the fit is shown as the blue dashed lines in Fig. 2.4. The effective index is close to the volume average of the dielectric constants [34, 35] for $\omega < 0.5$, but deviates for higher frequencies. This is due to the fact that for higher frequencies the wavelength becomes comparable to the lattice spacing and slit width, and simple effective-medium theory breaks down.

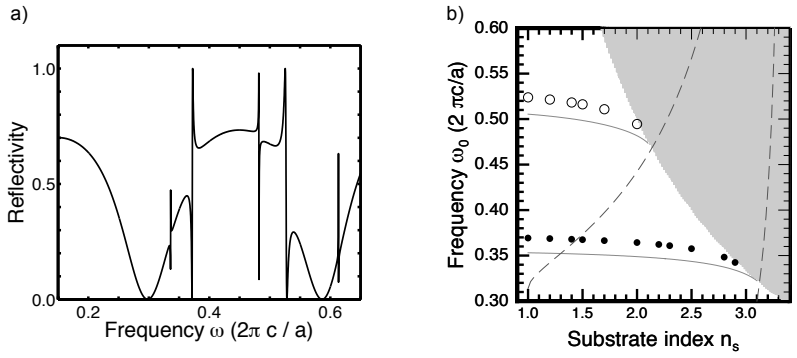

Figure 2.5. (a) Calculated reflectivity of the array of slits at 5° angle of incidence, for a substrate index $n_s = 1$. Two resonances that are not visible at normal incidence appear at $\omega \approx 0.33$ and $\omega \approx 0.48$. (b) Resonance frequencies of the Fano resonances as a function of the substrate refractive index n_s. The resonance frequencies can be predicted using a simple waveguide model (red curves), with n_g given by effective medium theory. This model does not include the avoided crossing between the two waveguide modes, and therefore calculates the average of the high-frequency and low-frequency resonances. The dashed curves correspond to the cut-off conditions of the $m = 0$ and $m = 1$ modes. The gray area indicates the parameter region where higher order diffraction into the substrate occurs.

At normal incidence, the resonances corresponding to a specific reciprocal wave vector $\vec{G}$ are degenerate. Due to the grating, they are coupled and show an avoided crossing. A simple explanation of the fact that we only observe one of the resonances is given in terms of coupled mode theory [36]. For a sinusoidal 1-D grating with a dielectric function that contains only a Fourier component $\epsilon(\vec{G})$, no avoided crossing occurs at normal incidence. The interaction that creates the avoided crossing is caused by the higher harmonics of the dielectric function $\epsilon(\vec{r})$. The coupling to these modes is determined by the relative phase of the Fourier components. For a 1-D square profile, the first and second harmonic are out of phase ($\phi = \pi/2$ in the notation of Ref. 36). The Bloch wave that mediates the coupling to the resonance only has nonzero overlap with the high-frequency mode. This leads to zero coupling strength to the low-frequency mode, and as a consequence, the peaks in Fig. 2.4 are exclusively due to coupling to the high-frequency mode [26]. The fact that we only observe the high-frequency mode at normal incidence is confirmed by the calculation in Fig. 2.5(a), that shows a reflection spectrum for the 1-D grating with a substrate index $n_s = 1$, at an angle of incidence of 5°, calculated using

a rigorous coupled wave analysis [37]. In this figure, the lower-frequency resonances can be seen to appear as narrow resonances at $\omega = 0.33$ and $\omega = 0.48$.

As can be seen in Fig. 2.4, the two resonances visible for $n_s \leq 2.0$ at normal incidence have opposite symmetry. This is consistent with the fact that these resonances are due to the first and second TE waveguide mode, that have an even and odd field distribution, respectively. For a refractive index $n_s > 2.0$, the second resonance is seen to disappear from the spectrum. We fitted Eq. (2.6) to the calculated spectra, using the refractive index obtained by the fit of the oscillating background as an input. The only fit parameters are the resonance frequencies ω_0 and ω_1, and the line widths γ_0 and γ_1. The resulting resonance frequencies are shown as the symbols in Fig. 2.5(b), plotted as a function of the substrate refractive index, and are compared to the numerical solution of Eq. (2.7) (solid curves) obtained using $n_g = 3.34$. The calculated frequencies are below the frequencies obtained from the fits, because the waveguide model predicts the center frequency and does not take into account the avoided crossing. In fact, the data in Fig. 2.5(a) for 5° angle of incidence show that the waveguide model correctly predicts this center frequency.

The disappearance of the resonance is also predicted by the waveguide model. The cut-off frequency of the m-th mode is given by [14]

$$\omega_{cm} = \frac{c}{2\pi d\sqrt{n_g^2 - n_s^2}} \left(m\pi + \arctan \sqrt{\frac{n_s^2 - n_0^2}{n_g^2 - n_s^2}} \right). \tag{2.10}$$

This condition is drawn with dashed curves in Fig. 2.5(b) for the first two waveguide modes, calculated using an effective refractive index $n_g = 3.34$. Diffraction into the substrate occurs at a frequency ω_d, where the propagation constant β becomes equal to the length of the wave vector in the substrate. This leads to the condition

$$\omega_d = (k_{\|} + G)/n_s. \tag{2.11}$$

The existence of diffraction orders at normal incidence is indicated by the grey area in Fig. 2.5(b). This corresponds to the situation where the transverse component of the wave vector in the substrate $p = 0$. The resonance frequency of the waveguide mode *at cut-off* is thus given by the intersection of Eq. (2.10) and Eq. (2.11).

It is important to mention here that although assigning the different resonances to different modes is quite straightforward in the 1-D case, in the 2-D case TE-TM mixing will occur [38]. The mixing between different modes induces avoided crossings between otherwise orthogonal modes, and causes TE

modes to appear in the TM spectra, and vice-versa. This makes identification of specific peaks with specific waveguide modes more complicated.

2.4 Reflection measurements

We measured the specular reflection from the GaAs photonic-crystal slab shown in Fig. 2.1(a) along the Γ-X direction (indicated with the arrow) as a function of the angle of incidence from 25° to 80°. White light from a spectrally broad lamp was polarized and focused onto the sample. The specular reflection was polarization-filtered, imaged onto a fiber, and analyzed in a spectrometer with a spectral resolution of ~ 2 nm. The numerical aperture (NA) of the incoming beam was limited to NA < 0.04. The spot size on the sample was ~ 100 μm.

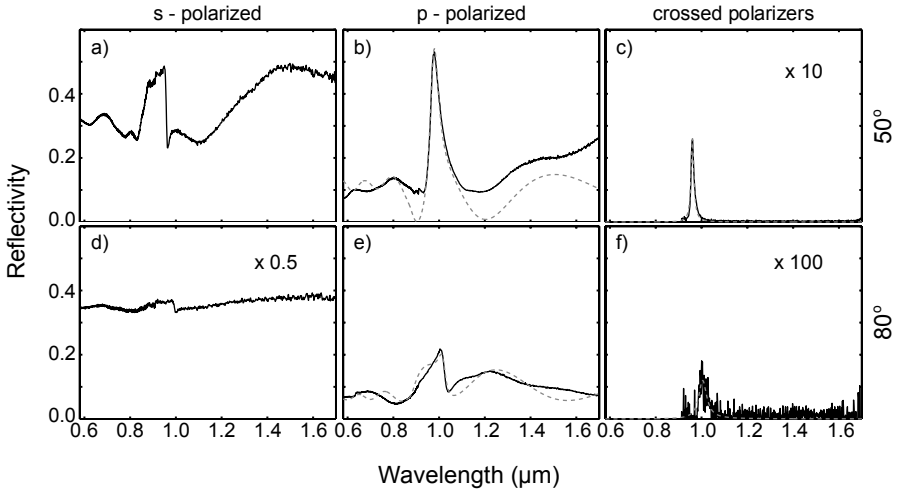

Figure 2.6. Experimental reflection spectra of a photonic-crystal slab for two angles of incidence, 50° [(a) to (c)] and 80° [(d) to (f)], for *s*-polarized [(a) and (d)] and *p*-polarized light [(b) and (e)], and for a crossed polarizer setup, where the incoming light was *p*-polarized and the detected light was *s*-polarized [(c) and (f)]. The dashed curves are fits using the model discussed in the text. Figures (c), (d), and (f) are scaled with the factors indicated, to enhance visibility.

Reflection spectra for angles of incidence of 50° and 80° are shown in Fig. 2.6 for three different settings of the polarizers. Figures 2.6(a) and (d) show the spectra for the situation where both polarizers were set to a polarization perpendicular to the scattering plane (*s*-polarization). An asymmetric

peak around a wavelength of ~ 950 nm is seen on top of an oscillating background. The peak position changes with angle of incidence. Similar peaks can be seen in Fig. 2.6(b) and (e), where both polarizers were set to a polarization parallel to the scattering plane (p-polarization). In this case, the asymmetry of the peak is changed when tuning the angle of incidence from 50° to 80° The symmetry of the peak is the same for both polarizations at 80° angle of incidence.

The Fano model described in Sec. 2.3.1 can be used to describe the observations. We use Maxwell-Garnett's effective medium theory [34,35] to describe the photonic crystal layer as a homogeneous birefringent layer with an effective refractive index n_{eff}, incorporating the known refractive index dispersion of GaAs [39]. This includes absorption for wavelengths shorter than 950 nm. With this effective index, we calculate the polarization- and angle-dependent Fresnel reflection and transmission coefficients of the layered system.

The dashed curves in Fig. 2.6 show fits of the Fano model to the measurements. The only fit parameters were the resonance frequency ω_0, the linewidth γ, and the waveguide losses Γ. We slightly adjusted the effective index n_{eff} for different angles of incidence, to get a better fit to the oscillating background. Although the fits deviate on detail from the measurements, qualitatively all elements of the measurement are contained in the model. We attribute most deviations to the simplifications we made with respect to the vertical shape of the air holes, and to the fact that effective medium theories only hold when all relevant length scales in the system are much smaller than the wavelength. In fact, the tapering of the holes is essential to observe the resonances. It ensures that there is a waveguiding layer in the top part of the photonic-crystal structure, that provides a discrete mode.

The Fano model also gives a direct explanation for the change in asymmetry of the peak. Since the peak shape is determined by interference of a resonant and a direct channel, the relative phase between these two contributions determines the asymmetry of the resulting peak. The Fresnel coefficient r for s-polarized light is always negative, but the Fresnel coefficient for p-polarized light vanishes and changes sign at Brewster's angle. It is exactly this change of sign that causes the line shape to change when the angle of incidence is tuned to larger angles (see Ch. 3 and Refs. 40, 41). The fact that the asymmetry for s-polarized light is the same as for p-polarized light at large angles of incidence indicates that both peaks are due to coupling to a waveguide mode that is even in the center plane of the photonic-crystal slab.

In Fig. 2.6(c) and (f) the reflection spectra of the photonic-crystal slab is shown in a setup where the incoming light was p-polarized, and the collected

light was s-polarized. A small Lorentzian-shaped peak can be observed in these spectra. The resonance frequencies obtained from the fits of the different measurements are not exactly identical for the same angle of incidence. This indicates that the peaks in Fig. 2.6(a), (b), and (c) are due to different waveguide modes. Since Fresnel reflection is polarization-maintaining for s- and p-polarization, the direct channel is filtered out by the second polarizer. This results in a resonant contribution only, explaining the Lorentzian line shape of the peak [42]. The intensity of these peaks is low, because the symmetry of the photonic-crystal lattice dictates that the polarization (s or p) is conserved upon transmission and reflection, as long as the wave vector $k_{\|}$ is along one of the symmetry directions of the lattice. The fact that we do observe a small peak demonstrates that our structure does not have perfect square symmetry.

2.5 Conclusion

In summary, the typical asymmetric peaks on top of an oscillating background, observed in the reflection from a photonic-crystal slab, are due to interference between a direct and a resonant reflection channel. The observed change of asymmetry of the peak, for p-polarized light, is caused by a change of sign of the direct reflection at Brewster's angle. This asymmetry change will be discussed in detail in Ch. 3. The rough shape of the holes in our experiment causes relatively broad spectral features that are easily resolved. The fact that we are able to describe our data with a coupled mode theory and observe the change in asymmetry of the spectral line shows that the description is robust and also valid for less-than-perfect photonic crystals.

The frequencies of the resonances can be predicted using a simple waveguide model, using the effective index of the guiding layer as the only adjustable parameter. This model can be used to predict the disappearance of certain resonances from the reflectivity spectrum, when changing the substrate refractive index. The predictions for waveguide cut-off of the second TE mode are confirmed by FDTD calculations of the reflectivity. The ability to control the coupling to specific modes can be an important design parameter for photonic crystal structures, if coupling to a specific mode is undesirable. Another possible application is to create an optical switch, where a change in the optical parameters of the guiding layer can be used to temporarily transform one of the guided modes into a leaky mode.

Chapter 3

Asymmetry reversal in the reflection from a two-dimensional photonic-crystal slab

The measured, angle-dependent, reflection spectra of a 2-D GaAs photonic-crystal slab consist of an asymmetric peak on top of an oscillating background. At large angles of incidence ($> 70°$), the asymmetry of the peak is observed to flip for p-polarized light. We explain the observed spectra with a Fano model that includes loss and interference between a resonant waveguide component and direct Fresnel reflection of the layered structure. We show that the reversal of the asymmetry of the line is due to a change in sign of the direct reflection at Brewster's angle.

This chapter is based on E. F. C. Driessen, D. Stolwijk, and M. J. A. de Dood, *Asymmetry reversal in the reflection from a two-dimensional photonic crystal*, Opt. Lett. **32**, 3137–3139 (2007).

3.1 Introduction

Optical reflectivity measurements of two-dimensional photonic-crystal slabs are a relatively easy way to characterize the properties of these slabs. The wavelength dependent spectra show a number of features related to the leaky waveguide modes of the slab [19,20]. A lot of effort has been devoted to calculating these spectra by rigorously solving Maxwell's equations, using scattering matrices [21,22], Green's functions [23] and finite difference time domain methods [19,24]. Although being able to reproduce the spectra, these calculations do not give physical insight into the origin of the spectral features. Therefore it is important to develop simpler models that can explain the measured resonances. Such models are an important diagnostic tool for fabricated structures and can facilitate the first design of a photonic crystal structure.

In this Chapter, we present reflection measurements on a 2-D photonic-crystal slab. We study the line shape of a resonance in this spectrum, as a function of the angle of incidence. The asymmetry of the (Fano) line shape [29,30] in the reflection spectra is observed to change for p-polarized light. Our observations can be described with an extended coupled mode theory, linking the reversal of asymmetry to the change of sign of the Fresnel reflection coefficient of the layered structure. This change of sign occurs at Brewster's angle.

3.2 Experiment

The photonic crystal in this study was fabricated in GaAs using e-beam lithography and reactive ion etching. It consists of a square lattice of 1000×1000 holes with radius $r \approx 100$ nm and lattice constant $a \approx 320$ nm. Figure 2.1(a) shows a scanning electron microscope (SEM) image from the top, and Fig. 2.2(a) a cross-section (made with a focussed ion beam). Due to details of the fabrication process, the cross-section of the holes consists of two slightly tapered parts, as can be seen in figure 2.2(b). The holes become wider until a depth of ~ 600 nm, and then narrow down until a depth of $1.5 - 2$ μm.

We measured the specular reflection from the photonic crystal along the Γ-X direction [indicated with the arrow in figure 2.1(a)], as a function of the angle of incidence from 25° to 80° in steps of 2.5°. White light from a spectrally broad lamp was polarized and focused onto the sample. The specular reflection was polarization-filtered, imaged onto a fiber and analyzed in a spectrometer with a spectral resolution of ~ 2 nm. The numerical aperture (NA) of the incoming beam was limited to NA < 0.04. The spot size on the sample was ~ 100 μm. We measured the spectra for both polarizations, but show only the

results for p-polarized light.

Reflection spectra for angles of incidence of 50, 70 and 80° are shown in figure 3.1. The spectra show a large, asymmetric peak, on top of an oscillating background. By changing the angle of incidence, the peak shape in figure 3.1 changes from asymmetric with a tail on the red side (a), to symmetric (b), to asymmetric with a tail on the blue side (c).

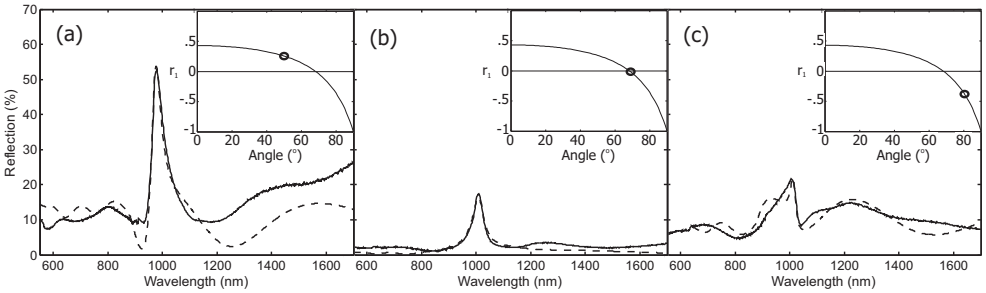

Figure 3.1. Experimental reflection spectra of the photonic-crystal slab for 3 angles of incidence: 50° (a), 70° (b) and 80° (c). The dashed lines are fits using the model discussed in the text. The insets show the reflection coefficient r_1 for an interface of air and $n_{\text{eff}} = 2.5$, as function of angle of incidence. The circles indicate the angle of the measurement.

3.3 Model

In order to explain our measurements, we extended the temporal coupled-mode theory in Ref. 30, by including an additional loss port. Light incident onto the photonic-crystal slab can be reflected through different channels: a non-resonant (direct), and a resonant loss channel. The direct channel corresponds to the Fresnel reflection of the layered system, while the resonant channel is created by coupling to a (leaky) waveguide mode. This waveguide mode has a well-defined dispersion relation and coupling at a specific frequency occurs via diffraction. The asymmetric Fano line shape can be explained by interference between the direct channel and the resonant channel. A loss port is added to include the effects of scattering from surface roughness and diffraction into the substrate. All input and output ports of the system are linked by a direct-scattering matrix C and a resonant scattering matrix U. Coupling of the resonant mode to the three different ports is described by the complex coefficients d_j.

The direct channel contains the reflection and transmission coefficients of

the layered system. At each angle of incidence, we use Maxwell-Garnett's effective-medium theory [34, 35] to describe the photonic crystal layer as a birefringent layer with refractive index n_{eff}. We then calculate the Fresnel reflection and transmission coefficients [43] of the layered system shown in figure 3.2(a), incorporating the known refractive-index dispersion of GaAs [39], that includes absorption for wavelengths shorter than 950 nm. Taking the loss port into account, we write the scattering matrix for the direct process as

$$C = \begin{pmatrix} r_1 & t & 0 \\ t & r_2 & 0 \\ 0 & 0 & 1 \end{pmatrix}, \tag{3.1}$$

where r_1, r_2 and t are the (complex) Fresnel reflection and transmission coefficients for the electric field.

The resonant channel, due to the leaky waveguide, is formed by the photonic crystal layer. As pictured in figure 3.2(b), the incident light is partially diffracted into the waveguide and confined by internal reflection. The light that is diffracted back, interferes with the directly reflected and transmitted light (ports 1 and 2 in figure 3.2). The resonance angular frequency ω_0 is determined by the dispersion relation of the waveguide mode involved. The average lifetime in the waveguide is parameterized by an escape rate γ and is a function of angle of incidence. The scattering matrix describing the resonant channel is given by

$$U_{jk} = \frac{d_j d_k}{i(\omega - \omega_0) + \gamma}. \tag{3.2}$$

where ω is the angular frequency of the incident light.

In our experiment, the tapered form of the holes effectively ensures that there is a waveguide in the upper part of the photonic crystal layer. However, since the refractive index of the substrate is higher than the effective index of the photonic crystal layer, light propagating in the waveguide mode can still leak to the substrate without being diffracted. In order to incorporate these losses in the model, we added a third port to the scattering matrix [port 3 in fig. 3.2(b)]. In this relatively simple model, we assume that a fraction of the light is irreversibly lost by leaking out of the resonant channel. This is valid as long as losses in the resonant channel are much larger than losses in the direct channel. This generally holds when the losses in the direct channel are small, since in this case the interaction length for light in the resonant channel is much larger than that in the direct channel. The effect of adding a loss port is that the reflectivity no longer reaches 100% nor 0% as is the case for a system without loss [30].

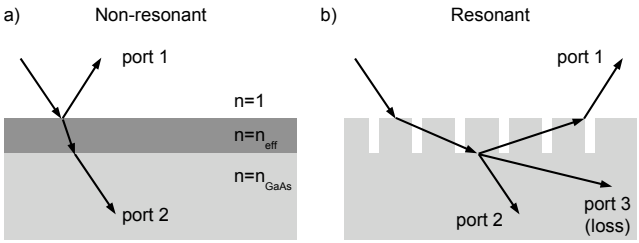

Figure 3.2. Model for the non-resonant (a) and resonant (b) channels in the model. The numbers indicate the different ports in the scattering matrix model. (a) The non-resonant channel is modeled by applying effective medium theory to the photonic-crystal layer and calculating the Fresnel reflection and transmission coefficients of the layered system. (b) For the resonant channel, the incident light is diffracted into a waveguide mode, which can diffract back to ports 1 and 2, but can also propagate into the substrate (port 3) constituting loss.

Time-reversal symmetry and energy conservation put the following constraints on the coupling constants d_j [30]

$$\sum_k C_{jk} d_k^* = -d_j \tag{3.3}$$

$$\sum_j |d_j|^2 = 2(\gamma + \Gamma), \tag{3.4}$$

where Γ is the loss rate from the resonant mode. Furthermore, the diffractive coupling to the resonant mode is assumed to be equally large on both sides of the photonic crystal slab (i.e. $|d_1| = |d_2|$). With these constraints, we can write the coupling constants d_j in terms of the Fresnel coefficients and the parameters ω_0, γ and Γ. The reflectivity $R = |U_{11} + C_{11}|^2$ for the system is then given by

$$R = \left| \frac{i\left[(\omega - \omega_0) r_1 \mp \gamma t\right] + \Gamma r_1}{i(\omega - \omega_0) + \gamma + \Gamma} \right|^2 . \tag{3.5}$$

After setting the fill fraction and the thickness of the photonic crystal slab once, the Fresnel coefficients are fixed and there are only three free parameters left in the model: the resonance angular frequency ω_0, and the loss rates γ and Γ.

The dashed curves in figure 3.1 show the best fit of the model to our data. Although the fits deviate on detail from the measurements, qualitatively all elements of the measurements are contained in the model. We attribute most deviations from the measurements to simplifications we made with respect to

the vertical shape of the air holes. Also, Maxwell-Garnett effective medium theory is only valid when all relevant length scales in the system are much smaller than the wavelength. This condition is not fulfilled in our structure.

Using the model described here, one can understand the origin of the change in asymmetry of peak shape when changing the angle of incidence. Since the peak is a product of interference between a resonant Lorentzian line and a non-resonant direct contribution, the relative phase between these two contributions will determine the asymmetry of the resulting line shape.

The Fresnel reflection coefficient (r_1) for p-polarized light, for a dielectric interface, vanishes and changes sign at Brewster's angle. This is shown in the insets of figure 3.1, for an interface between air and a dielectric with $n_{\text{eff}} = 2.5$. It is exactly this change of sign that causes the line shape to vary from red-tailed asymmetric to Lorentzian at Brewster's angle to blue-tailed asymmetric for larger angles. For s-polarized light, we observed the line shape to be blue-tailed asymmetric for all angles of incidence, which confirms this explanation since the Fresnel reflection coefficient for s-polarized light is always negative.

The rough shape of the holes causes relatively broad spectral features that are easily resolved. The fact that we are able to describe our data with an extended version of a coupled mode theory and observe a change in asymmetry of the spectral line shows that the description is robust and also valid for less-than-perfect crystals.

3.4 Conclusion

In summary, the reflection spectra from a 2-D photonic-crystal slab show a large asymmetric peak on top of an oscillating background. With increasing angle of incidence, the asymmetry of the peak reverses. We explained all observations with a scattering matrix model [30] that is extended to include losses. The reversal of the asymmetry is a consequence of the change in sign of the Fresnel reflection coefficient when crossing Brewster's angle. The 'model gives good qualitative as well as quantitative agreement with the measurements, while having only three fit parameters describing the resonance frequency and lifetime of the resonant waveguide mode, and its losses.

Although the model does not predict the position of the resonances for a given structure, these can be estimated for the case of a true waveguide (i.e. $n_{\text{eff}} > n_{\text{subs}}$, with n_{subs} the refractive index of the substrate) [44, 45]. The model can easily be extended to incorporate multiple uncoupled waveguide modes, thus forming a powerful tool in explaining the observed phenomena in reflection spectra from 2-D photonic crystals.

Chapter 4

Imaging of a Fano resonance in a two-dimensional photonic-crystal slab

We investigate a resonance of a photonic-crystal slab by imaging the reflection from the slab of a strongly focused beam of monochromatic light. Polarization-dependent k-space imaging allows us to identify the resonance as originating from diffraction into a TM_0 waveguide mode. In real-space images of the reflection, we can spatially separate the direct and resonant contributions of the Fano resonances that are observed in the reflection spectra. We observe decay lengths of the resonant contributions of up to 7 μm. From the normal-incidence reflection spectrum we determine the escape rate. Combined, this allows us to estimate a group refractive index $n_g = 2.6$ and a phase index $n_{eff} = 1.5$ of the resonant mode.

4.1 Introduction

Reflection spectra from waveguides that are patterned with a periodic array of holes, so-called photonic-crystal slabs, contain a multitude of sharp, resonant features. These features are caused by diffraction from the periodic array of holes into a (leaky) waveguide mode. Light that is coupled into these leaky modes diffracts back, and interferes with the direct (Fresnel) reflection from the layered structure. This interference leads to the typical asymmetric (Fano) line shape as described in the previous chapters. Usually, information about the dispersion of these resonances is only obtained by measuring spectra at different angles of incidence [20]. These spectra are compared to calculations, and information about the resonance is distilled, most notably the specific waveguide mode that the light is coupled into. This method has the obvious disadvantage that it only works well for structures of which the constitution is reasonably well known, but even then, complications arise, since TE waveguide modes can show up in *p*-polarized reflection spectra, and vice-versa [46].

In this chapter, we use a different approach to obtaining information about a specific resonance of a photonic-crystal slab. We use a strongly focused, monochromatic beam to illuminate the photonic crystal at a specific spot. We image the reflection of the sample both in real space and in k-space. From the k-space images, we were able to unambiguously identify the resonance as a first-order diffraction process into the TM_0 waveguide mode. Real-space images allow us to separate the resonant and non-resonant contributions of the Fano resonance. In these images, we can measure the decay length of the resonant contribution directly. From this length and the decay time, obtained from a separate measurement of the reflection spectrum, we can determine the group refractive index of the leaky waveguide mode.

4.2 Sample

The photonic-crystal slab used in this chapter is made using the techniques described in Ch. 2. It consists of a 160 nm thick, free-standing membrane of $Al_{0.35}Ga_{0.65}As$ that is patterned with a 250×250 μm^2 large square array of holes with a radius $r \approx 120$ nm and a lattice constant $a = 480$ nm. Due to a small lattice mismatch of the lattice constants of the AlGaAs and the GaAs substrate, there is a small compressive strain in the membrane layer, that is released when the sacrificial layer is etched. This causes the membrane layer to buckle up, resulting in a variable distance between the membrane and the GaAs substrate when moving along the membrane.

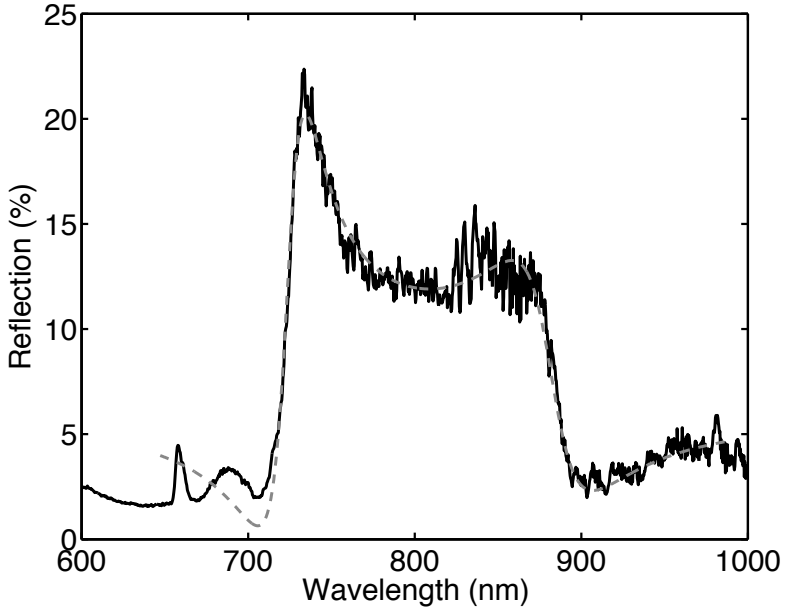

Figure 4.1. Normal-incidence reflection spectrum of the photonic-crystal membrane (solid curve). Two asymmetric Fano resonances are visible, centered around wavelengths of 725 nm and 882 nm. The dashed curve is a fit of a Fano model with two resonances to the measurements, as discussed in the text.

4.3 Normal-incidence reflection spectrum

The photonic-crystal slab two distinct resonances in the near-infrared spectral region. Figure 4.1 shows the reflectivity of the membrane at normal incidence, as a function of the wavelength of the incident light. To record this curve, we used an unpolarized, fiber-coupled xenon lamp and imaged the 50 μm-diameter fiber facet onto the sample, while limiting the numerical aperture of the incident light to < 0.01. The reflected light was collected with a 200 μm core-size fiber and sent to a grating spectrometer*, to analyze the spectral content. The detected signal was normalized to the reflection from a silver mirror.

The measurement in Fig. 4.1 shows two asymmetric (Fano) resonances, centered around wavelengths of 725 nm and 882 nm. We ascribe the small peak that is observed around 670 nm to luminescence at the band edge of

*Ocean Optics USB2000, resolution 1.2 nm.

the AlGaAs material, and not to a resonance that is caused by the patterning of the membrane. This assumption is confirmed by the fact that the peak does not change spectral position when changing the angle of incidence of the illumination. To obtain a better understanding of the reflection spectrum, we used the Fano model described in Ch. 2. In this model, the reflection is given by

$$R = \left| r - \sum_p \gamma_p \frac{r \pm it}{i(\omega - \omega_p) + \gamma_p + \Gamma_p} \right|^2 , \tag{4.1}$$

where r and t are the reflection and transmission coefficients of the direct contribution, respectively, ω is the angular frequency of the light, ω_p the resonance angular frequency, γ_p the radiative loss, and Γ_p the irreversible (scattering) loss of waveguide mode p. In order to fit this model to the measurements, we assumed that the reflection r is constant over the wavelength range. Furthermore, we assumed that the transmission t is given by $|t|^2 = 1 - |r|^2$, i.e. that there are no losses in the direct channel. We checked this assumption by adding some loss in the direct channel (i.e., $|r|^2 + |t|^2 < 1$). This addition of loss did not change the overall quality factor $Q = \omega_p/(\gamma_p + \Gamma_p)$ of the resonances significantly. It does change the relative contributions of γ_p and Γ_p in Eq. (4.1), which makes a reliable independent fit of these two parameters impossible. The buckling of the membrane structure causes a variable distance between the free-standing membrane and the GaAs substrate. This results in an ambiguity of both the precise angle of incidence and the vertical structure of the different layers. Combined, this makes it impossible to calculate the Fresnel coefficients for direct reflection and transmission for this structure, contrary to the structure discussed in chapters 2 and 3.

The dashed curve in Fig. 4.1 shows the best fit of this model to the measurements. The fit parameters are summarized in Table 4.1. The fit was performed using two resonances with opposite symmetry [set by the $\pm$ sign in Eq. (4.1)]. The symmetry of the two resonances in Fig. 4.1 is determined by the symmetry (even or odd) of the waveguide modes relative to the plane in the middle of the slab [30]. For the wavelength range of these measurements, the only two waveguide modes that are below cut-off are the TM_0 and the TE_0 waveguide mode. Since these two waveguide modes have opposite symmetry, we conclude that each of the two resonances is caused by coupling to a different waveguide mode. Since the phase of the direct reflection cannot be determined from this measurement, it is impossible to tell from the shape of the resonant peaks, which resonance corresponds to which specific waveguide mode, however.

Table 4.1. Fit parameters and 95% confidence intervals of the two-resonance Fano model.

Parameter	Value	
	Resonance 1	**Resonance 2**
r	0.238 ± 0.002	
$2\pi c/\omega_p$ (nm)	725.4 ± 0.3	881.8 ± 0.6
Q	53 ± 1	37 ± 1

4.4 Imaging of the resonance

In order to gain more insight into the character of the resonance around 725 nm, we image the reflection of a strongly focused beam of light from the photonic crystal slab. Figure 4.2 shows a schematic overview of the setup used in the experiments. Light from a tunable picosecond Ti:Sapphire laser or from an external-cavity tunable diode laser is attenuated using neutral-density filters (ND), sent through a single-mode optical fiber (SMF), and collimated with a $f = 5$ cm lens to a beam of ~ 1 cm diameter. The beam is polarization-filtered using a polarizer (P). A glass plate that is anti-reflection coated on one side is used as a beam splitter (BS) to direct the beam to an aspheric lens L3 ($f = 8$ mm, NA $= 0.5$), that focuses the light onto the photonic-crystal membrane. The membrane is aligned such that the beam axis is parallel to its surface normal. The reflection from the membrane is collected with the same lens and sent back onto the beam splitter. The reflected light is transmitted through this beam splitter, and the surface of the photonic crystal membrane is imaged onto a CCD camera using a $f = 250$ mm lens L4. A second lens L5 ($f = 125$ mm) can be inserted into the imaging setup, to make a k-space image of the photonic crystal reflection. The solid and hatched beam paths depicted in Fig. 4.2 show the imaging of the real-space and k-space reflection, respectively. A polarization analyzer was placed between lenses L4 and L5 to probe the polarization properties of the reflected light.

For our experiments, we selected a part of the membrane that was locally parallel to the GaAs substrate, to minimize the pattern of interference fringes caused by the (partial) reflection from the substrate of light that was transmitted through the membrane. We recorded the real-space and k-space reflection image of an unpatterned piece of the substrate next to the membrane, as a reference. We aligned the crystal axes of the photonic crystal such, that the ΓX-directions were parallel to the horizontal and vertical directions of the images.

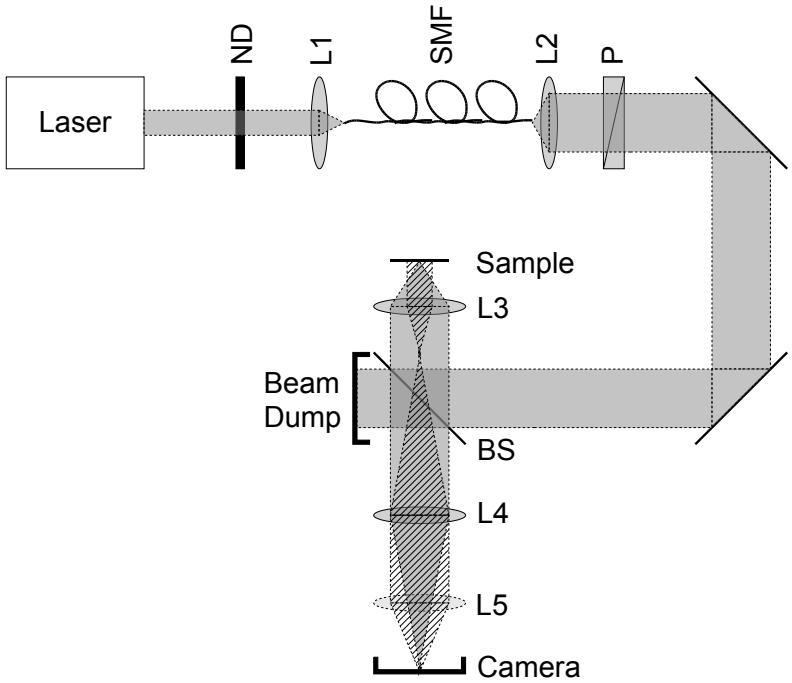

Figure 4.2. Experimental setup. Light from a tunable laser is focused on the photonic-crystal sample via a beam splitter (BS). By inserting the lens L5, the imaging is switched from real-space imaging (solid beam path) to k-space imaging of the reflection from the photonic crystal slab (hatched beam path). Details of the setup are found in the text.

4.4.1 k-space imaging and polarization properties

Figure 4.3(a) shows the recorded reflection in k-space, when the photonic-crystal slab was illuminated at a wavelength of 762.5 nm, red-detuned from the resonance at 725 nm, with horizontal polarization. Most obviously, a dark and bright ring pattern, that is centered around the normal-incidence (Γ) point (the center of the image) is visible. These Fabry-Perot fringes are caused by the partial reflection from the GaAs substrate underneath the photonic-crystal slab, that interferes with the reflection from the slab. The fact that the rings are concentric indicates that locally the membrane is parallel to the GaAs substrate.

Besides the Fabry-Perot fringes, a resonance is observed on the left and right sides of the normal-incidence point. Most obviously, the dark minimum of the Fano resonance is observed. The azimuthal angular dependence of the

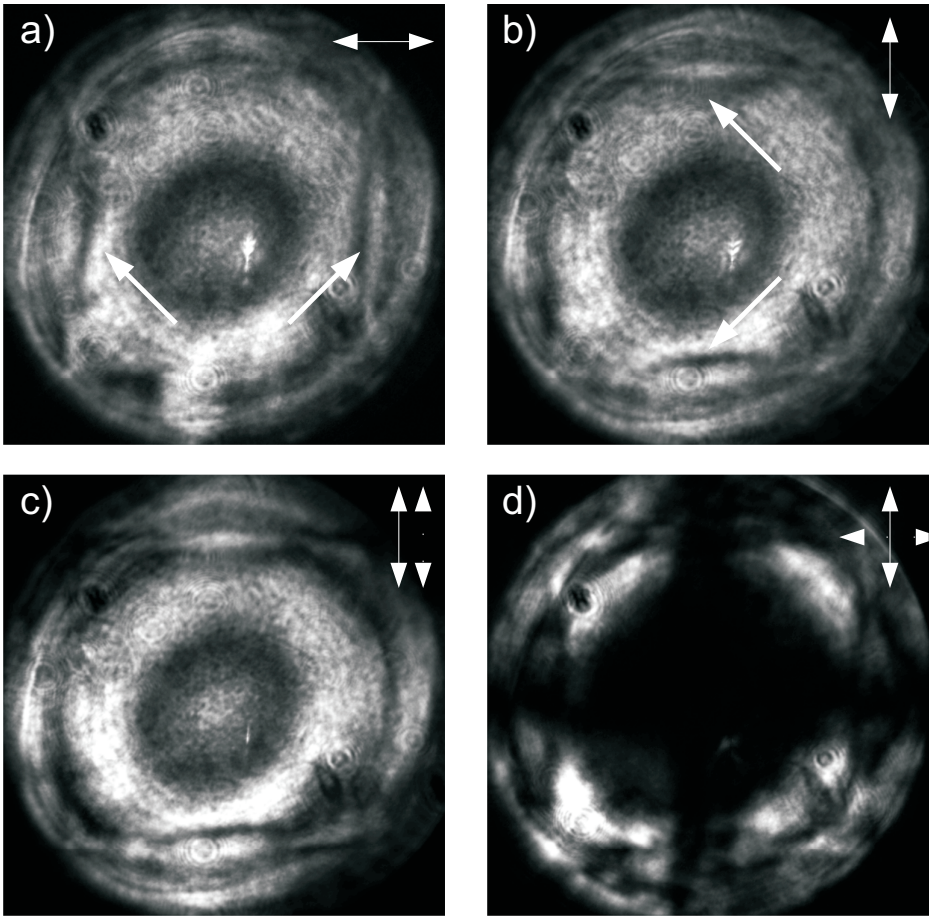

Figure 4.3. k-space image of the reflection of the photonic-crystal slab, when illuminated at a wavelength of 762.5 nm. (a) and (b) show the reflection when no analyzer is placed in the detection path and the illuminating light was polarized horizontally (a) and vertically (b). In these images, a resonance is visible (indicated with the arrows). In figures (c) and (d), the illumination was polarized vertically, and an analyzer was placed in the detection path, either parallel (c) or perpendicular (d) to the polarizer. The full image spans a numerical aperture $NA = 0.5$. The solid arrows in the upper right corner of the figures indicates the polarizer setting, the dashed arrows indicate the analyzer settings.

resonance suggests that the resonance originates from the $(\pm 1, 0)$ reciprocal lattice points. The resonances are not visible in the vertical direction. When the polarization of the illumination is rotated 90° (b), only the resonances in the $(0, \pm 1)$ direction are visible. A comparison with a calculation of the waveguide modes of a uniform slab with an effective refractive index (not shown), and folding these modes back into the first Brillouin zone, confirms that the resonance is caused by coupling to the TM_0 waveguide mode, by diffraction from the (1,0) reciprocal lattice points. On changing the wavelength towards the blue, the resonances are observed to shift towards the Γ-point. This allows us to identify this resonance with the resonance around 725 nm, observed in the normal-incidence reflection spectrum.

Figures 4.3(c) and (d) show a polarization analysis of the reflection for vertically polarized light. In Fig. 4.3(c), an analyzer is placed parallel to the polarization of the incident light. In Fig. 4.3(d), the analyzer is placed perpendicularly. Most of the reflected light is polarized the same as the incident light, except for four small areas in the (diagonal) ΓM-directions. Along the directions of high symmetry, the resonances of a photonic-crystal slab can be characterized by the polarization properties of the radiating field, as either *s*- or *p*-polarized [38]. The incident polarization is aligned with the ΓX symmetry direction, such that it is *p*-polarized in the vertical, and *s*-polarized in the horizontal direction. Since these are the eigenpolarizations of the resonant modes, no polarization mixing occurs and the reflected light has the same polarization as the incident light. Away from the ΓX directions, the incident light is both *s*- and *p*-polarized, nor polarized in an eigenpolarization of the resonant mode. Light that is coupled into the leaky waveguide mode will therefore undergo a polarization rotation, which shows up in the *k*-space image with crossed polarizers [Fig. 4.3(d)].

4.4.2 Real space imaging

Figure 4.4 shows the real-space reflection of the photonic-crystal slab, using the same illumination conditions as before, for horizontally (a) and vertically (b) polarized illumination, on a logarithmic scale. Besides a very bright spot where the slab is illuminated, two tails are visible, in the direction of the incident polarization. These tails are formed by light that is coupled into a leaky waveguide mode, and propagates in this mode before being diffracted back. The fact that we only observe a tail parallel to the incident polarization confirms again that the mode we couple into is a TM-like waveguide mode. The distortions in the images are caused both by the fact that the membrane is not flat, and could also be due to the fact that a resonantly excited mode propa-

gates in the direction of the group velocity, which is not necessarily the same as the direction of the reciprocal lattice vector that causes the resonance [47, 48].

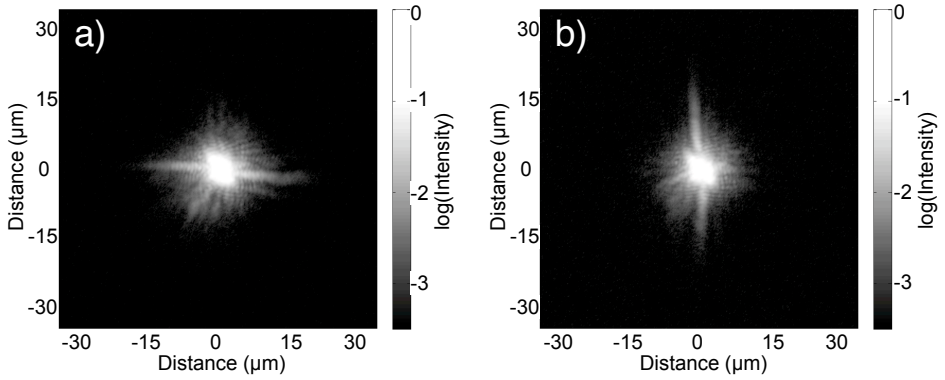

Figure 4.4. Real space image of the reflection of the photonic-crystal slab, when illuminated at a wavelength of 762.5 nm, on a logarithmic scale, for horizontally (a) and vertically (b) polarized illumination. The two long tails that emerge from the pump spot are caused by light that is resonantly coupled to a leaky waveguide mode of the slab, and that decays exponentially from this waveguide mode.

In Fig. 4.5 we show a cross-section of the vertical resonance of Fig. 4.4(b). To obtain this plot, we summed the intensity over a horizontal box of width 4.5 μm, in order to capture all intensity in the resonant tails. In this image, the direct and resonant contributions to the Fano resonance are spatially separated [49]. The central peak is Gaussian in shape, and corresponds to a direct image of the illuminating spot. As a comparison, the reflection from an unpatterned piece of the sample is given as the dash-dotted curve, showing a perfect agreement with the peak of the measured curve. The resonant tails decay exponentially on both sides of the central spot. A fit of a single exponential to these tails is shown by the dashed lines. The resonant contribution can be traced over 2.5 orders of magnitude, and up to a distance of 30 μm away from the center of the illumination spot. An interference between the resonant and non-resonant contributions, as observed in similar experiments with surface-plasmon polaritons [49], was not observed in these measurements.

We measured the real-space image of the resonance for different wavelengths from 700 to 800 nm. From these images, we obtained the decay length of the resonant contribution by fitting a single exponential to the intensity of the resonant tail. The result of these fits are shown in Fig. 4.6 and varies from ~ 3 μm at wavelengths around 750 nm to ~ 7 μm at 795 nm.

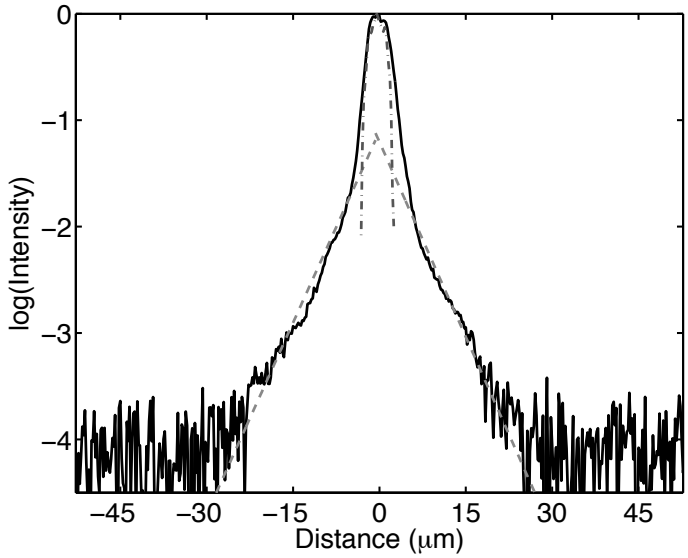

Figure 4.5. Logarithmic plot of the measured reflected intensity, taken along the vertical resonance in Fig. 4.4(b) (solid curve). The two contributions to the Fano resonance are spatially separated. The reflection arising from the direct (Fresnel) contribution is giving rise to the central spot, whereas the exponentially decaying tails are caused by light that is resonantly coupled to a waveguide mode. The dashed lines show a linear fit to the resonant tails. The dash-dotted curve is the profile of the pump spot, measured on an unpatterned region of the substrate.

The decay length l of the resonant tails can be parametrized by

$$l = \frac{v_\mathrm{g}}{\gamma + \Gamma} = \frac{\lambda}{2\pi n_\mathrm{g}} Q, \tag{4.2}$$

where v_g and n_g are the group velocity and the group index, respectively, γ and Γ are the escape rates as defined before, and λ is the wavelength of the light in vacuo. Q is the quality factor of the resonance, as defined before. Using this equation, we determine the group refractive index at normal incidence (725 nm) to be 2.6. Although this value is small compared to the refractive index of the AlGaAs material ($n \approx 3.5$), it is large compared to the effective index of the TM_0 waveguide mode of the slab, which we estimate to be $n_\mathrm{eff} \approx 1.5$. This estimate was made noting that the resonance at the Γ point occurs when the condition $\lambda = n_\mathrm{eff} a$ is met, and assuming no avoided crossing around the Γ-point. At this wavelength, the TM_0 waveguide mode is still very close to cut-off, which explains why the calculated effective index of the waveguide mode

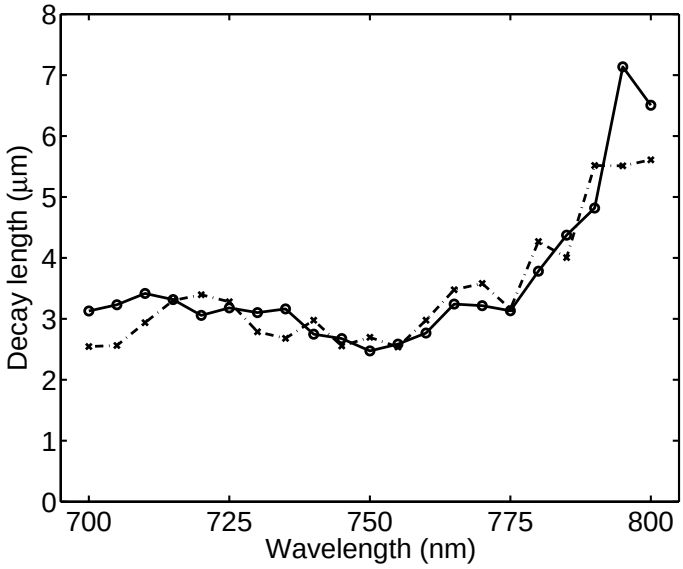

Figure 4.6. Decay length of the $TM_0(1,0)$ resonance as a function of wavelength. The circles and crosses show the fitted decay length on either side of the non-resonant reflection spot. The lines are guides to the eye.

is so close to the refractive index of the surrounding air. The group index is actually comparable to both the group index calculated from the waveguide dispersion of an unpatterned waveguide, and to the group index that is caused by the refractive-index dispersion of the AlGaAs material. We do not observe a considerable increase of the group index around the band gap at the Γ point. This is due to our illumination scheme where we illuminate the photonic crystal with a high numerical aperture. We therefore excite the resonance at different angles of incidence, but the resonance that is excited with the largest decay length, i.e. the highest group velocity, will be most pronounced in the imaging.

The variation of the decay length with wavelength can be explained as follows: both the group index and the decay time of the resonance change with changing angle of incidence. The group index is proportional to $(\partial\omega/\partial k)^{-1}$. At the Γ-point, an avoided crossing occurs. The resonant modes consist of standing waves, which causes $n_g \rightarrow \infty$. When moving the resonance away from the Γ point, the group index will lower, leading to a longer decay length. At the same time, the decay time will change [38], which also leads to a change in decay length, as observed in the measurements. Some precaution has to be taken with the resonance that is observed at 883 nm. With increasing angle

of incidence, we expect this resonance to split, and obtain a branch that shifts to lower wavelengths. Since this resonance can be linked to a TE waveguide mode, however, we do not expect this resonance to couple strongly to the TM-like resonance that is described in the rest of this chapter.

4.5 Conclusion

The imaging technique described in this chapter allowed us to directly measure the decay length of a photonic-crystal resonance. In principle, this decay length can be linked to the group refractive index at this specific wavelength. This would require exact knowledge of the variation of the resonance decay time with wavelength, which could be obtained by measuring the reflection spectra of the photonic-crystal slab at different angles of incidence, which in turn would also yield the group refractive index. The advantage of the technique used in this chapter lies in the fact that an unambiguous identification of the specific waveguide mode and reciprocal lattice vector is possible using a k-space image. Moreover, it allows to spatially separate the resonant and non-resonant contributions of a Fano resonance, which is principally impossible using a series of reflection spectra.

Part II

Metal hole arrays

Chapter 5

Enhanced coupling between plasmons in hole arrays with periodic dielectric antennas

We compare the angle-dependent transmission spectra of a metal hole array with dielectric pillars in each hole with that of a conventional metal hole array. The pillars enhance the optical transmission as well as the interaction between surface-plasmon modes. This results in an observed splitting $\Delta\omega/\omega$ as large as 6%, at normal incidence, for the modes on the pillar side of the array.

This chapter is based on D. Stolwijk, E. F. C. Driessen, M. A. Verschuuren, G. W. 't Hooft, M. P. van Exter, and M. J. A. de Dood, *Enhanced coupling of plasmons in hole arrays with periodic dielectric antennas*, Opt. Lett. **33**, 363–365 (2008).

5.1 Introduction

Metal films perforated with an array of subwavelength holes have intrigued researchers ever since the discovery that these arrays show extra-ordinary transmission of light [50]. It is generally accepted that the enhanced transmission is mediated by surface plasmons, electro-magnetic surface waves that are bound to a metal-dielectric interface. On a smooth interface these waves cannot be excited directly because their momentum is larger than that of light incident from the dielectric. Diffraction from a regular array of holes enables efficient excitation of the plasmon modes and increases the optical transmission. Due to this surface-plasmon excitation, the transmission of the hole array exceeds that, what is expected based on the transmission through a set of independent single holes [51].

The transmission spectra of metal hole arrays show a number of asymmetric resonances that correspond to different diffraction orders. Each of the resonances can be labeled by a specific reciprocal lattice vector [52]. The asymmetric lineshape of the resonances can be explained in terms of a phenomenological (Fano) model [29, 53–55]. Each peak features a maximum in transmission and a profound minimum, known as Wood's anomaly [56]. The frequencies of these features depend on the angle of incidence and can be compared to the dispersion relation of a plasmon on a smooth surface, folded back to the first Brillouin zone of the periodic lattice [52].

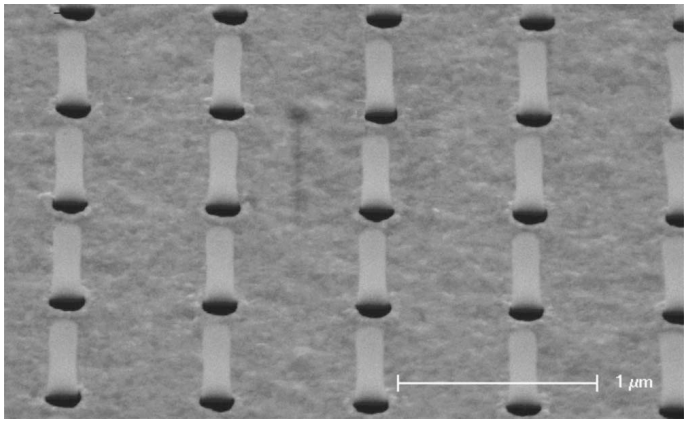

Figure 5.1. SEM image of the metal hole array created using an imprinting technique. The holes are 132 nm in diameter and each hole contains a ∼650 nm long glass pillar. The array has a lattice constant $a = 760$ nm.

In this chapter we study the polarization-dependent transmission spectra of metal films perforated with a square lattice of subwavelength holes. We compare the transmission of an array with a dielectric pillar in each of the holes with that of a conventional hole array. Transmission spectra of conventional hole arrays have been studied previously [57,58], and show that different modes can be excited depending on the input polarization. The p-polarized input light dominantly excites plasmon modes which propagate in the direction parallel and anti-parallel to the projected wave vector of the incident light. For small angles of incidence, coupling to modes that propagate in the approximately orthogonal direction is inefficient. We show that the excitation of these modes is strongly enhanced for the hole array with pillars. The pillars in the holes act as antennas that enhance the coupling to these modes. This provides a way of controlling the interaction between light and surface-plasmon modes.

5.2 Experiment

The metal hole arrays in the experiment were made using an imprinting technique. An array of pillars was defined by e-beam lithography and was used to create a rubber stamp. A replica of the array was created by pressing the stamp into a layer of liquid sol-gel glass. This second array was then coated with a layer of gold. The gold was selectively removed from the pillars with a wet etch, by making use of the fact that the gold layer deposited on the side of the pillars is thinner than the layer on the substrate. The result is a metal hole array with a $\sim$650 nm long glass pillar sticking out of each hole, as shown in Fig. 5.1. The 0.5×0.5 mm^2 array was created on an AF45 glass substrate with $n \approx 1.52$. A 100 nm thick layer of sol-gel glass with a refractive index $n \approx 1.41$ was left between the substrate and the gold layer. The gold layer is 200 nm thick and is perforated by a square array of pillars with a lattice constant $a = 760\pm4$ nm* and a diameter $d = 135\pm5$ nm. After measuring the transmission of this array, we selectively removed the glass pillars using hydrofluoric acid, to create a conventional hole array, and repeated the transmission measurement.

The optical transmission of the hole array was measured using an incandescent lamp coupled to a 200 μm multimode optical fiber. A set of lenses was used to create a $\sim$300 μm diameter spot on the sample. The transmitted light was sent to a fiber-coupled grating spectrometer with a CCD detector (resolution 1.2 nm) to measure the spectral content. Apertures limited the numerical aperture of the incident and transmitted light beam to less than

*The lattice constant was obtained from diffraction measurements with an He-Ne laser.

0.01. Polarizers were placed in parallel parts of the incident and transmitted beam to control the polarization. To measure the angular dispersion, the substrate was placed on a rotation mount with the rotation axis aligned to the $(0, 1)$-direction of the hole array. The wave vector of the incident light was in the plane perpendicular to this direction.

Figure 5.2 shows measured transmission spectra (normalized to the lamp spectrum) of the metal hole array both before (dashed lines) and after (solid lines) removing the pillars. Spectra are shown for normal incidence (bottom) and 15° angle of incidence (top). The maximum transmission decreases, and at the same time the resonance narrows while the maximum shifts to shorter wavelengths. The observed change in line shape corresponds to a Fano resonance for which the amplitudes of both the direct and resonant channel, as well as the linewidth of the resonance, are reduced by a factor 2. Note that the spectral positions of the transmission minima do not shift when the hole size is reduced [56, 59]. The marginal shift that we do observe is attributed to the fact that the pillars change the effective index of the surface plasmon.

5.3 Coupling to surface plasmons

Each resonance in the transmission spectra can be labeled with a specific reciprocal lattice vector. The labels (i, j) in Fig. 5.2 refer to the reciprocal lattice vector $\vec{G} = i\vec{G}_{\mathrm{x}} + j\vec{G}_{\mathrm{y}}$, where $\vec{G}_{\mathrm{x,y}}$ are the two basis vectors of the reciprocal lattice. The condition for exciting a surface-plasmon mode is given by:

$$\vec{k_{\parallel}} = \vec{k}_{\mathrm{SP}} + \vec{G}, \tag{5.1}$$

where $\vec{k}_{\parallel}$ is the projection of the wave vector of the incoming light onto the metal-dielectric interface, and $\vec{k}_{\mathrm{SP}}$ is the propagation constant of the surface plasmon. To describe the dispersion, we approximate the propagation constants of the surface plasmons on both sides of the metal hole array with that of a plasmon on a smooth metal-dielectric interface:

$$k_{\mathrm{SP}}(\omega) = \frac{\omega}{c}\left(\frac{\epsilon_{\mathrm{d}}\epsilon_{\mathrm{m}}(\omega)}{\epsilon_{\mathrm{d}} + \epsilon_{\mathrm{m}}(\omega)}\right)^{1/2}, \tag{5.2}$$

where c is the speed of light, ϵ_{d} is the dielectric constant of the dielectric and $\epsilon_{\mathrm{m}}(\omega)$ is the frequency-dependent dielectric constant of the metal.

Figure 5.3 shows grayscale plots of the transmission as a function of the angle of incidence (horizontal axis) and the wavelength (vertical axis) for the sample without pillars (top) and with pillars (bottom). The dark bands in

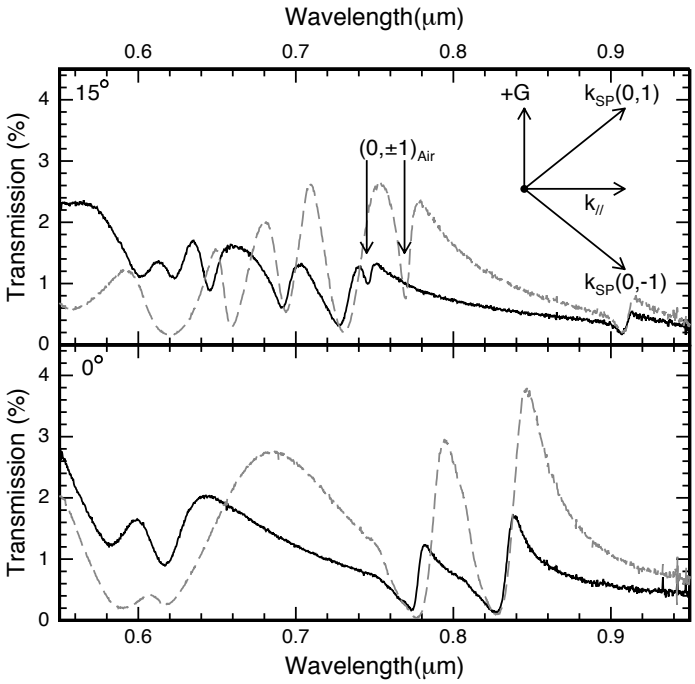

Figure 5.2. Transmission spectra of a conventional metal hole array (solid curve) and a metal hole array with pillars (dashed curve), for p-polarized light. Spectra are shown for normal incidence (bottom) and 15° angle of incidence (top). The arrows indicate the $(0, \pm 1)$ resonance for 15° angle of incidence. The inset shows the wavevector $\vec{k}_{\parallel}$, a reciprocal lattice vector $\vec{G}$ in the (0,1) direction and the propagation direction of the two (0,±1) surface-plasmon modes.

the figure correspond to the minima in the transmission spectra. The white curves are the frequencies calculated from Eqs. (5.1) and (5.2) for different reciprocal lattice vectors $\vec{G}$, using the tabulated frequency dependence of the dielectric constant of gold [60], and an effective index of $n \approx 1.46$ for the glass substrate*. A distinction is made between surface-plasmon modes on the air side (dashed curves) and on the glass side (solid curves). The $(\pm 1, 0)$ and $(0, \pm 1)$ modes on the air side are degenerate at normal incidence. When the angle of incidence is changed, the degeneracy is lifted and the resonance splits into a $(1, 0)$, a $(-1, 0)$, and a degenerate $(0, \pm 1)$ resonance. The $(1, 0)$ and $(-1, 0)$ modes have a strong dispersion, because $\vec{k}_{\parallel}$ and $\vec{G}$ are parallel. For the

*The effective index is based on the calculated propagation constant of a surface plasmon on an interface of gold with a 100 nm layer of sol-gel glass.

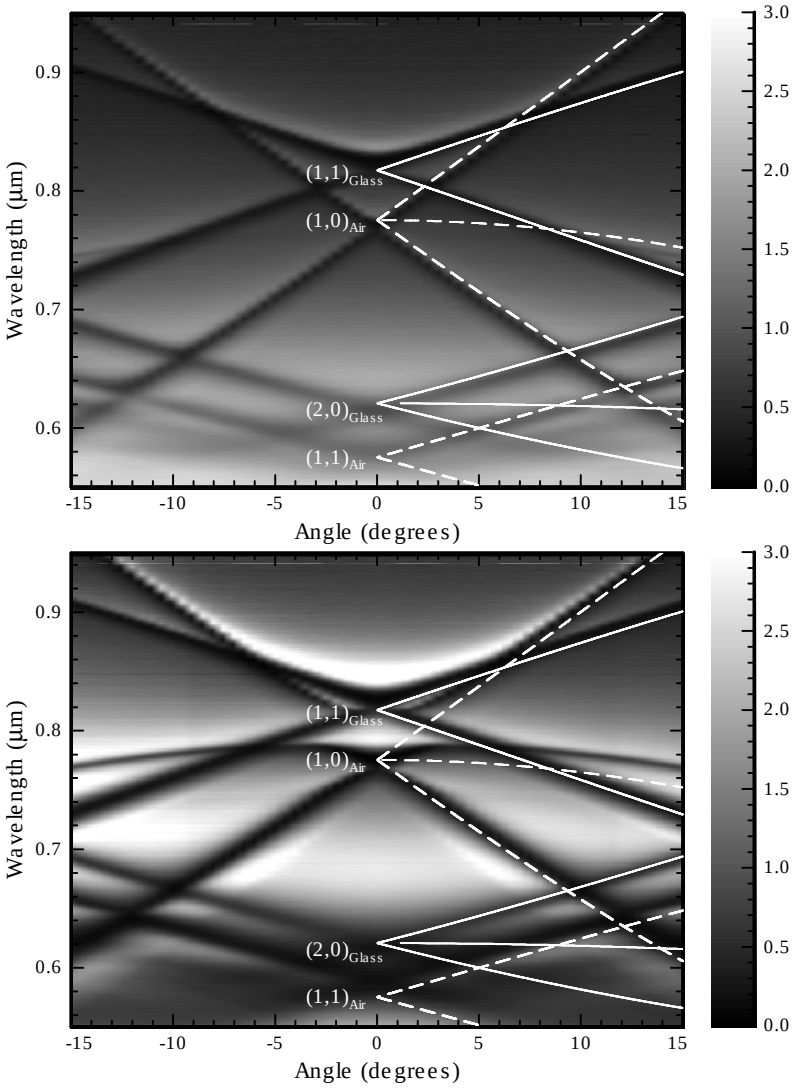

Figure 5.3. Grayscale plots of the measured transmission as a function of angle of incidence and wavelength, for the metal hole array without pillars (top) and with pillars (bottom). The grayscale ranges from 0 to 3% transmission. The white curves indicate the frequencies calculated from Eqs. (5.1) and (5.2). The solid curves are for modes on the glass side, while the dashed curves are for modes on the air side.

$(0, \pm 1)$ modes the dispersion is limited, because $\vec{k_{\parallel}}$ and $\vec{G}$ are perpendicular. For the conventional array the $(0, \pm 1)$ resonance is barely visible for small angles, consistent with earlier work [58]. The resonance is strikingly visible in the transmission of the array with pillars. The large difference in amplitude for this resonance is also clearly visible in the top part of Fig 5.2 (arrows).

For the geometry of our structure, the scattering plane coincides with a (1,0) direction of the square lattice. This plane is a mirror plane of the hole array, and the modes can be classified as either *odd* or *even* relative to this plane. The *p*-polarized input light has an *odd* H-field distribution relative to this plane, and therefore only plasmon modes with an *odd* H-field distribution can be excited. At normal incidence, this corresponds to plasmon modes that propagate in the direction of the E-field vector [61], i.e. the $(\pm 1, 0)$ directions. For finite angles of incidence it is possible to couple to a combination of $(0, \pm 1)$ modes. The direction of propagation of these modes is sketched in the inset of Fig. 5.2. The pillars in the holes do not change the symmetry, but act as antennas and affect the efficiency with which the modes are excited. The interaction between light and a dielectric pillar is strongest when the E-field is parallel to the long axis of the pillars. As a result, when pillars are placed in the holes, the coupling to the $(0, \pm 1)$ modes on the air side is enhanced for *p*-polarized light.

5.4 Coupling between surface plasmons

For both arrays, the angle dependent transmission in Fig. 5.3 shows that the $(\pm 1, 0)$ air modes have an almost-linear dispersion at sufficiently large angles of incidence. For smaller angles, this only holds for the conventional hole array. For the hole array with pillars, the $(\pm 1, 0)$ modes on the air side are clearly coupled. At normal incidence we observe two minima in the spectra at 775 and 825 nm. The minimum at 825 nm coincides with the minimum of the $(1, 1)$ glass modes. At normal incidence, the excited plasmon modes are standing waves. The resonances occur at different energies depending on the position of the nodes and anti-nodes of the standing waves relative to the holes [36, 54]. Without pillars, this energy difference is small and the splitting is not resolved. The pillars lower the energy only of the mode that has anti-nodes at the position of the pillars. For our array, with a filling factor of pillars of only 2.3%, this leads to an observed splitting of the resonances of 6% of the center frequency. Note that we used the separation between the minima as a measure of the splitting, because the minima do not shift when radiation losses are increased [56, 59]. We have compared this splitting to a two-band

model and to a model that uses the polarizability per unit volume. We find that the calculated splitting from these simplified models is much smaller than the observed splitting.

Increasing the filling factor of pillars will certainly increase the energy difference between the modes. However, a larger hole size also leads to larger radiation losses [54], and broadens the spectral features. This may obscure the effect. Similar effects are expected when dielectric hole arrays are placed on top of a metal hole array, although the interaction with p-polarized light is generally weaker, when compared to pillars. This kind of hybrid structures can be used to (locally) tune the dispersion of the surface modes of a metal film. By locally adding or removing pillars (holes), control of the excitation and propagation of plasmons on the wavelength scale can be achieved. When the interaction between plasmon modes can be increased, it becomes conceivable that two-dimensional periodic metal-dielectric structures exist that do not allow coupling of light waves to surface modes in any direction, for a certain range of frequencies. This effect would be analogous to the existence of photonic bandgaps in two-dimensional dielectric structures.

Chapter 6

Waveguide modes in solid-state index-matched metal hole arrays

We investigate the surface-plasmon modes of a metal hole array covered with a thin layer of glass. The glass layer diminishes the asymmetry of the structure, which leads to degenerate surface plasmon modes propagating on both sides of the metal hole array, when the glass layer is sufficiently thick. Besides the plasmon resonances, we observe a number of sharp dips in the transmission spectra, that are caused by waveguide modes in the glass layer on top of the metal hole array. Calculations of the dispersion of these guided modes show perfect agreement with the measurements.

This chapter is based on M. J. A. de Dood, E. F. C. Driessen, D. Stolwijk, M. P. van Exter, M. A. Verschuuren, and G. W. 't Hooft, *Index matching of surface plasmons*, Proc. SPIE **6987**, 698713 (2008).

6.1 Introduction

For sensing applications, it may be interesting to design structures in which the plasmons on different sides are index matched. In this chapter, we attempt to achieve index matching of the surface plasmon resonances on both sides of the metal hole array that was investigated in Ch. 5. For this purpose, it was covered with a thin ($\sim$ 400 nm) layer of sol-gel glass. This layer serves as an index matching layer and should make the surface plasmons that propagate on different sides of the metal film indistinguishable. The thin layer of glass however acts as a waveguide. The modes of this waveguide cause extra sharp resonances to occur in the transmission spectra. In section 6.2 we investigate these waveguide modes. In section 6.3 we discuss the effect of the finite thickness of the glass layers on the effective index of the surface plasmon modes, and show that it is possible to fabricate a structure where the surface-plasmon modes on both sides of the gold layer are degenerate.

6.2 Waveguide modes

In Fig. 6.1, we compare the transmission spectra for the metal hole array with (top) and without (bottom) the dielectric layer deposited on top of the structure. A number of changes is observed. Most notably, the increase of intensity of the peak that is associated with the (1,0) surface plasmon resonance on the glass side of the structure. The resonances belonging to the air side of the structure are shifted in wavelength, and a number of new features are observed in the spectra.

Figure 6.2 shows the measured transmission as function of the angle of incidence. Several strong, relatively broad, minima (black lines in Fig. 6.2) are clearly visible. These minima in transmission are associated with the Fano-type line shape caused by the coupling to a surface-plasmon mode. Two such modes can be observed, which correspond to a surface plasmon mode propagating on the substrate side and a surface plasmon mode propagating on the side covered with the dielectric layer. These modes can still be distinguished because the AF45 substrate has a higher refractive index ($n \approx 1.52$) than the sol-gel material ($n \approx 1.40$), making the structure slightly asymmetric.

In addition to the surface plasmon modes that are clearly visible, the new features that are observed in Fig. 6.1 also clearly show angular dispersion. For instance, at normal incidence a resonance appears at a wavelength of 700 nm, which cannot be explained by a surface plasmon mode. The extra resonances are characterized by a sharp symmetric dip instead of the asymmetric line

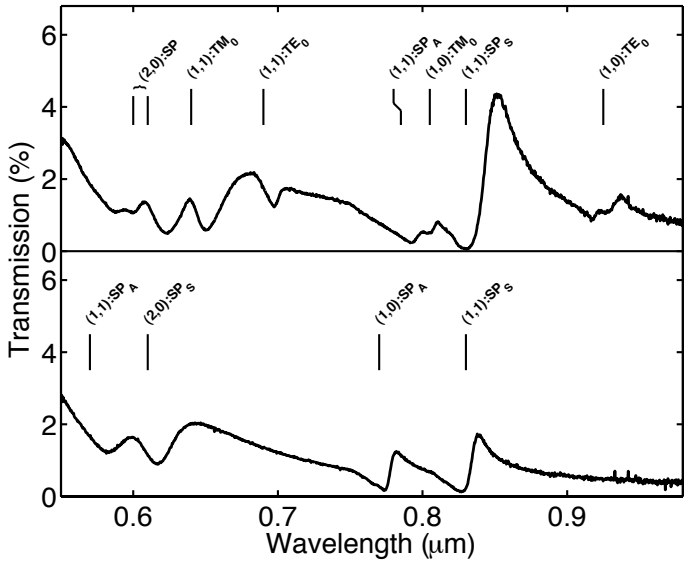

Figure 6.1. Measured transmission of the metal hole array of Ch. 5. The bottom curve shows the transmission spectrum for the structure without a glass layer on top, the top curve shows the transmission spectrum when a $\sim$ 400 nm thick layer of glass is deposited on top of the structure. The positions of the different resonances are indicated with lines, as well as the character of the resonances.

shape of the surface plasmon modes, and are caused by coupling to a waveguide mode supported by the dielectric superstrate [62]. Similar to the case of surface plasmons, the resonance condition to excite a mode is given by

$$\vec{k}_{\parallel} = \vec{\beta}_m + \vec{G}, \tag{6.1}$$

where $\vec{\beta}_m$ is the propagation constant of the mode, and $\vec{k}_{\parallel}$ and $\vec{G}$ are defined as in Ch. 5. For this layered structure, $\vec{\beta}_m$ has to be found numerically. The modes can be classified as either transverse electric (TE) or transverse magnetic (TM) depending on whether the E-field or the H-field vector is perpendicular to the surface normal of the structure. Following the notation of Ref. [63], we define the x-direction as perpendicular to the interface and the z-direction as the propagation direction of the guided mode. The dielectric constant $\epsilon(x)$ of our structure is stepwise continuous and equal to ϵ_1 for $0 \leq x$, ϵ_2 for $-d \leq x \leq 0$ and equal to 1 for $x \leq -d$. Here, d is the thickness of the dielectric layer, and ϵ_1, ϵ_2 and ϵ_3 are the dielectric constants of the metal, the dielectric layer and the dielectric above the structure, respectively. The metal-to-dielectric

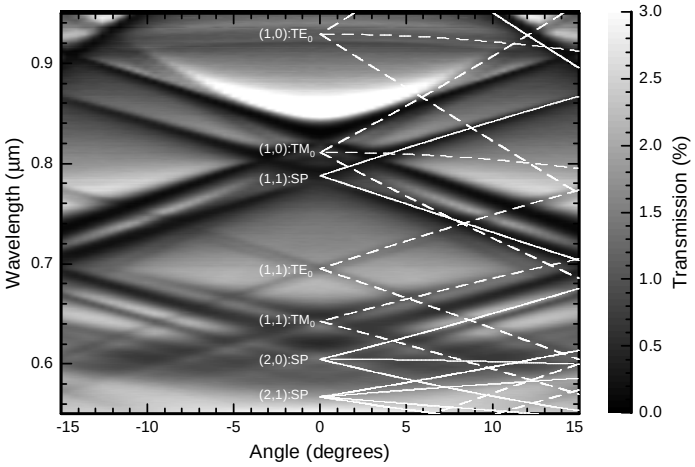

Figure 6.2. Grayscale plot of the measured transmission of a metal hole array covered with a dielectric layer as function of angle of incidence. The lines in the figure correspond to the calculated position of the different resonances. Each of the resonances corresponds to a specific reciprocal lattice vector and has an additional label to indicate the nature of the mode; i.e. surface plasmon (SP), fundamental TE waveguide mode (TE_0) or fundamental TM waveguide mode (TM_0).

interface is positioned at $x = 0$. The H-field of the m-th order TM mode that propagates in the positive z-direction can be written as

$$\vec{H}_m(\vec{r}, t) = \vec{H}_m(x)\, \mathrm{e}^{i(\omega t - \beta_m z)}, \tag{6.2}$$

where β_m is a propagation constant, that can be interpreted as the component of the wavevector parallel to the interface. For modes that are guided, the H field is confined either to the metal-to-dielectric interface (surface plasmon) or to the dielectric layer. Outside the region of the dielectric layer, the field $\vec{H}_m(x)$ decays exponentially. The H-field points in the y-direction (i.e., parallel to the interface), and it is given by

$$H_m(x) = \begin{cases} \frac{\epsilon_1 S_2}{\epsilon_2 S_1} \exp(-S_1 x) & 0 \leq x \\ \frac{\epsilon_1 S_2}{\epsilon_2 S_1} \cosh(S_2 x) - \sinh(S_2 x) & -d \leq x \leq 0 \\ \left[\frac{\epsilon_1 S_2}{\epsilon_2 S_1} \cosh(S_2 d) + \sinh(S_2 d)\right] \times & \\ \qquad \exp[S_3(x+d)] & x \leq -d \end{cases} \tag{6.3}$$

where the transverse momentum in the layer with dielectric constant ϵ_i is given by $S_i = \sqrt{\beta_m^2 - (\omega^2/c^2)\epsilon_i}$. A mode of this form can only exist when

the boundary conditions from Maxwell's equations are fulfilled at $x = 0$ and $x = d$, leading to the condition

$$\tanh(S_2 d) = -\frac{S_2}{\epsilon_2}\left(\frac{S_1}{\epsilon_1} + \frac{S_3}{\epsilon_3}\right) \Big/ \left(\left(\frac{S_2}{\epsilon_2}\right)^2 + \frac{S_1}{\epsilon_1}\frac{S_3}{\epsilon_3}\right). \tag{6.4}$$

This last equation can be used to numerically find the propagation constant β_m as function of frequency for all TM modes, including the surface plasmon mode. A similar approach can be applied to find all TE waveguide modes.

The curves in Fig. 6.2 are the numerically calculated resonance conditions for the surface plasmon on the sol-gel side (solid curves) and the waveguide modes in the structure (dashed curves). The calculated resonances due the surface plasmon on the substrate side are slightly red shifted and have been omitted from the figure for reasons of clarity. Each of the calculated resonances in the figure is labeled by a combination of reciprocal lattice vector and an identifier to indicate the nature of the mode. The modes are classified as a surface plasmon (SP), a fundamental TE waveguide mode (TE_0) or a fundamental TM waveguide mode (TM_0). In our calculation, we adjusted the thickness d of the sol-gel layer to get good agreement with the measured data and find a value of 480±10 nm. For this layer thickness, the cut-off frequencies of the higher order TE and TM waveguide modes are beyond the frequency range probed in the experiment.

6.3 Effects of layer thickness

The formalism discussed in the previous section can be used to design structures where the surface-plasmon resonances on both sides of the structures are index matched, by using a dielectric layer. A numerical algorithm is used to find the propagation constant β of the surface plasmon at a given wavelength as function the layer thickness d of the dielectric layer. This calculation is done for the surface plasmon modes on the "air" ($n = 1.0$) side of the structure as well as on the substrate ($n = 1.52$) side of the structure. In both cases, the dielectric layer has a refractive index of 1.4. This calculation allows to find the minimum required thickness of the dielectric layer, on each side, that is needed to create a structure in which the surface plasmon modes on the two interfaces are indistinguishable.

Figure 6.3 shows the real part of the calculated effective index, defined as $n_{\text{eff}} = \beta_m(\omega)c/\omega$, for gold covered with a dielectric film, as a function of the layer thickness d, for a wavelength of 800 nm (solid curve). The dotted curves show similar calculations for slightly different wavelengths of 700 nm

and 900 nm. We have included results for both sides of the metal film, with insets next to the curves to show the configuration that corresponds to the curves. For a thin dielectric layer inserted between the metal and air, the surface plasmon propagates mostly in the air and the effective index is close to that of a surface plasmon propagating on a bare air-to-gold interface. When the layer thickness is increased, the effective index approaches that of a surface plasmon on a single dielectric-to-metal interface. From the figure it is clear that this situation is reached for a layer thickness ~ 500 nm. As expected, the required thickness becomes smaller for shorter wavelengths.

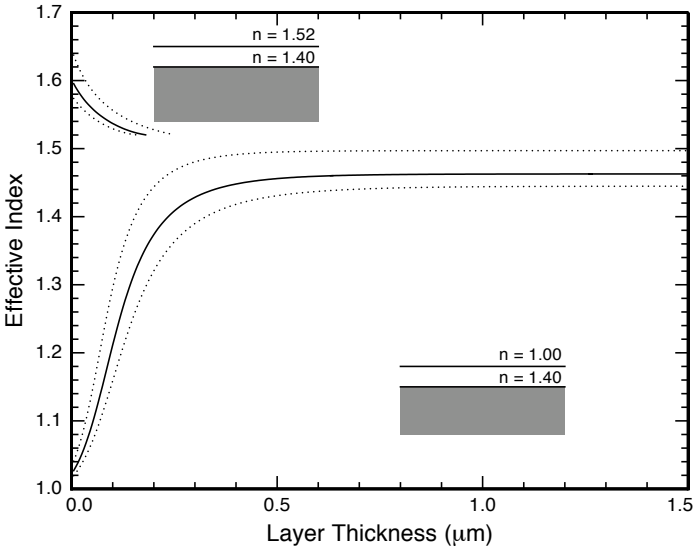

Figure 6.3. Effective index for a gold interface covered with a dielectric film, as a function of the thickness of the dielectric layer. The dielectric layer has a refractive index $n = 1.40$. Results are shown for an ambient with a lower refractive index ($n = 1.00$), and with a higher refractive index ($n = 1.52$). The solid curves are calculated for a wavelength of 800 nm. The dotted curves indicate the change when the wavelength is 700 nm and 900 nm.

The effective index for the configuration that corresponds to the substrate side of the metal film behaves differently. As shown in the figure, the curves start at an effective index of a surface plasmon on a glass-to-gold interface. As long as a very thin layer of dielectric is used, the effective index of the surface plasmon is always larger than that of the dielectric with the highest ϵ, for frequencies below the plasmon frequency [64]. If the layer thickness is increased this is no longer the case and bound modes cease to exist for thicknesses larger

than 200 nm. At this point, the effective index of the surface plasmon mode becomes equal to the refractive index of the substrate and the surface mode transforms into a leaky mode. However, for a sufficiently thick dielectric layer, the coupling to radiation modes will be weak and the mode resembles the plasmon mode of a single glass-to-gold interface with $n = 1.4$. Based on the calculation of the surface plasmon mode on the air side, we estimate that the typical thickness required for this regime is also around 500 nm for a wavelength of 800 nm.

In Fig. 6.4, we show a grayscale plot of the transmission of such a symmetric structure. This structure was fabricated on a sol-gel glass layer of thickness 1000 nm, and after the deposition of the gold layer, another thick sol-gel glass layer was deposited on top of the structure. Again, the waveguide modes that are supported by the thick glass layer on top are clearly visible. From a fit of the waveguide mode dispersion, discussed before, we determined the thickness of the top layer to be $\sim$ 2100 nm. Besides the waveguide modes, the surface plasmon resonances are also clearly visible, as the dark diagonal bands. The surface plasmon modes on either side of the hole array have become indistinguishable.

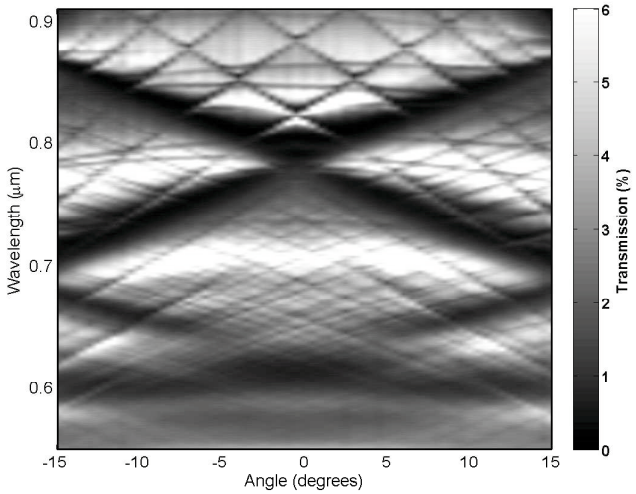

Figure 6.4. Gray scale plot of the measured transmission of a metal hole array covered with a $\sim$ 2100 nm thick dielectric layer, as a function of angle of incidence and wavelength. The surface-plasmon modes on either side of the hole array (broad dark bands) have become indistinguishable. The waveguide modes that are supported by the dielectric layer are clearly visible as sharp black lines.

6.4 Conclusion

In this chapter, we have shown that it is possible to make the resonances that correspond to surface plasmons that propagate on either side of a metal hole array indistinguishable. To achieve this, a sufficiently thick layer of glass needs to be deposited on top of the hole array. If the glass layer is too thin, the exponential tail of the surface plasmon will extend beyond the layer, which lowers the propagation constant of the surface plasmon. The transmission spectra of the metal hole arrays with a glass layer on top show a number of extra resonances, that are caused by resonant coupling to the waveguide modes that are sustained by this glass layer. Calculation of the dispersion of these modes gives perfect agreement with the measurements, and allowed us to determine the thickness of the glass layer. The surface-plasmon resonances in the (close to) index-matched structures change intensity and width. This change is further investigated in the next chapter.

Chapter 7

Observation of coupling between surface plasmons in index-matched hole arrays

We measured the transmission of a large array of holes in an optically thick gold film, immersed in liquids of different refractive index. For a large difference in refractive index between the substrate and the liquid ($\Delta n \gtrsim 0.05$), the transmission spectra contain separate resonances, due to coupling to surface plasmons propagating on each of the metal-to-dielectric interfaces. When the index difference is reduced, we observe an avoided crossing between a strong low-energy mode and a weak high-energy mode. The low-energy mode becomes broader and gains amplitude at the expense of the high-energy mode. For an index-matched array, a single broad resonance remains. These observations provide direct evidence that the two surface-plasmon modes on different sides of the interface are coupled.

This chapter is based on M. J. A. de Dood, E. F. C. Driessen, D. Stolwijk, and M. P. van Exter, *Observation of coupling between surface plasmons in index-matched hole arrays*, Phys. Rev. B **77**, 115437 (2008).

7.1 Introduction

It is well known that coupling of different surface plasmon modes on the same interface, via Bragg scattering, leads to the formation of bright and dark modes in 1-D arrays of slits or wires [54, 65, 66]. Alternatively, plasmons on a single interface can be coupled to a waveguide mode [67, 68]. The coupling between plasmons on different interfaces is more difficult to observe, because in most cases the plasmon resonances on different sides of the metal film are detuned in frequency. This is due to the inherent asymmetry of a metal film on a substrate. This asymmetry can be removed by either fabricating a symmetric sample or by using index matching liquids [69–71]. The observed transmission spectra generally resemble the calculated spectra [70, 72], but the finite size of the arrays and the numerical aperture of the incoming beam limit a proper observation of the coupling between the modes.

Here, we present transmission measurements on a large two-dimensional metal hole array, using a white light beam with a numerical aperture that is small enough to resolve the coupled modes. We obtain the frequency, the linewidth, and the amplitude of the resonances by fitting multiple Fano resonances to the transmission spectra [53, 54]. When the index difference between substrate and liquid is reduced we observe an avoided crossing between a broad low-energy mode and a narrow high-energy mode. At the same time, the linewidth and the amplitude of the low-energy mode increase at the expense of the high-energy mode. These modes correspond to the two peaks in the transmission spectrum, which can be identified as surface plasmons propagating on either the substrate or the liquid side of the metal film. Our observations can be described by a coupled-mode theory, and are consistent with calculations that use tunneling of light through the holes as the coupling mechanism [70, 72].

7.2 Experiments

For our experiments, we mounted a metal hole array on a glass substrate inside a closed glass cuvette with a 2.5 mm optical path length. The array was immersed in different refractive-index solutions. We used mixtures of ethanol and benzyl alcohol to cover the range n=1.36–1.54 and mixtures of benzyl alcohol and bromo-naphtalene for the range n=1.54–1.66. The refractive index of each mixture was determined by Abbe refractometry, and is close to the volume average of the refractive index of the two liquids. The glass substrate (Schott-BK7) has a nearly constant refractive index n=1.51 over the wavelength range of interest. The metal hole array is a large (1×1 mm^2) square

array of 200 nm diameter holes with a lattice constant $a = 700$ nm, in an optically thick (200 nm) gold film. A 2 nm thick Ti bonding layer ensures proper adhesion of the gold layer. The optical transmission was measured at normal incidence. We used a fiber-coupled lamp to illuminate a ~ 300 μm diameter spot on the sample, thus avoiding edge effects. The transmitted light was sent to a fiber-coupled grating spectrometer with a Si CCD array (resolution 1.2 nm, 550-1000 nm) or an InGaAs linear array (resolution 3.0 nm, 900-1700 nm). Apertures in the incident and transmitted light beam were used to limit the numerical aperture below 0.01.

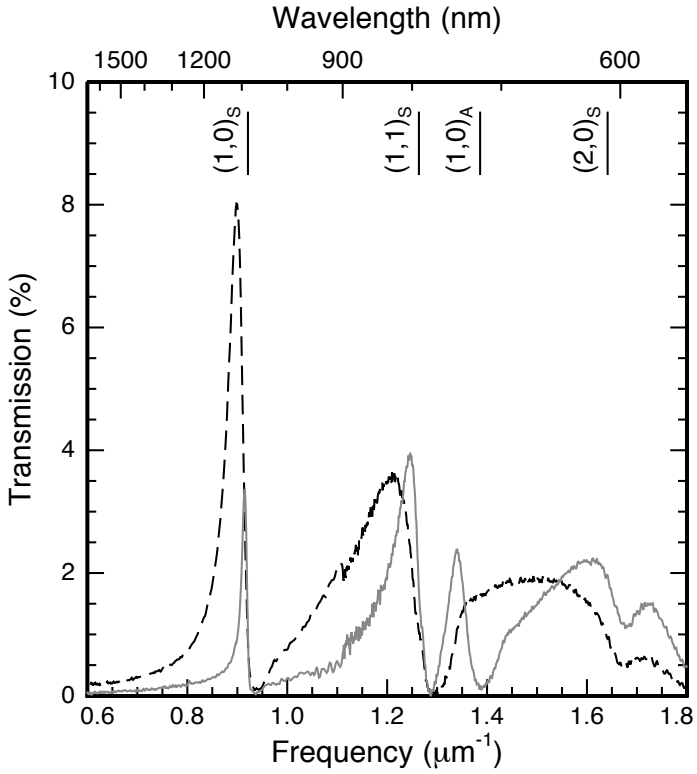

Figure 7.1. Transmission as function of frequency for a metal hole array in air (solid curve, $n_{\mathrm{L}} = 1.00$) and nearly index matched (dashed curve, $n_{\mathrm{L}} = 1.50$). The vertical lines indicate the calculated spectral positions of the different plasmon resonances on the substrate (S) and air (A) side of the array for $n_{\mathrm{L}} = 1.00$.

Figure 7.1 shows the measured transmission as function of frequency. Spectra are shown for the metal hole array in air (solid line), and immersed in a

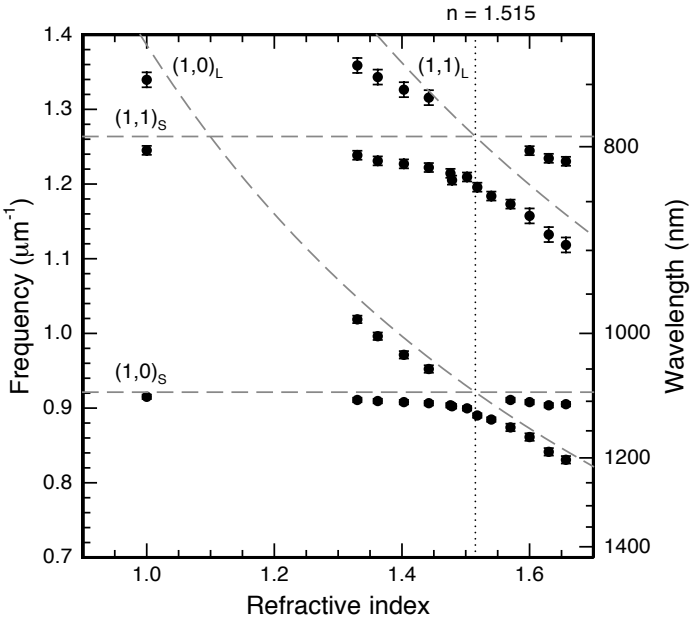

Figure 7.2. Frequencies of the maximum in transmission as a function of the refractive index obtained directly from the transmission data. The dashed curves show the calculated resonance frequencies according to Eq.(7.1).

liquid with refractive index $n_{\mathrm{L}} = 1.50$ (dashed curve). The spectra show a number of resonant peaks for which the transmission is enhanced. This is a result of coupling of incident radiation to surface plasmons that propagate on either the metal-to-air or the metal-to-substrate interface. The condition for coupling to such a surface plasmon is given by $\vec{k}_{\parallel} = \vec{k}_{\mathrm{SP}} + \vec{G}$, where $\vec{k}_{\parallel}$ is the component of the wave vector of the incident light along the interface, $\vec{k}_{\mathrm{SP}}$ is the wave vector of the surface plasmon and $\vec{G}$ is a reciprocal lattice vector. For normal incidence this condition leads to a set of resonance frequencies given by

$$\omega_{\mathrm{res}} = \frac{|\vec{G}|c}{n}\sqrt{1 + \frac{n^2}{\epsilon_{\mathrm{m}}(\omega)}}, \tag{7.1}$$

where c is the speed of light in vacuum, n is the refractive index of the dielectric, and $\epsilon_m(\omega)$ is the frequency-dependent dielectric constant of the metal. For a square lattice, the length of the reciprocal lattice vector is $|\vec{G}| = \sqrt{(N_{\mathrm{x}}^2 + N_{\mathrm{y}}^2)}2\pi/a$, with N_{x} and N_{y} integer. Therefore, the resonances

can be labelled as $(N_x, N_y)_{S,A}$, where the subscript indicates whether the resonance occurs on the substrate (S) or on the air (A) side of the metal hole array. To calculate the resonance frequencies we use literature values of the dielectric constant of gold [60] and take the dielectric constants of air and glass as constant. The vertical lines in Fig. 7.1 indicate the calculated positions of the different resonances. For an asymmetric structure with air on one side and glass on the other side, the resonances from the two sides are well separated.

When the air is replaced by a nearly index-matching liquid, the transmission spectrum changes drastically (dashed curve in Fig. 7.1). The $(1,0)_A$ mode on the metal-to-liquid interface shifts in frequency from 1.387 μm^{-1} (721 nm) to 0.922 μm^{-1} (1085 nm) to coincide with the $(1,0)_S$ mode on the metal-to-substrate interface. The peak transmission of the combined $(1,0)$ mode is roughly a factor of two higher, and a significant broadening of the resonance is observed.

The frequencies of the maxima in the transmission spectra are plotted in Fig. 7.2 as a function of the refractive index of the liquid (symbols). The dashed lines are the frequencies of the different modes as predicted by Eq. (7.1). The modes can be classified in two categories: modes on the metal-to-substrate interface (labelled 'S'), which do not shift when the index of the liquid is changed, and modes on the metal-to-liquid interface (labelled 'L'), which show a strong red-shift in frequency when the refractive index of the liquid is increased. To correctly predict the resonance frequencies from Eq. (7.1) the frequency dependent dielectric constant of the metal should be included. The index dispersion of the liquids and the glass can be neglected.

7.3 Model

The transmission through a metal hole array can be described as a combination of a non-resonant direct transmission through the holes, and a resonant component that couples to surface plasmons [53, 54, 72–74]. Interference between these two contributions gives an asymmetric line shape. The transmission spectra $T(\omega) = |t(\omega)|^2$ can be expressed as a sum over a finite number of (uncoupled) resonances

$$t(\omega) = a_{nr}\omega^2 + \sum_j \frac{b_j \Gamma_j \exp(i\varphi_j)}{(\omega - \omega_j) + i(\Gamma_j + \gamma_j)}, \tag{7.2}$$

where Γ_j is the radiative loss and γ_j is the intrinsic Ohmic loss of mode j. The resonance at frequency ω_j has an amplitude b_j and a phase φ_j. The slowly varying non-resonant contribution has an amplitude a_{nr} and is proportional

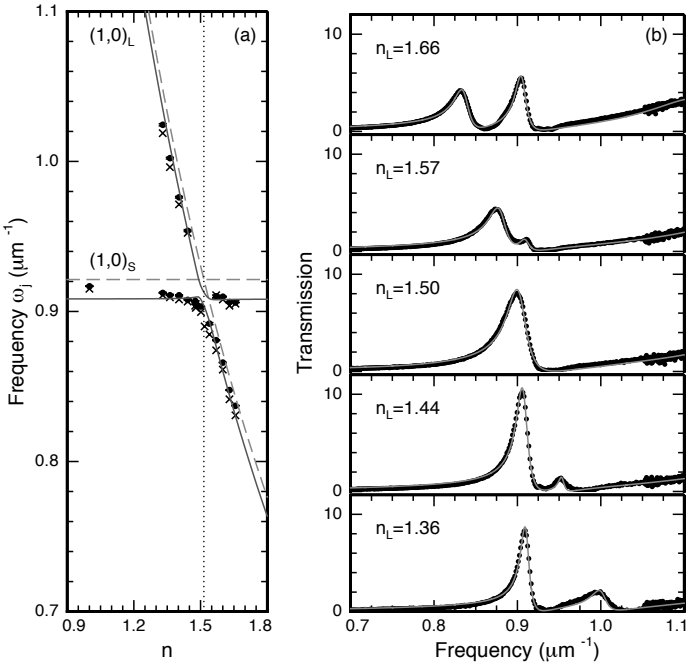

Figure 7.3. Detail of the crossing between the (1,0) modes (a) and corresponding spectra (b). The crosses are the peak frequencies obtained directly from the measured data, while closed symbols are the frequencies ω_j from fitting the transmission data to 4 Fano resonances. The solid curves are a fit to coupled-mode theory (see text). The dashed lines are the calculated frequencies for the uncoupled surface-plasmon resonances. The measured transmission (b) is shown for different refractive indices of the liquid (dots) and can be fitted to the Fano expression (curves)

to ω^2 to reflect the fact that the transmitted intensity through a single sub-wavelength hole is proportional to ω^4 for a single, sub-wavelength hole in a thin film of a perfect conductor [51]. In the limit of long wavelengths, the dielectric constant of the metal approaches that of the perfect conductor, while the film thickness relative to the wavelength becomes negligible and Eq. 7.2 gives the correct result. In principle, Eq. (7.2) allows a separation of resonant and non-resonant contributions, but in practice the number of separate resonances that can be identified in measured transmission spectra is limited. This complicates the interpretation of a_{nr} because the non-resonant term now also contains a contribution from resonances at higher frequencies.

Figure 7.3 shows the frequency of the peaks as a function of the refractive

index in more detail (a), and corresponding transmission measurements in the frequency range between 0.7 and 1.1 μm^{-1} (b). The solid curves are fits of Eq. (7.2), containing up to 4 resonant contributions. In these fits, the Ohmic losses γ_j were set to zero*. This description is valid for the typical situation that the radiative loss is much larger than the intrinsic Ohmic loss. The number of fit parameters can be reduced by setting all phases φ_j equal to π. This corresponds to the normal situation, where the resonant channel is out of phase with the direct channel. This choice does not affect the values of the other fit parameters significantly.

The crosses in Fig. 7.3(a) indicate the frequencies of the transmission maxima determined directly from the experimental data. These maxima are close to the resonance frequencies obtained from the fits (solid symbols). When the refractive index of the liquid is close to that of the substrate, the transmission spectrum is reduced to a single peak. Two distinct peaks can be observed for an index difference between liquid and substrate larger than $\sim$0.05. In addition, the linewidth and amplitude of the resonances depend strongly on the refractive index. The low-frequency resonance broadens and grows in amplitude when the refractive index is increased, while the high-frequency resonance narrows and diminishes in amplitude.

Figure 7.4 shows the linewidth Γ_j and square amplitude b_j^2 obtained from the fit of Eq. (7.2) to the transmission data. The triangular symbols refer to a fit where all parameters were kept free, while the circular symbols refer to a fit with all phases φ_j equal to π. The data in Fig. 7.4 confirm that the low-frequency mode (mode 1) gains amplitude and broadens while the high-frequency mode (mode 2) is reduced in amplitude and narrows. Note that a typical value of $\Gamma = 0.01\ \mu m^{-1}$ corresponds to a propagation distance $x = 1/(2\pi\Gamma) \approx 16\ \mu m$. This is much smaller than the illuminated spot size (300 μm) and the coherence length $D \approx \lambda/\mathrm{NA}$, which we estimate $> 100\ \mu m$ for a NA of less than 0.01. The avoided crossing together with the data in Fig. 7.4 prove that the two surface plasmons on different sides of the optically thick metal film are coupled.

A coupled-mode theory with only 2 modes is sufficient to describe our data. These modes correspond to the two surface plasmons that propagate on either the substrate or the liquid side of the metal film. In this analysis, we treat the plasmon modes on the same interface that are coupled via Bragg reflection [54, 65, 66] as a single mode. The time evolution of the amplitudes a

*The parameters b_j, Γ_j and γ_j are not independent and cannot be determined by a fit of the data to Eq. (7.2).

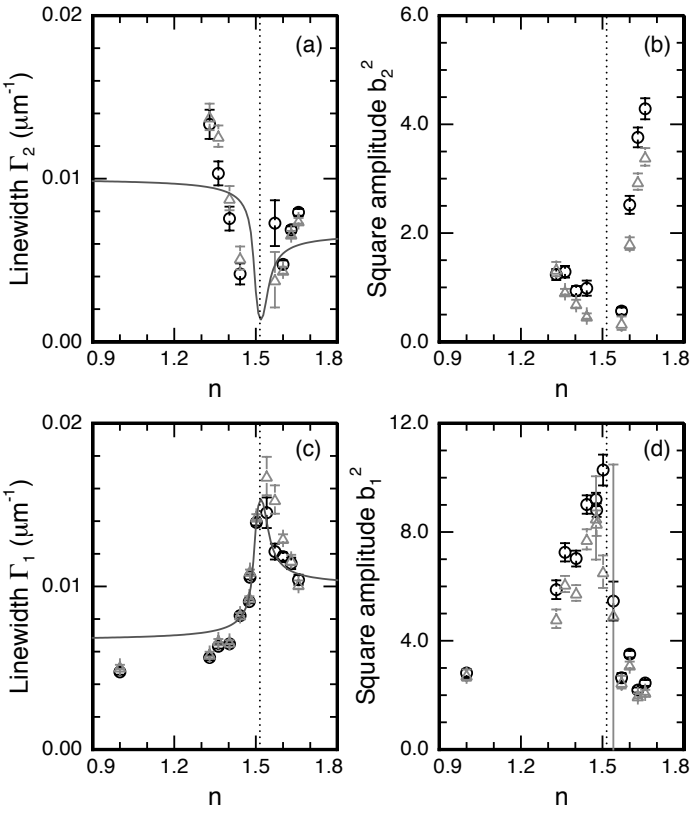

Figure 7.4. Linewidth Γ and square amplitude b^2 for the lowest two resonances as function of refractive index. The low-frequency mode (c,d) is always present and both linewidth and amplitude show a maximum around the index matched situation ($n_{\mathrm{L}} = 1.515$, dotted line). At the same time, the second mode shows a minimum in linewidth and amplitude and disappears from the spectra for nearly index-matched samples. The solid curve is a fit to coupled-mode theory (see text).

and b of the two modes in our model is given by the equation of motion

$$i\frac{\mathrm{d}}{\mathrm{d}t}\begin{pmatrix} a \\ b \end{pmatrix} = H\begin{pmatrix} a \\ b \end{pmatrix}. \tag{7.3}$$

The Hamiltonian H that describes the coupled system has the following form:

$$H = \begin{pmatrix} \omega_{\mathrm{a}} + V - i\Gamma_{\mathrm{a}} & W + i\Gamma_{\mathrm{C}} \\ W + i\Gamma_{\mathrm{C}} & \omega_{\mathrm{b}} + V - i\Gamma_{\mathrm{b}} \end{pmatrix}. \tag{7.4}$$

Table 7.1. Fit parameters of the coupled-mode theory described in the text

V	: Frequency shift	-0.013	$\pm$	$0.028\ \mu\mathrm{m}^{-1}$
Γ_a	: Damping rate of mode a	0.0067	$\pm$	$0.0004\ \mu\mathrm{m}^{-1}$
Γ_b	: Damping rate of mode b	0.0100	$\pm$	$0.0005\ \mu\mathrm{m}^{-1}$
W	: Conservative coupling rate	0.0046	$\pm$	$0.0015\ \mu\mathrm{m}^{-1}$
Γ_C	: Dissipative coupling rate	0.0068	$\pm$	$0.0011\ \mu\mathrm{m}^{-1}$

The diagonal elements of the matrix contain the frequencies $\omega_{\mathrm{a,b}}$ and linewidths $\Gamma_{\mathrm{a,b}}$ of the uncoupled modes, and a frequency shift V. The off-diagonal elements contain parameters W and Γ_C that describe conservative coupling (leading to mode splitting and an avoided crossing), and dissipative coupling (leading to mode pulling or frequency locking), respectively [75, 76]. The complex eigenvalues of the Hamiltonian H give the frequencies $\omega_{1,2}$ and linewidths $\Gamma_{1,2}$ of the coupled modes.

The solid curves in Figs. 7.3(a) and 7.4 are a fit of the model to the experimental data*. The fit parameters are summarized in Table 7.1. There is a small frequency red-shift V, compared to the resonance frequencies predicted by Eq. (7.1), which is consistent with the theory in Ref. [72]. The conservative coupling rate W causes the avoided crossing in Fig. 7.3(a). The frequencies ω_j can be fit satisfactorily by setting the dissipative coupling rate Γ_C to zero. However, a system with only conservative coupling gives line widths $\Gamma_{1,2}$ that are independent of refractive index. This is inconsistent with the data in Fig. 7.4. To describe the fact that the line width of one mode increases while the line width of the other mode decreases, a dissipative component in the coupling is needed. Conservative coupling is still important because a model with only dissipative coupling ($W = 0$) gives significant mode pulling, which is not observed in our measurements. As a comparison, Fig. 7.5 shows the fitted line widths for coupled mode theories with only conservative coupling (a), only dissipative coupling (b), and both conservative and dissipative coupling (c).

As a refinement of our model, we have also used damping rates $\Gamma_{\mathrm{a,b}}$ that depend on the refractive index of the liquid via the optical density of states [54, 77, 78]. Introducing these extra fit parameters indeed results in a better fit. However, it does not affect the values of the fit parameters V, W and Γ_C significantly, and thus does not change our interpretation of the measurements. The fit parameters in table 7.1 indicate that the mode on the liquid side is

*The fit was obtained by fitting the frequency and linewidth data simultaneously, giving equal weight to each of the points.

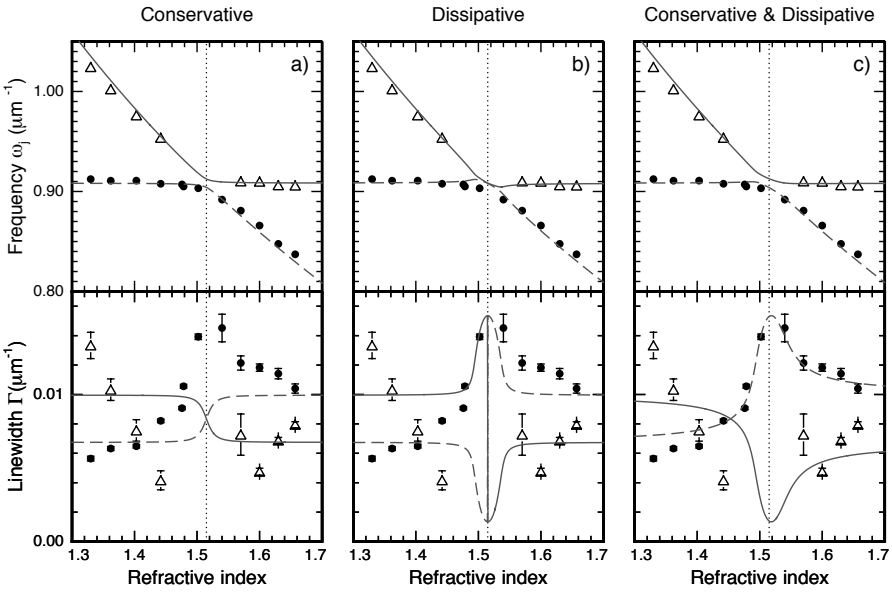

Figure 7.5. Frequencies and linewidths of the $(1, 0)$ resonance as function of the refractive index of the liquid. The values are obtained from a Fano fit of the measured transmission spectra at normal incidence and compared to coupled mode theory with only conservative coupling (a), only dissipative coupling (b) or both conservative and dissipative coupling (c). The closed symbols (data) and dashed curves (theory) indicate the low-energy mode, while the open triangles and solid curves indicate the high-energy mode.

somewhat more lossy than the mode on the glass side. It is reasonable to assume that this is due to the fact that the roughness of the metal-to-liquid interface is larger than the interface between the metal and the polished glass substrate. From AFM measurements on the sample, we indeed find roughness (rms) values of 4.4 nm for the gold surface, and 0.8 nm for the glass surface. In addition, some residual particles from the fabrication process are present on the gold-air interface, which will add to the scattering of surface plasmons on this interface.

The modes in our coupled-mode theory are consistent with the states calculated using a scattering formalism [70, 72]. On resonance, the eigenmodes correspond to a situation where the plasmons on the two interfaces oscillate in phase (low-frequency mode) or out of phase (high-frequency mode). Close to resonance, the calculated spectra show a split resonance (avoided crossing) and a linewidth of the low-energy mode that becomes larger, while the linewidth

of the high-energy mode becomes smaller. Without absorption the amplitude of the modes is equal. If absorption is included, the amplitude of the peaks is reduced depending on the linewidth (resonance time) of the mode [70]. This explains the dependence of the squared amplitude $b_{1,2}^2$ of the modes as function of refractive index given in Fig. 7.4.

7.4 Conclusion

In conclusion, an experiment where surface-plasmon resonances on either side of a metal hole array are tuned into degeneracy, gives insight into the coupling between these surface-plasmon modes. Two plasmon modes, on different sides of the metal film, can be identified if there is a large mismatch in refractive index. The resonance in the transmission spectra is reduced to a single broad resonance when the sample is index matched. This behavior can be explained by a coupling between the two surface plasmon modes through the hole-array. A coupled-mode analysis shows that the modes have an avoided crossing and correctly predicts the change in linewidth of the coupled modes when the refractive index is changed.

Part III

Superconducting single-photon detectors

Chapter 8

Polarization-dependent optical absorption of superconducting single-photon detectors

We measured the single-photon detection efficiency of NbN superconducting single photon detectors as a function of the polarization state of the incident light, for different wavelengths in the range from 488 nm to 1550 nm. The polarization contrast varies from ∼5% at 488 nm to ∼30% at 1550 nm, in good agreement with numerical calculations. We use an optical-impedance model to describe the absorption for polarization parallel to the wires of the detector. For lossy NbN films, the absorption can be kept constant by keeping the product of layer thickness and filling factor constant. As a consequence, we find that the maximum possible absorption is independent of filling factor. By illuminating the detector through the substrate, an absorption efficiency of ∼ 70% can be reached for a detector on Si or GaAs, without the need for an optical cavity.

This chapter is based on E. F. C. Driessen, F. R. Braakman, E. M. Reiger, S. N. Dorenbos, V. Zwiller, and M. J. A. de Dood, *Impedance model for the polarization-dependent optical absorption of superconducting single-photon detectors*, European Physical Journal - Applied Physics (2009).

8.1 Introduction

Superconducting single-photon detectors (SSPDs) [79], that consist of a meandering NbN wire, are an interesting new class of detectors that may outperform single-photon counting avalanche photodiodes. SSPDs feature a relatively high quantum efficiency at infrared wavelengths, combined with low time jitter, low dark counts, and high counting rates [80]. This makes these detectors promising for quantum optical studies and long-distance quantum cryptography applications [81].

A lot of attention has been given to the electronic operation of these detectors [82–84], leaving the optical design of the detectors less explored. In fact, due to the highly anisotropic nature of the wires, the detection efficiency shows a strong polarization dependence [85]. This is important, since a common way to encode quantum information is to use the polarization state of photons [86]. Detection of a photon thus comprises a simultaneous measurement of the polarization, which may be undesirable for some applications. At the same time, knowledge of the polarization dependence may simplify experimental schemes that require a polarization measurement, or can be used to optimize the detection efficiency.

The efficiency η to detect a single photon can be decomposed in an electronic and an optical contribution and can be expressed as

$$\eta = \eta_{\mathrm{e}} A, \tag{8.1}$$

where A is the optical absorption efficiency of the detector, and η_{e} is the electronic efficiency of the detector, i.e. the probability that an absorbed photon leads to a measurable voltage pulse across the detector.

The microscopic working principle of the detectors, which is essential to understand η_{e}, is still under active investigation [87, 88]. On a macroscopic level, a photon that is absorbed by the superconducting wire triggers a temporary loss of superconductivity, which gives rise to a finite voltage pulse across the detector. The optical absorption efficiency A is determined by the geometry of the detector and the dielectric constants of the substrate and the NbN layer. Since the energy of the incident photons is much larger than the superconducting gap of the NbN, the complex dielectric constant of the NbN layer at room temperature can be used.

The polarization dependence of NbN SSPDs has been investigated at a single wavelength and compared to finite-difference time domain calculations [85]. In section 8.4, we experimentally investigate the wavelength dependence of the polarization contrast, in the range between 488 and 1550 nm, and report a

strong dependence of the polarization contrast on the wavelength. We introduce an analytical optical-impedance model in section 8.5 to describe the optical absorption in thin lossy films and describe different ways to increase the detection efficiency by changing the parameters of the detector. We find that the optimum thickness is a strong function of the filling factor, while the maximum achievable absorption is independent of the NbN filling factor.

The optical impedance model also provides more insight into the cavity enhancement reported for a NbN detector inside a Fabry-Perot type cavity [85, 89]. We show, in section 8.5.3, that the absorption of the detector is enhanced by a factor n, with n the refractive index of the substrate, when the detector is illuminated from the substrate. This factor was not accounted for in earlier work and thus leads to an overestimate of the resonant enhancement. For a high index Si or GaAs substrate this factor becomes dominant and an absorption efficiencie of $\sim 70\%$ can be reached without the need for an optical cavity.

8.2 Experimental setup

The detectors in this experiment were two commercially available superconducting single-photon detectors (SSPD) [80]. These detectors nominally consist of a 4 nm thick and 100 nm wide NbN strip on an R-plane sapphire substrate, which is folded into a meandering structure of dimensions 10×10 μm^2 and filling factor 50%. Figure 8.1(a) shows a scanning electron microscope image of a detector similar to the ones used in our experiments.

SSPDs can be used to detect single photons when cooled below the critical temperature T_c of the NbN. When the detector is biased with a current close to the critical current, the absorption of a single photon deposits sufficient energy to locally bring the NbN material from the superconducting to the resistive state. The Ohmic heating due to this resistivity in turn switches a large part of the detector to the resistive state. The corresponding voltage pulse over the detector can be amplified and detected.

Figure 8.1(b) shows the electrical setup of the detectors. The dashed box shows an equivalent model circuit of the detector. It consists of a resistor of magnitude R_N in parallel with a switch. When the NbN wire is superconducting, the switch is closed. When a photon is absorbed, the switch shortly opens [83], leading to an increased impedance of the detector circuit. The inductor L_k is a model of the kinetic inductance of the superconducting wire.

Bias current I_b is provided to the detector by a voltage source V_b in series with a resistor $R_\text{b} = 400$ kΩ. Unless otherwise specified in this chapter, the

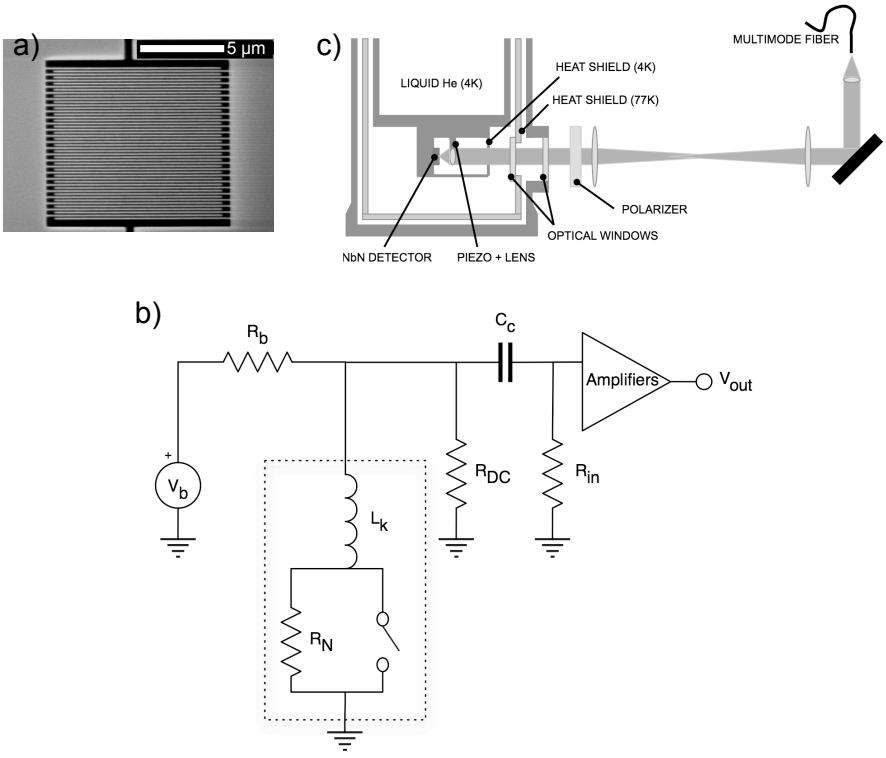

Figure 8.1. (a) SEM image of a NbN SSPD similar to the one used in the experiments. The 100 nm wide NbN line is folded into a meander with an area of 10×10 μm^2. (b) Schematic diagram of the readout electronics. The bias current is provided by a voltage source and a resistor of 400 kΩ. The dashed box contains a phenomenologically equivalent circuit of the detector. (c) Schematic overview of the optical setup. Wavelength-filtered light from a lamp is sent through an optical fiber with a 50 μm core, and is imaged onto the detector through a telescope and a moveable lens mounted inside the cryostat.

bias current was set such that $I_\mathrm{b} = 0.9 I_\mathrm{sw}$, where I_sw is the current at which the detector switches to the normal state. A coupling capacitor C_c transfers the high-frequency components of the voltage pulse over the detector to a 66 dB amplifier chain*, with an input resistance $R_\mathrm{in} = 50\,\Omega$. The resistor $R_\mathrm{DC} = 1\,\mathrm{k}\Omega$ ensures that when the detector is in the normal state, the current I_b does not flow through the detector, enabling it to cool down to the superconducting

*In our experiments we used a Miteq, JS2-01000200-10-10A (gain 36 dB), amplifier, followed by a MiniCircuits ZKL-2R5 (gain 30 dB) amplifier

state. The voltage pulse V_{out} was either measured with a 1.5 GHz oscilloscope, to retrieve the pulse shape, or sent to pulse counting electronics to obtain count rates.

We mounted the SSPD in a ^{4}He-cryostat and cooled it to a temperature of ∼5 K. The temperature remained constant within 10 mK during each measurement run. Unpolarized light from an incandescent tungsten lamp was wavelength-filtered and sent through a 50 μm core size multimode optical fiber. The output of the fiber was imaged onto the detector using 4 lenses, with the final lens mounted on a piezo stage inside the cryostat, as shown in Fig. 8.1(c). The outermost two lenses form a telescope that makes a 3× demagnified image of the fiber facet on the detector. The 1:1 telescope that is formed by the middle two lenses ensures that, with a small displacement of the optical fiber, the light entering the cryostat still impinges onto the last lens. To probe the polarization dependence of the detection efficiency, a linear polarizer with an extinction ratio better than 100 : 1 for the wavelength range of interest was placed in the parallel part of the beam. To probe the wavelength dependence, we used different narrow bandpass filters (≤10 nm FWHM) in combination with several edge filters to ensure that the light on the detector was monochromatic.

8.3 Characterization

Figure 8.2 shows the voltage pulse corresponding to a single detection event on the detector (dotted curve) together with an average over 100 pulses (solid curve). The initial steep rise corresponds to the detector switching to the normal state. The rise time is limited by both the 2 GHz bandwidth of the amplifier chain, and the 1.5 GHz bandwidth of the oscilloscope. After the detector switches back to the superconducting state, the voltage V_{amp} at the input of the detector is given by

$$V_{\text{amp}}(t) = R_{\text{in}} I_{\text{b}} \exp\left(-\frac{t}{\tau}\right), \tag{8.2}$$

where τ is the reset time of the detector. The pulse shape after the detector, $V_{\text{out}}(t)$ is modified by the finite bandwidth of the amplifier chain. It is given by the convolution of the impulse response function of the amplifier chain, $H(t)$ and the voltage at the input of the detector $V_{\text{amp}}(t)$. The dash-dotted curve in Fig. 8.2 gives the best fit for τ, using the measured impulse response function of the amplifier chain, given in the inset of Fig. 8.2. This fit yields a reset time $\tau = 8.5 \pm 1$ ns.

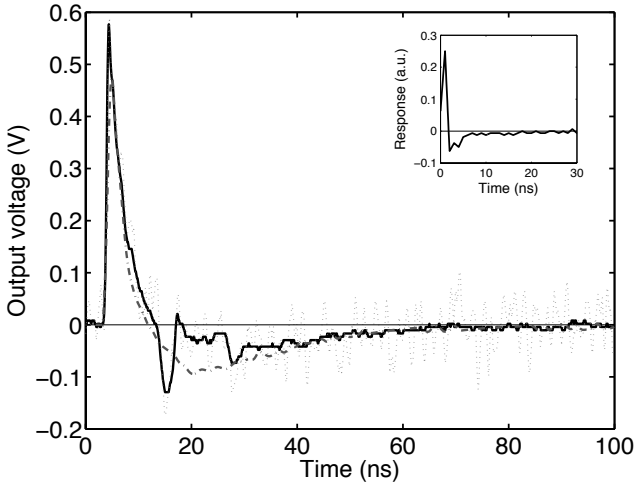

Figure 8.2. Detector pulse shape. The solid line is an average over 100 pulses. The dotted line is a single pulse, showing the noise level. The dash-dotted line is a fit to the measured pulse shape, of an exponential decay, convolved with the amplifier response shown in the inset.

The reset time of the detector should be compared to the time that is needed to restore the current through the superconducting wire, given by [83]

$$\tau = \frac{L_{\mathrm{k}}}{R_{\mathrm{in}}}. \tag{8.3}$$

From this, we determine the kinetic inductance of the detector to be $L_{\mathrm{k}} = 425 \pm 50$ nH, which corresponds well to the specific kinetic inductance of 0.87 nH/μm [90] for a 4 nm thick, 100 nm wide line of NbN.

In Fig. 8.3 we show the count rate of a detector as a function of the bias current I_{b}. When the bias current increases, less energy is needed to switch the superconductor to the normal state. This means that the probability that an absorbed photon leads to a voltage pulse increases [91]. The efficiency of the detector is ultimately limited by the optical absorption of the metal wire. The saturation of the count rate that corresponds to this limit [80] was not observed in our experiments, due to the relatively high temperature of the detectors. This indicates that $\eta_{\mathrm{e}} < 1$ in our measurements. The squares show the count rate when no light impinges onto the detector. The slope of this curve is comparable to the slope for an illuminated detector, indicating that the dark count rate in this case is dominated by detection of stray light, and not by the intrinsic dark count rate of the detector [92].

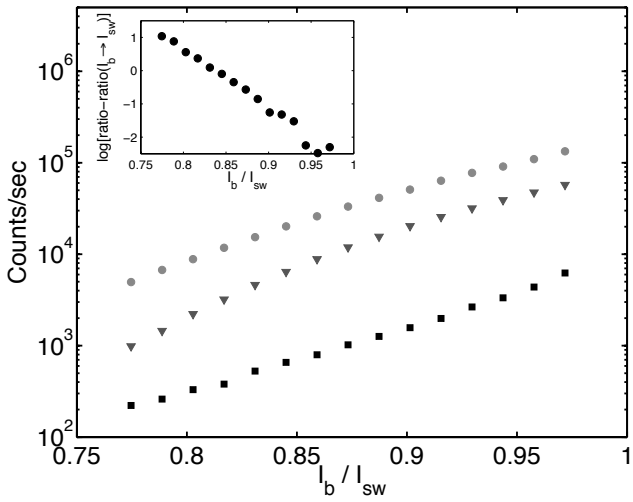

Figure 8.3. Detector count rate as a function of bias current, for light with a wavelength of 780 nm (circles) and 1550 nm (triangles). The squares show the count rate when no light impinges onto the detector. The inset shows the ratio between the count rate at 780 nm and the count rate at 1550 nm, subtracted by their ratio when $I_\mathrm{b} \to I_\mathrm{sw}$, on a logarithmic scale. Note that the absolute power impinging onto the detector was not calibrated, so that the curves at different wavelength cannot be compared directly.

The detection efficiency depends on the wavelength of the incident light as well. The circles and triangles show the count rates at a wavelength of 780 nm and 1550 nm, respectively. Although the power of the incident light was not calibrated in this experiment, it can be seen that the count rate for 1550 nm light increases more rapidly with bias current than that for 780 nm light. The ratio of these two count rates R_{780} and R_{1550}, is a single exponential

$$\frac{R_{780}}{R_{1550}} = \exp\left(-\alpha \frac{I_\mathrm{b}}{I_\mathrm{sw}}\right) + \left(\frac{R_{780}}{R_{1550}}\right)_{I_\mathrm{b}=I_\mathrm{sw}} . \tag{8.4}$$

In the limit $I_\mathrm{b} \to I_\mathrm{sw}$, the ratio between the two curves exponentially reaches a constant value, as shown in the inset of Fig. 8.3. This behavior is not fully understood yet, although it has already been shown that it can be used to operate such a detector as a spectrometer [93].

8.4 Polarization dependence

Figure 8.4 shows the count rate of the detector as a function of linear polarization for a wavelength of 1550 nm (squares) and 532 nm (triangles). Note that the absolute count rates at different wavelengths cannot be compared directly, due to a difference in incident power. The insets show the orientation of the E-field relative to the detector. The measured count rates follow a sinusoidal dependence as a function of polarization and are minimal when the E-field is perpendicular to the lines of the detector.

We define the polarization contrast C as

$$C = \frac{N_{\parallel} - N_{\perp}}{N_{\parallel} + N_{\perp}}, \tag{8.5}$$

where $N_{\parallel}$ and $N_{\perp}$ are the count rates of the detector when the light is polarized parallel and perpendicular to the wires, respectively. This definition of the contrast is a direct measure for the polarization effects, independent of the electronic quantum efficiency (η_{e}), and the incident power. We extract the contrast from the sinusoidal fits to the data (solid curves in Fig. 8.4). It varies with the wavelength of the incident light and is independent of the bias current and temperature of the detector in our experiment.

The circles in Fig. 8.4 show the count rate as a function of polarizer angle, at a wavelength of 1550 nm, when two wedge depolarizers under a relative angle of 45° were placed after the polarizer. These wedge depolarizers effectively depolarize the incident light by imposing a position-dependent rotation of the polarization. Indeed, the polarization contrast in this case is reduced to below 3%. The lower average count rate can be attributed to the extra four air-glass interfaces in the optical setup, leading to an increased reflection of the incident light, and can also be caused by a small displacement of the beam impinging onto the detector.

The polarization effect can be understood by comparing the periodic structure of the detector to that of a wire grid polarizer [94] that consists of a grid of parallel, highly conductive metal wires with a subwavelength spacing. For a perfect conductor the E-field should be perpendicular to the metal surface. As a consequence, only light with a polarization perpendicular to the wires is efficiently transmitted. A similar argument holds for lossy metals, albeit that in this case the field penetrates into the metal, leading to absorption. This absorption is largest when the E-field is parallel to the wires, since in this case the field penetrates more into the metal.

For the typical dimensions and spacing of the NbN wires, an effective medium approach that is accurate for both polarizations is difficult [95, 96].

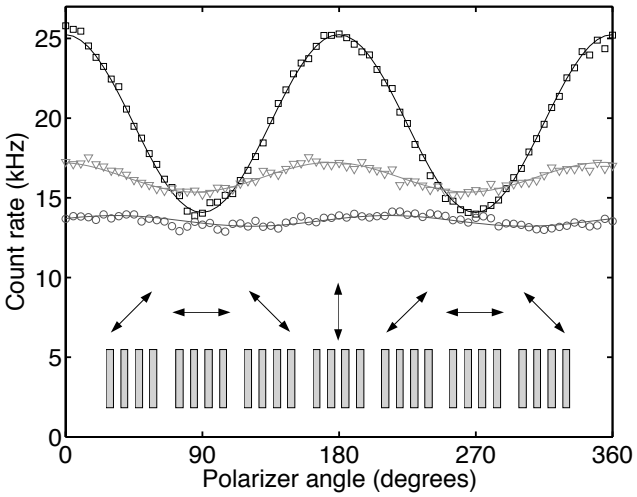

Figure 8.4. Count rate of the SSPD (corrected for stray light counts) as a function of linear polarization, for a wavelength of 1550 nm (squares) and 532 nm (triangles). The circles show the count rates for 1550 nm light when two wedge depolarizers (under a relative angle of 45°) are placed after the polarizer. The insets show the orientation of the E-field relative to the detector, for the different polarizer settings. The solid curves are sinusoidal fits to the data, used to extract the polarization contrast.

Instead, we calculated the absorption at normal incidence for an infinitely-sized detector, using the rigorous coupled-wave analysis (RCWA) developed in Ref. [37]. This method finds an exact solution of Maxwell's equations by expressing the electromagnetic fields in the different materials as a summation over all diffraction orders. The Fourier components of the periodic dielectric constant couple the diffraction orders in the patterned region. The continuity of the parallel component of the wavevector, together with the boundary conditions for the E and H fields fully determine the field in all regions. From this the intensity in all reflected and transmitted diffraction orders can be calculated. The absorption in the grating is then simply given by $A = 1 - R - T$, where R and T are the reflected and transmitted intensity.

The effects of focusing of the incident beam can be taken into account by decomposing the beam into plane waves with wave vector $\vec{k}$. Each of these plane waves will experience a different absorption $A(\vec{k})$. The effect of finite detector size can be incorporated in a similar way, by multiplying the beam profile in the near field by an aperture function $D(\vec{r})$ which is 1 at the location

of the detector, and 0 elsewhere. Taking both into account, the total absorption is given by the convolution integral

$$A = \int_{\vec{k}} A(\vec{k}) \left[u(\vec{k}) * D(\vec{k}) \right]^2 d\vec{k}, \tag{8.6}$$

where $u(\vec{k})$ is the Fourier transform of the beam profile, and $D(\vec{k})$ is the Fourier transform of the aperture function $D(\vec{r})$.

The k-spread of the incident waves is determined by the detector size [determining the spread in $D(\vec{k})$] and the numerical aperture of the last lens in the illuminating system, determining the spread in $u(\vec{k})$. The latter is the most important factor in our experiment, since we used a large-NA lens to focus the incoming light onto the detector. Calculations of the absorption of the grating as a function of angle of incidence (i.e., as a function of $\vec{k}$) show however, that the absorption only varies appreciably from the absorption at normal incidence for angles of incidence corresponding to NA > 0.5. Therefore, the total absorption given by Eq. (8.6) can be approximated by a product of the absorption coefficient at normal incidence and the total intensity impinging on the (finite-sized) detector. This justifies the use of a plane wave calculation in the rest of this chapter.

To calculate the absorption efficiency, we used the nominal structure parameters of the detector, and tabulated values of the dielectric constant of the sapphire substrate ($n_{\text{sapphire}} = 1.74$ at 1550 nm) [97]. For the wavelength-dependent dielectric constant of NbN, a Drude model [98] was used, giving a refractive index $n_{\text{NbN}} = 5.5 + 6.3i$ at a wavelength of 1550 nm. This value is close to the value reported in Ref. [85] ($n_{\text{NbN}} = 5.23 + 5.82i$), for a thicker NbN film.

Figure 8.5(a) shows the calculated absorption for polarization parallel (TE) and perpendicular (TM) to the wires, as a function of wavelength. The absorption for parallel-polarized light monotonously increases with wavelength, whereas the absorption for perpendicular polarization goes through a maximum and decreases for wavelengths above 800 nm. This leads to a higher polarization contrast for longer wavelengths.

For comparison, the dashed curve in Fig. 8.5(a) shows the absorption of an unpatterned film, multiplied by the filling factor of NbN, as was suggested in Ref. [79]. This estimate deviates over the entire wavelength range from the polarization-averaged result obtained by RCWA, which shows that for structures with features smaller than the wavelength of light, a more refined model is needed. We will discuss this refined model in Sec. 8.5. The fact that the absorption decreases for both the parallel polarization and for the closed

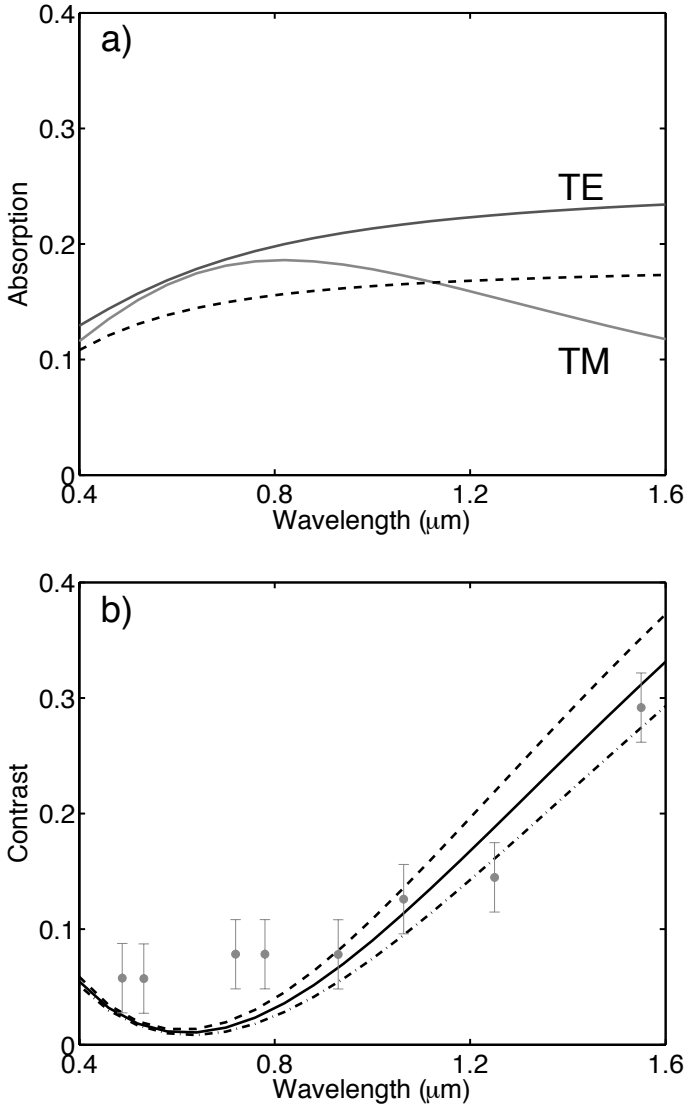

Figure 8.5. (a) Calculated absorption efficiency of a NbN grating as function of wavelength for polarization parallel (TE) and perpendicular (TM) to the lines of the detector. For comparison, the dashed line shows the calculated absorption of an unpatterned film multiplied by the filling factor of NbN. (b) Measured (dots) and calculated (black curves) polarization contrast as a function of wavelength. The calculations are shown for a filling factor of 52% (dashed), 55% (solid), and 58% (dash-dotted) and a film thickness of 4.5 nm.

film is mostly due to dispersion of the dielectric constant of the NbN material, ϵ_{NbN}.

In Fig. 8.5(b) we compare the measured polarization contrast (dots) to the results of the calculations (solid curve), as a function of wavelength. For comparison, the calculated contrast is shown for filling factors of 52% (dashed curve) and 58% (dash-dotted curve) as well. The experimentally observed contrast varies between ∼5% and ∼30% and increases with wavelength. The error bars on the experimental points represent slight variations in the measured polarization contrast during different measurement runs, as well as a slight polarization in the illuminating light source, of ∼ 1%. We attribute the fact that the calculation and the measurements differ for lower wavelengths to the fact that we used literature values for the dielectric constant of NbN. It is known that the dielectric constant of NbN varies as a function of the deposition parameters [98] and may depend on the film thickness as well [99]. Additional calculations (not shown) reveal, that for lower wavelengths, the polarization contrast is increasingly sensitive to small variations in the dielectric constant of NbN, since for these wavelengths, the Drude model for the dielectric constant of the NbN is close to resonance.

It has been shown that the linear-polarization dependence can be removed by changing the design of the detector [100]. A spiraling detector breaks the translational symmetry that causes the strong polarization contrast. The optical absorption in such a detector, however, will be lower than the maximum obtainable for parallel-polarized light, due to the fact that in these detectors, partial screening of the electric field is always possible.

8.5 Discussion

8.5.1 An optical impedance model for the absorption

In order to gain some physical insight into the absorption in the detector, we start out by describing the absorption of a film of thickness d with a complex dielectric constant ϵ_2, embedded between two dielectrics with refractive index n_1 and n_3, respectively. The film is illuminated from the medium with index n_1.

We can define the optical impedance of a medium i with refractive index n_i as

$$\eta_i = \frac{\eta_0}{n_i}, \tag{8.7}$$

where $\eta_0 = \sqrt{\mu_0/\epsilon_0} = 377\ \Omega$ is the impedance of the vacuum. The reflection

and transmission of the layered system are given by [101]

$$R = \left| \frac{\eta_{\text{load}} - \eta_1}{\eta_{\text{load}} + \eta_1} \right|^2, \tag{8.8}$$

$$T = \frac{\eta_1}{\eta_3} \left| \frac{2\eta_{\text{load}}}{\eta_{\text{load}} + \eta_1} \right|^2, \tag{8.9}$$

where η_{load} is the combined load impedance of the film and the backing substrate. The absorption of the film is again given by $A = 1 - R - T$.

If we assume that the film is thin enough to neglect interference effects ($k_0 d \ll 1$), the load impedance is given by [102]

$$\eta_{\text{load}} \approx \frac{R_\square \eta_3}{R_\square + \eta_3}, \tag{8.10}$$

where $R_\square \approx \eta_0 / k_0 d \text{ Im } \epsilon_2$ is the square resistance for a highly absorbing (Im $\epsilon_2 \gg$ Re ϵ_2) film, and k_0 is the wave vector of the light in vacuo. With these assumptions, we can write the absorption in the film as

$$A = \frac{4}{\eta_1 R_\square} \left(\frac{\eta_1 R_\square \eta_3}{\eta_1 + R_\square + \eta_3} \right)^2 = 4 n_1 \frac{k_0 d \text{ Im } \epsilon_2}{(n_1 + n_3 + k_0 d \text{ Im } \epsilon_2)^2}. \tag{8.11}$$

The absorption of the film reaches a maximum value $A_{\max} = n_1/(n_1 + n_3)$ for a square resistance given by

$$R_\square = \frac{\eta_1 \eta_3}{\eta_1 + \eta_3}. \tag{8.12}$$

Note that the maximum possible absorption is a function of the refractive indices of the surrounding media only. The optimal value of $R_\square$ to reach this maximum can be obtained by tuning the film thickness d.

8.5.2 The effect of film thickness

Figure 8.6 shows the absorption and the polarization contrast of a film of NbN, embedded between air ($n_1 = 1$) and sapphire ($n_3 = 1.74$), as a function of the film thickness. The solid curves show the calculated absorption using the rigorous coupled-wave analysis described before, while the dotted curves are obtained from the impedance model.

For a closed film, there is a distinct maximum of absorption, that occurs at a thickness

$$d = \frac{n_1 + n_3}{k_0 \text{ Im } \epsilon_2}. \tag{8.13}$$

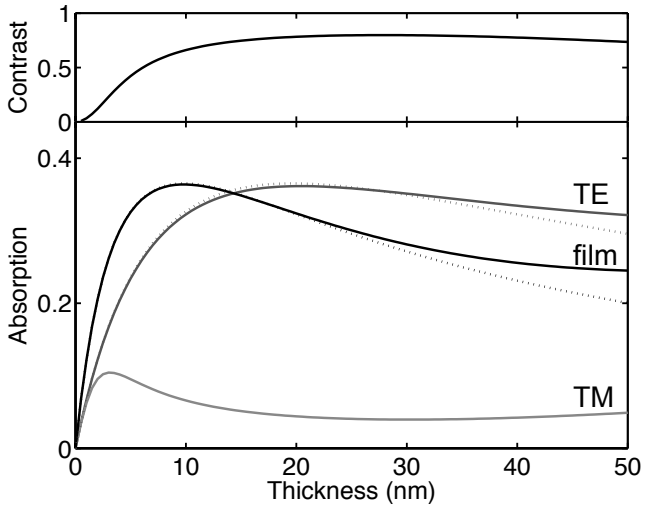

Figure 8.6. Calculated absorption at a wavelength of 1550 nm as a function of film thickness. The curve labeled "film" gives the absorption for a closed film, the other curves for a detector with lattice period 200 nm and filling factor 0.5, for polarization parallel (TE) and perpendicular (TM) to the wires of the detector. The dotted curves are calculated using the impedance model of section 8.5.1, whereas the solid curves are exact calculations using RCWA. The top graph shows the calculated polarization contrast.

For thinner films, the transmission through the film is too high to get maximal absorption, whereas for thicker films, reflection dominates.

The other curves in Fig. 8.6 show the absorption for a detector with filling factor 0.5 and lattice period 200 nm, for polarization parallel (TE) and perpendicular (TM) to the wires. The thickness for which the absorption in the patterned film is maximum, is higher than the optimal thickness for the closed film. The dotted curve is calculated using the impedance model of section 8.5.1, taking an effective dielectric constant for the absorbing film, given by [95]

$$\epsilon_{\text{eff}} = (1 - f)\epsilon_{\text{slits}} + f\epsilon_{\text{NbN}}, \tag{8.14}$$

where f is the filling factor of the metal, and ϵ_{slits} is the dielectric constant of the material in the slits, typically air. Since only the imaginary part of ϵ_{eff} determines the absorption in the film, the absorption of the detector can simply be calculated by multiplying the thickness of the film by the filling factor. For the polarization perpendicular to the wires of the detector, it is not so straightforward to define an effective dielectric constant for the patterned

film [95, 96]. For this polarization the light is concentrated in the air slits and the effective dielectric constant is closer to that of air. Therefore the condition Im $\epsilon_2 \gg$ Re ϵ_2 used to define the impedance model, breaks down for this polarization.

Surprisingly, the calculation also shows that it is easily possible to construct a detector where the absorption for parallel polarization is larger than the absorption of an unpatterned film of the same thickness. Since the electronic efficiency of the detector, η_e, strongly depends on the thickness of the metal [103, 104], it is important to realize that the absorption for parallel-polarized light is a function of df Im ϵ_2. A reduction in thickness of the detector, to increase the electronic efficiency, can thus be countered by increasing the filling factor accordingly.

8.5.3 Illuminating through sub- or superstrate

Commonly, NbN SSPDs are deposited on a substrate of sapphire and illuminated from air. An inspection of Eq. (8.11) shows that for a certain choice of sub- and superstrate, a factor of n_3/n_1 in absorption can be gained by illuminating the detector from the medium with the higher refractive index. Figure 8.7 shows the calculated absorption for a detector, with a superstrate of air ($n_1 = 1$), as a function of the refractive index of the substrate. The thickness of the detector is set such that maximal absorption in the detector is achieved. This thickness is indicated with the line. The solid curves give the absorption for illumination from the air, whereas the dash-dotted curves give the absorption for illumination from the substrate. The different curves are for polarization parallel (TE) and perpendicular (TM) to the wires. We stress that this effect is caused by a lower impedance mismatch and should be separated from the cavity enhancement of the absorption, previously reported in Refs. [85, 89].

When the substrate index is increased, the absorption rises for illumination from the substrate side. For illumination from the air side, the absorption for parallel polarization decreases. Note however that in both cases, the polarization contrast decreases, from $C = 0.88$ at $n_3 = 1$ to $C = 0.26$ at $n_3 = 4$, and is independent on the direction of illumination, as shown in the top graph of Fig. 8.7. The absorption is a factor of n_3 higher, when the detector is illuminated from the substrate, as expected from the impedance model. It is interesting to note that, for parallel-polarized light, the absorptions from super- and substrate add up to give $A_{\text{super}} + A_{\text{sub}} \approx 1$. It is therefore possible to construct a detector with higher absorption, up to 70%, and lower polarization contrast, by using a high refractive index substrate (e.g. Si or GaAs) and illuminating

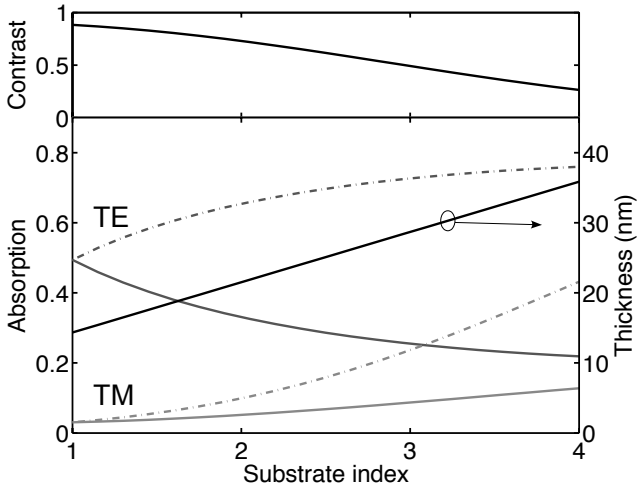

Figure 8.7. Calculated absorption for a detector with filling factor 0.5, lattice period 200 nm, at a wavelength of 1550 nm, as a function of the substrate refractive index. The solid curves are for illumination from the air side, the dash-dotted curves for illumination from the substrate side. The absorption is given for polarization parallel (TE) and perpendicular (TM) to the wires, respectively. The detector thickness is changed at each substrate index, to achieve maximal absorption. The thickness is given by the solid line (right axis). The top graph shows the polarization contrast.

the detector from the substrate. Unfortunately, increasing the refractive index of the substrate also increases the wavelength for which diffraction orders in the substrate appear. The first diffraction order at normal incidence appears at $\lambda/a = n_3$, with a the periodicity of the structure, and λ the wavelength of the light. In general, these diffraction orders lower the absorption efficiency. For a typical lattice period of 200 nm, and a substrate index of $n_3 = 3.5$, the first diffraction order appears at a wavelength of 700 nm, making detectors on a high-refractive-index substrate less effective for detecting visible light. The problem of diffraction could also be circumvented by designing a detector that has a variable line spacing.

8.6 Conclusion

In conclusion, we have measured a polarization dependence in the detection efficiency of NbN superconducting single photon detectors and find a wave-

length dependent polarization contrast between 5% and 30%. This effect can be explained by the geometry of the detector. Calculations of the optical absorption efficiency give good agreement with the measured data. We have demonstrated that the polarization dependence can be removed by the use of wedge depolarizers.

Furthermore, we have shown that the parameters of the detector can be tuned to achieve an absorption for a polarization parallel to the detector wires, that exceeds the absorption of an unpatterned film of the same thickness. We have given a simple optical impedance model, that allows for a quick estimate of the parameters needed to optimize the detector. For parallel-polarized light, the maximum absorption achievable is not determined by the thickness or the dielectric constant of the metal film, nor by the filling factor, but only by the refractive indices of the surrounding media. We have shown that by illuminating the detector from the substrate it is possible to increase the detection efficiency of the detector even further, by a factor equal to the refractive index of the substrate. Such highly absorbing, highly polarization-dependent detectors can be employed to efficiently detect photons with a well-defined polarization.

Chapter 9

The perfect absorber

We demonstrate that films of very lossy metal or dielectric, with a thickness of only a few nanometers, can absorb almost all incident radiation, when illuminated from the substrate side, at the critical angle for total internal reflection. The absorption for *s*-polarized light approaches 100%, while the absorption for *p*-polarized light vanishes. We demonstrate this effect by measuring the absorption as a function of the angle of incidence, at a wavelength of 775 nm in a 4.5 nm thick NbN film with a dielectric constant $\epsilon_{\mathrm{NbN}} = -8.2 + 31.4i$. The measured absorption in this film reaches a maximum of 94%. We discuss the design of a near-unity efficiency single-photon detector for *s*-polarized light, that has a broadband absorption coefficient of $> 90\%$ for wavelengths from 700 to 1600 nm.

This chapter is based on E. F. C. Driessen and M. J. A. de Dood, *The Perfect Absorber*, Applied Physics Letters **94**, 171109 (2009).

9.1 Introduction

An ideal photodetector or photovoltaic cell would absorb all incident radiation over a broad range of frequencies, and converts the energy into an electrical signal. Not only should the material absorb all radiation, it should also be thin enough to efficiently collect the electrical signal. Although very desirable, these requirements seem contradictory, and thin film materials that absorb all incoming light are extremely hard to find. A possible route around this problem is to use conventional materials and couple resonantly to a surface polariton [56, 105, 106], a waveguide mode [107], or a cavity that incorporates the absorbing material [85, 89]. Unfortunately, the resonant nature of these effects implies that the absorption can only be large over a narrow range of frequencies.

More recently, transition edge sensors [108] and high speed superconducting single-photon detectors (SSPDs) [79] have been described that use thin layers of extremely lossy materials, i.e. materials with a very large complex part of the dielectric constant. For these devices, the absorption is limited due to a large impedance mismatch at the interface, and the absorption at normal incidence is limited to 50% when the film is illuminated from the air side [79,85]. Illumination from the substrate side decreases the impedance mismatch and increases the optical absorption in the film by a factor n_{s}, where n_{s} is the refractive index of the substrate [109].

In this chapter, we show that it is possible to reach almost 100% absorption in a lossy film of only a few nanometers thick if the film is illuminated by *s*-polarized light at the critical angle for total internal reflection. We show measurements on the polarization-dependent absorption of an unstructured 4.5 nm thick NbN film on a sapphire substrate, and find that the absorption is well above 90%. The same concept can be applied to a detector structure that consists of a subwavelength meandering NbN wire. Calculations show that the absorption reaches a maximum of 94% when the detector is illuminated at the critical angle, and is $> 90\%$ over a wide frequency range.

9.2 Absorption of a closed film

In order to measure the absorption of a thin, lossy film at the critical angle, we used a 4.5 nm thick NbN film deposited on a double-polished R-plane sapphire substrate ($n_{\mathrm{s}} = 1.75$). The substrate was placed on an isosceles BK7 prism ($n = 1.51$) with index matching liquid between the substrate and the prism. This allows us to illuminate the film at angles larger than the critical angle for

total internal reflection [110].

Figure 9.1 shows the measured absorption of a 4.5 nm thick NbN film, at a wavelength of 775 nm, as a function of the angle of incidence, for light polarized parallel to the interface (s-polarized, closed symbols) and light with an electric field component perpendicular to the interface (p-polarized, open symbols). The film was illuminated using a 775 nm continuous-wave diode laser that was collimated to a $\sim$ 1 mm diameter beam. The polarization and orientation of the birefringent substrate were set to ensure that the linear polarization of the incident radiation was unchanged. The transmitted (T) and reflected (R) fraction of the incident power were recorded as a function of angle of incidence using a silicon photodiode, and were corrected for the losses due to reflections at the prism-air interfaces. From this the absorption is obtained as $A = 1 - R - T$.

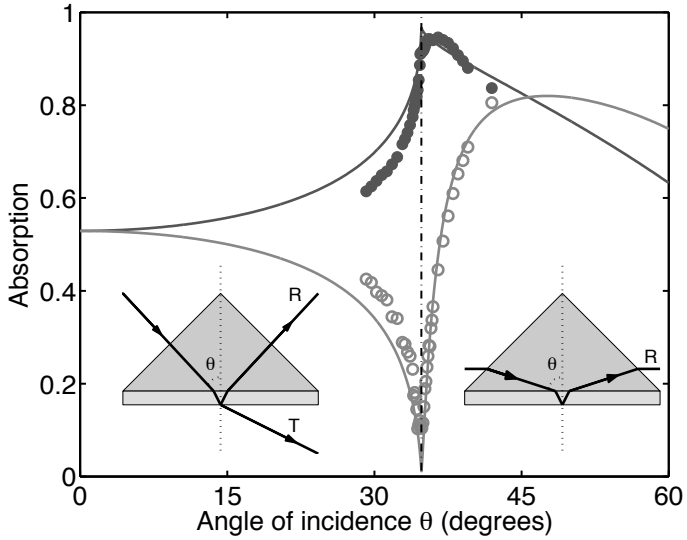

Figure 9.1. Measured optical absorption of a 4.5 nm thick NbN film as a function of angle of incidence, for s- (closed symbols) and p- (open symbols) polarized light. The curves are a fit of Fresnel's equations, using the (complex) refractive index of the NbN as only fit parameter. The dash-dotted line indicates the critical angle for total internal reflection. The insets show the experimental configuration of the prism and the substrate.

The dash-dotted line in Fig. 9.1 indicates the critical angle $\theta_c = \arcsin(n_s^{-1})$ for the substrate. For angles larger than this angle, light is not allowed to propagate in the air, and all incident light is either reflected or absorbed. At

the critical angle, the absorption for s-polarized light goes to a maximum value of $\sim 94\%$, for a film that is only 4.5 nm thick. At the same angle, the absorption for p-polarized light goes to a minimum of $\sim 10\%$.

At the critical angle θ_c, the amplitude of the evanescent wave extending into the air is zero. Hence, all the fields are contained in the half space bounded by the metal-air interface. For p-polarized light, the reflected and incident wave are out of phase, which creates an antinode in the thin film, expelling the field from the absorbing medium. For s-polarized light, the reflected and incident waves are in phase, creating a node at the boundary. A large part of the field is thus contained in the absorbing film, and absorbed.

We stress that the high absorption is not caused by coupling to a surface plasmon resonance or another polaritonic excitation on the metal-air interface. Such resonances only occur for p-polarized light (open symbols), at angles beyond the critical angle [105]. In fact, the local maximum for p-polarized light at an angle of incidence $\theta \approx 55^\circ$ is a remnant of the surface plasmon. Since we are dealing with a very thin, very lossy metal film, there is no sharp resonance. It is interesting to note that, at an angle $\theta \approx 46^\circ$, the absorption for both s- and p-polarized light can be as high as 80%.

We compare the measured absorption to the absorption calculated using Fresnel's coefficients for the reflection and transmission of a system with two interfaces [43]. The curves in Fig. 2.6 show a fit to the measurements where we used the complex dielectric constant of the absorbing NbN layer as the only fit parameter, giving $\epsilon_{\text{film}} = -8.2 + 31.4i$. We attribute the differences between the fit and the measurements to a small residual polarization rotation caused by the birefringence of the sapphire substrate.

The film thickness and the dielectric constant of the film determine the value of the absorption at the critical angle. For a film thickness much smaller than the wavelength, interference can be ignored. Furthermore, for a very lossy material, the real part of the dielectric constant of the film can be neglected. The absorption for s-polarization can then be approximated as [102]

$$A \approx 4 \frac{\sqrt{n_s^2 - 1}\, k_0 d \,\text{Im}\, \epsilon_{\text{film}}}{\left(\sqrt{n_s^2 - 1} + k_0 d \,\text{Im}\, \epsilon_{\text{film}}\right)^2}, \tag{9.1}$$

where k_0 is the wave vector of the light in vacuo, and d is the film thickness. The absorption reaches a maximum value at a film thickness given by

$$d = \frac{\sqrt{n_s^2 - 1}}{k_0 \,\text{Im}\, \epsilon_{\text{film}}}. \tag{9.2}$$

Note that the real part of the dielectric constant, and therefore also the sign of the real part, does not enter the expression for the maximum in absorption. This means that the maximum in absorption should occur both for lossy dielectrics and for lossy metals.

9.3 Nanostructured films

Some applications of thin absorbing films actually require a non-uniform film in order to work. In the remainder of this paper, we will show that it is equally possible to obtain the near-unity absorption for a superconducting single-photon detector [79], that consists of a meandering NbN wire. Absorption of a photon in this superconducting wire provides enough energy to give rise to a finite voltage pulse, which can be detected to count single photons. The parallel wire grid structure of the detector makes that light polarized parallel to the wires has a higher probability of being absorbed [85, 109].

Figure 9.2 shows the calculated absorption for a detector structure using the rigorous coupled-wave analysis developed in Ref. [37], as a function of angle of incidence, for light polarized parallel (TE) or perpendicular (TM) to the wires. The detector was oriented such, that the TE direction was parallel to the *s*-polarization of the incident light. This choice of orientation allows us to combine the high absorption due to the polarization dependence induced by the periodic grating structure, with the maximum in absorption due to the illumination at the critical angle. The detector has a line width of 100 nm and a filling factor of $f = 50\%$, and the thickness of the NbN lines was set to $d = 11.3$ nm to maximize the absorption. The value of the thickness was obtained from Eq. (9.2), taking an effective dielectric constant [95] for the patterned layer of $\epsilon_{\text{film}} = f + (1-f)\epsilon_{\text{NbN}}$, where ϵ_{NbN} is the dielectric constant of NbN.

At the critical angle, the calculated absorption reaches a maximum value of 94%, for *s*-polarized light. This confirms the fact, that the finite filling factor can be countered by increasing the film thickness [109]. It is important to notice that for an angular spread of $\sim 10^\circ$ around the critical angle, the absorption is still well above 80%, making the proposed detector also efficient for absorbing light with a finite numerical aperture.

In Fig. 9.3, we show the variation of the absorption of the detector geometry defined before, as a function of the film thickness, calculated using the rigorous coupled-wave analysis, for both polarizations. The graph shows that the absorption for *s*-polarized light reaches a maximum at $d = 10.8$ nm, close to the value predicted from Eq. (9.2). From this figure, we conclude that for

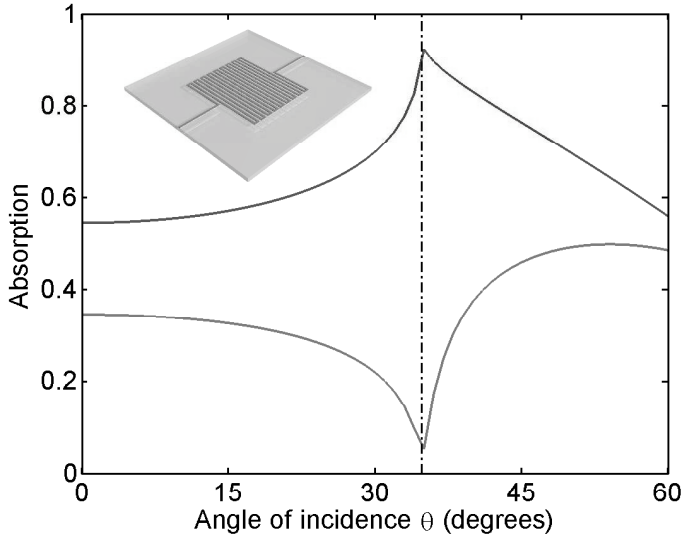

Figure 9.2. Calculated absorption as a function of the angle of incidence, for a detector geometry having a lattice period of 200 nm and a filling factor of 50% (as shown in the inset). The top curve gives the absorption for s-polarized light, the bottom curve for p-polarized light. The lines of the detector are positioned such that they are parallel to the p-polarization. The thickness of the detector layer $d = 11.3$ nm was set for optimal absorption. The dash-dotted line indicates the critical angle.

detectors with a thickness between 7 nm and 20 nm, the absorption is still $> 80\%$. This is much higher than the value obtained by other methods [89] and comparable to the optimum efficiency of silicon avalanche photodiodes. It also shows that the maximum in absorption is not very sensitive to the design of the detector. Decreasing the thickness might give rise to an increased electronic conversion efficiency for this kind of detectors [104]. This decrease in film thickness can be countered by an equal increase in filling factor f.

The inset of Fig. 9.3 shows the calculated wavelength dependence of the absorption. For this calculation, we used literature values for the dispersion of the sapphire substrate [97] and a Drude model for the dielectric constant of the NbN material [98]. We changed the high-frequency dielectric constant and the loss parameter to adjust the Drude model to the dielectric constant of the NbN film at 775 nm. The angle of incidence was set at the critical angle for a wavelength of 775 nm. The calculated absorption is almost constant.

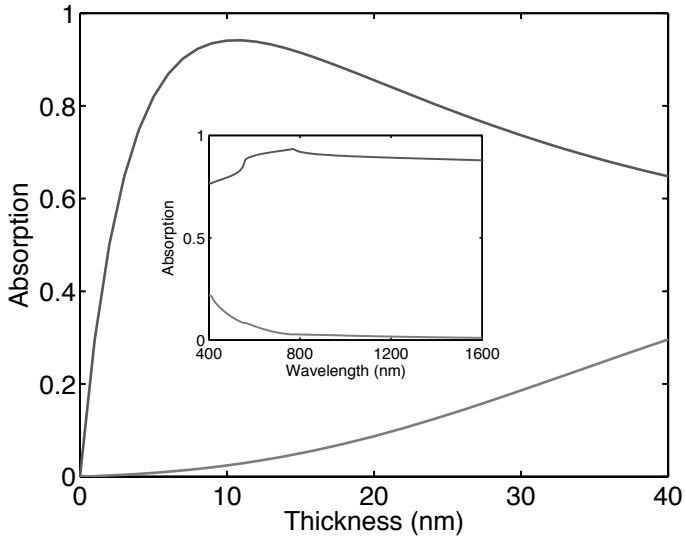

Figure 9.3. Calculated dependence of the absorption on the thickness of the NbN detector. For *s*-polarized light, the absorption has a maximum of 94.5% around 10.8 nm thickness. The inset shows the absorption as a function of the wavelength of the incident light. The wavelength dependence is small for *s*-polarized light.

This is due to the fact that the maximum absorption is only dependent on the product k_0 Im ϵ, which is nearly constant for a Drude metal far from resonance. As a result, the optimal film thickness only varies marginally with the wavelength of the incident light. The decrease in absorption at wavelengths < 550 nm is caused by the fact that for these wavelengths, diffraction from the periodic structure decreases the overall absorption. The dispersion of the sapphire substrate causes the small feature at 775 nm. At this wavelength, the angle of incidence is set exactly at the critical angle, and the absorption is maximal. For wavelengths below (above) this value, the angle is slightly below (above) the critical angle.

9.4 Conclusions

In conclusion, we have shown experimentally that the optical absorption of a 4.5 nm thick NbN can reach values as high as 94% for *s*-polarized light incident from the substrate side, at the critical angle for total internal reflection. For a very lossy material, the absorption of a thin layer does not depend on

the real part of the dielectric constant. The concept described here can therefore be applied to all devices that rely on the absorption of light in a thin, strongly absorbing film. To demonstrate this, we proposed a design for a superconducting single-photon detector that takes advantage of this effect, and calculated that this detector can reach an absorption efficiency as high as 94% for a filling factor of only 50%. The calculated absorption of the detector is shown to be almost wavelength-independent, and robust against changes in film thickness. At the critical angle, the light that is not absorbed is reflected and can be collected by a second detector. This way, a high-speed, near-100% single-photon detector comes into reach that might be competitive with existing silicon avalanche photodiodes in the visible. Since the effect is to a large extent wavelength independent, similar detector performance can be reached at telecommunication and infrared wavelengths were no fast single photon detectors with high ($> 50\%$) efficiency exist. To apply our method to photovoltaic cells or photodiodes requires a semiconductor material with $\mathrm{Im}\ \epsilon \ll \mathrm{Re}\ \epsilon$, which may be achieved by an appropriately designed metamaterial.

Appendix

Appendix A

Fabrication recipe for photonic-crystal slabs

In this appendix we summarize the fabrication process for the AlGaAs photonic-crystal slabs in this thesis.

A.1 Wafer preparation

Material:

SiN_x	150 nm	Etch mask
GaAs	100 nm	Protective capping layer
$Al_{0.35}Ga_{0.65}As$	150 nm	Photonic-crystal layer
$Al_{0.7}Ga_{0.3}As$	1000 nm	Sacrificial layer
GaAs	$\sim$200 μm	Wafer

Cleaning:

- Acetone, 50°, 5'
- Iso-propyl alcohol, rinse
- N_2 (g), dry

Resist application:

- Resist: ZEP 520A
- Spin coating, 1500 rpm, 60" (gives $\sim$ 500 nm thickness)
- Bake, 175°, 30'

A.2 Mask definition

Exposure:

- Positive-tone pattern
- Resolution: 10 nm
- Dose: 220-260 μC/cm^2
- Spot size: $\sim$ 8 nm

Development:

- *n*-amyl acetate, 80"
- 9:1 Methyl Isobutyl Ketone:Iso-propyl alcohol, 30"
- N_2 (g), dry

Transfer to silicon nitride:

- RIE etch
- 25 sccm CHF_3, 25 sccm Ar
- Power: 50 W
- Pressure: $\sim$ 8 μbar
- Etch speed: $\sim$ 15 nm/min
- Selectivity: $> 1:10$
- Stop monitored with interferometer

Resist removal:

- RIE etch
- 20 sccm O_2
- Power: 50 W
- Pressure: $\sim$ 4 μbar
- Etch speed: $>$ 100 nm/min

A.3 Pattern transfer

RIE etch:

- 15 sccm BCl_3, 7.5 sccm Cl_2, 10 sccm N_2
- Power: 100 W
- Pressure: $\sim$ 4 μbar
- Etch speed: $>$ 200 nm/min for GaAs, changes with Al concentration
- Selectivity: $>$ 10, changes with Al concentration

A.4 Mask removal

SiN_x removal:

- RIE etch
- 25 sccm CHF_3, 25 sccm Ar
- Power: 50 W
- Pressure: ~ 8 μbar
- Etch speed: ~ 15 nm/min
- Stop monitored with interferometer

GaAs capping layer removal:

- 4:1 Citric acid (50 wt%):H_2O_2 (40% solution), 1'
- H_2O, stop, 30"

A.5 Membrane formation

Sacrificial layer etch:

- 1:4 HF (40%):H_2O, 1'
- H_2O, stop, 30"
- iso-propyl alcohol, rinse
- dry with critical point dryer

Bibliography

[1] Aristophanes, *Clouds*, translated by Kenneth McLeish, Cambridge University Press, 423 B.C. (1979).

[2] S. John, *Strong localization of photons in certain disordered dielectric superlattices*, Phys. Rev. Lett. **58**, 2486 (1987).

[3] E. Yablonovitch, *Inhibited spontaneous emission in solid-state physics and electronics*, Phys. Rev. Lett. **58**, 2059 (1987).

[4] K. J. Vahala, *Optical microcavities*, Nature **424**, 839 (2003).

[5] C. Reese, B. Gayral, B. D. Gerardot, A. Imamoğlu, P. Petroff, and E. L. Hu, *High-Q photonic crystal microcavities fabricated in a thin GaAs membrane*, J. Vac. Sci. Technol. B **19**, 2749 (2001).

[6] S. M. Thon, M. T. Rakher, H. Kim, J. Gudat, W. T. M. Irvine, P. M. Petroff, and D. Bouwmeester, *Strong coupling through optical positioning of a quantum dot in a photonic crystal cavity*, Appl. Phys. Lett. **94**, 111115 (2009).

[7] A. Fiore, V. Berger, E. Rosencher, P. Bravetti, and J. Nagle, *Phase matching using an isotropic nonlinear optical material*, Nature **391**, 463 (1998).

[8] J. P. Mondia, H. M. van Driel, W. Jiang, A. R. Cowan, and J. F. Young, *Enhanced second-harmonic generation from planar photonic crystals*, Opt. Lett. **28**, 2500 (2003).

[9] M. J. A. de Dood, W. T. M. Irvine, and D. Bouwmeester, *Nonlinear photonic crystals as a source of entangled photons*, Phys. Rev. Lett. **93**, 040504 (2004).

[10] E. Verhagen, A. Polman, and L. Kuipers, *Nanofocusing in laterally tapered plasmonic waveguides*, Opt. Express **16**, 45 (2008).

[11] Z. Yu, G. Veronis, Z. Wang, and S. Fan, *One-way electromagnetic waveguide formed at the interface between a plasmonic metal under a static*

magnetic field and a photonic crystal, Phys. Rev. Lett. **100**, 023902 (2008).

[12] E. Laux, C. Genet, T. Skauli, and T. Ebbesen, *Plasmonic photon sorters for spectral and polarimetric imaging*, Nat. Photon. **2**, 161 (2008).

[13] F. Villa, L. E. Regalado, F. Ramos-Mendieta, J. Gaspar-Armenta, and T. Lopez-Rios, *Photonic crystal sensor based on surface waves for thin-film characterization*, Opt. Lett. **27**, 646 (2002).

[14] P. Yeh, *Optical Waves in Layered Media*, John Wiley & Sons, Hoboken, N.J., 1998.

[15] H. Raether, *Surface Plasmons on Smooth and Rough Surfaces and on Gratings*, Springer, 1988.

[16] T. F. Krauss and R. M. De la Rue, *Photonic crystals in the optical regime - past, present and future*, Prog. Quant. Electron. **23**, 51 (1999).

[17] H. Kosaka, T. Kawashima, A. Tomita, M. Notomi, T. Tamamura, T. Sato, and S. Kawakami, *Photonic crystals for micro lightwave circuits using wavelength-dependent angular beam steering*, Appl. Phys. Lett. **74**, 1370 (1999).

[18] T. Yoshie, A. Scherer, J. Hendrickson, G. Khitrova, H. M. Gibbs, G. Rupper, C. Ell, O. B. Shchekin, and D. G. Deppe, *Vacuum Rabi splitting with a single quantum dot in a photonic crystal nanocavity*, Nature **432**, 200 (2004).

[19] M. Kanskar, P. Paddon, V. Pacradouni, R. Morin, A. Busch, J. F. Young, S. R. Johnson, J. MacKenzie, and T. Tiedje, *Observation of leaky slab modes in an air-bridged semiconductor waveguide with a two-dimensional photonic lattice*, Appl. Phys. Lett. **70**, 1438 (1997).

[20] V. N. Astratov, D. M. Whittaker, I. S. Culshaw, R. M. Stevenson, M. S. Skolnick, T. F. Krauss, and R. M. De la Rue, *Photonic band-structure effects in the reflectivity of periodically patterned waveguides*, Phys. Rev. B **60**, R16255 (1999).

[21] L. Li, *New formulation of the Fourier modal method for crossed surface-relief gratings*, J. Opt. Soc. Am. A **14**, 2758 (1997).

[22] D. M. Whittaker and I. S. Culshaw, *Scattering-matrix treatment of patterned multilayer photonic structures*, Phys. Rev. B **60**, 2610 (1999).

[23] A. R. Cowan, P. Paddon, V. Pacradouni, and J. F. Young, *Resonant scattering and mode coupling in two-dimensional textured planar waveguides*, J. Opt. Soc. Am. A **18**, 1160 (2001).

[24] S. Fan and J. D. Joannopoulos, *Analysis of guided resonances in photonic crystal slabs*, Phys. Rev. B **65**, 235112 (2002).

[25] T. Ochiai and K. Sakoda, *Nearly free-photon approximation for two-dimensional photonic crystal slabs*, Phys. Rev. B **64**, 045108 (2001).

[26] T. Ochiai and K. Sakoda, *Dispersion relation and optical transmittance of a hexagonal photonic crystal slab*, Phys. Rev. B **63**, 125107 (2001).

[27] T. Maeda, J. W. Lee, R. J. Shul, J. Han, J. Hong, E. S. Lambers, S. J. Pearton, C. R. Abernathy, and W. S. Hobson, *Inductively coupled plasma etching of III-V semiconductors in BCl_3-based chemistries I. GaAs, GaN, GaP, GaSb and AlGaAs*, Appl. Surf. Sci. **143**, 174 (1999).

[28] J. H. Kim, D. H. Lim, and G. M. Yang, *Selective etching of AlGaAs/GaAs structures using the solutions of citric acid H_2O_2 and deionized H_2O buffered oxide etch*, J. Vac. Sci. Technol. B **16**, 558 (1998).

[29] U. Fano, *Effects of Configuration Interaction on Intensities and Phase Shifts*, Phys. Rev. **124**, 1866 (1961).

[30] S. Fan, W. Suh, and J. D. Joannopoulos, *Temporal coupled-mode theory for the Fano resonance in optical resonators*, J. Opt. Soc. Am. A **20**, 569 (2003).

[31] W. Suh, Z. Wang, and S. Fan, *Temporal coupled-mode theory and the presence of non-orthogonal modes in lossless multimode cavities*, IEEE J. Quantum Elect. **40**, 1511 (2004).

[32] D. Gerace and L. C. Andreani, *Gap maps and intrinsic diffraction losses in one-dimensional photonic crystal slabs*, Phys. Rev. E **69**, 056603 (2004).

[33] A. Farjadpour, D. Roundy, A. Rodriguez, M. Ibanescu, P. Bermel, J. D. Joannopoulos, S. G. Johnson, and G. W. Burr, *Improving accuracy by subpixel smoothing in the finite-difference time domain*, Opt. Lett. **31**, 2972 (2006).

[34] J. C. Maxwell Garnett, *Colours in Metal Glasses and in Metallic Films*, Philos. Trans. R. Soc. London Ser. A **203**, 385 (1904).

[35] J. C. Maxwell Garnett, *Colours in Metal Glasses, in Metallic Films, and in Metallic Solutions. II*, Philos. Trans. R. Soc. London Ser. A **205**, 237 (1906).

[36] W. L. Barnes, T. W. Preist, S. C. Kitson, and J. R. Sambles, *Physical origin of photonic energy gaps in the propagation of surface plasmons on gratings*, Phys. Rev. B **54**, 6227 (1996).

[37] M. G. Moharam, E. B. Grann, D. A. Pommet, and T. K. Gaylord, *Formulation for stable and efficient implementation of the rigorous coupled-wave analysis of binary gratings*, J. Opt. Soc. Am. A **12**, 1068 (1995).

[38] P. Paddon and J. F. Young, *Two-dimensional vector-coupled-mode theory for textured planar waveguides*, Phys. Rev. B **61**, 2090 (2000).

[39] E. D. Palik, *Handbook of Optical Constants of Solids*, volume I, Academic Press, Inc., 1985.

[40] E. Flück, *Local interaction of light with periodic photonic structures*, PhD thesis, University of Twente, 2003.

[41] E. F. C. Driessen, D. Stolwijk, and M. J. A. de Dood, *Asymmetry reversal in the reflection from a two-dimensional photonic crystal*, Opt. Lett. **32**, 3137 (2007).

[42] K. A. Tetz, L. Pang, and Y. Fainman, *High-resolution surface plasmon resonance sensor based on linewidth-optimized nanohole array transmittance*, Opt. Lett. **31**, 1528 (2006).

[43] M. Born and E. Wolf, *Principles of Optics*, Pergamon Press, 6th edition, 1980.

[44] L. C. Andreani and D. Gerace, *Photonic-crystal slabs with a triangular lattice of triangular holes investigated using a guided-mode expansion method*, Phys. Rev. B **73**, 235114 (2006).

[45] D. S. Gao and Z. P. Zhou, *Nonlinear equation method for band structure calculations of photonic crystal slabs*, Appl. Phys. Lett. **88**, 163105 (2006).

[46] M. Galli, M. Agio, L. C. Andreani, M. Belotti, G. Guizzetti, F. Marabelli, M. Patrini, P. Bettotti, L. Dal Negro, Z. Gaburro, L. Pavesi, A. Liu, and P. Bellutti, *Spectroscopy of photonic bands in macroporous silicon photonic crystals*, Phys. Rev. B **65**, 113111 (2002).

[47] E. Altewischer, X. Ma, M. P. van Exter, and J. P. Woerdman, *Resonant Bragg scatter of surface plasmons on nanohole arrays*, New J. Phys. **8**, 57 (2006).

[48] D. N. Chigrin, *Spatial distribution of the emission intensity in a photonic crystal: Self-interference of Bloch eigenwaves*, Phys. Rev. A **79**, 1 (2009).

[49] E. Altewischer, X. Ma, M. P. van Exter, and J. P. Woerdman, *Fano-type interference in the point-spread function. of nanohole arrays*, Opt. Lett. **30**, 2436 (2005).

[50] T. Ebbesen, H. J. Lezec, H. Ghaemi, T. Thio, and P. A. Wolff, *Extraordinary optical transmission through sub-wavelength hole arrays*, Nature **391**, 667 (1998).

[51] H. A. Bethe, *Theory of diffraction by small holes*, Phys. Rev. **66**, 163 (1944).

[52] H. F. Ghaemi, T. Thio, D. E. Grupp, T. Ebbesen, and H. J. Lezec, *Surface plasmons enhance optical transmission through subwavelength holes*, Phys. Rev. B **58**, 6779 (1998).

[53] U. Fano, *The theory of anomalous diffraction gratings and of quasi-stationary waves on metallic surfaces (Sommerfeld's waves)*, J. Opt. Soc. Am. **31**, 213 (1941).

[54] C. Ropers, D. J. Park, G. Stibenz, G. Steinmeyer, J. Kim, D. S. Kim, and C. Lienau, *Femtosecond light transmission and subradiant damping in plasmonic crystals*, Phys. Rev. Lett. **94**, 113901 (2005).

[55] C. Genet, M. P. van Exter, and J. P. Woerdman, *Huygens description of resonance phenomena in subwavelength hole arrays*, J. Opt. Soc. Am. A **22**, 998 (2005).

[56] R. Wood, *Anomalous Diffraction Gratings*, Phys. Rev. **48**, 928 (1935).

[57] E. Altewischer, M. P. van Exter, and J. P. Woerdman, *Polarization analysis of propagating surface plasmons in a subwavelength hole array*, J. Opt. Soc. Am. B **20**, 1927 (2003).

[58] W. L. Barnes, W. A. Murray, J. Dintinger, E. Devaux, and T. Ebbesen, *Surface plasmon polaritons and their role in the enhanced transmission of light through periodic arrays of subwavelength holes in a metal film*, Phys. Rev. Lett. **92**, 107401 (2004).

[59] K. L. van der Molen, K. J. Klein Koerkamp, S. Enoch, F. B. Segerink, N. F. van Hulst, and L. Kuipers, *Role of shape and localized resonances in extraordinary transmission through periodic arrays of subwavelength holes: Experiment and theory*, Phys. Rev. B **72**, 045421 (2005).

[60] P. B. Johnson and R. W. Christy, *Optical constants of the noble metals*, Phys. Rev. B **6**, 4370 (1972).

[61] S. C. Hohng, Y. C. Yoon, D. S. Kim, V. Malyarchuk, R. Muller, C. Lienau, J. W. Park, K. H. Yoo, J. Kim, H. Y. Ryu, and Q. H. Park, *Light emission from the shadows: Surface plasmon nano-optics at near and far fields*, Appl. Phys. Lett. **81**, 3239 (2002).

[62] A. Adams, J. Moreland, P. K. Hansma, and Z. Schlesinger, *Light emission from surface-plasmon and waveguide modes excited by N atoms near a silver grating*, Phys. Rev. B **25**, 3457 (1982).

[63] A. Yariv and P. Yeh, *Optical Waves in Crystals*, Wiley-Interscience, 2002.

[64] A. Karalis, E. Lidorikis, M. Ibanescu, J. D. Joannopoulos, and M. Soljacic, *Surface-plasmon-assisted guiding of broadband slow and subwavelength light in air*, Phys. Rev. Lett. **95**, 063901 (2005).

[65] Y. J. Chen, E. S. Koteles, R. J. Seymour, G. J. Sonek, and J. M. Ballantyne, *Surface plasmons on gratings: coupling in the minigap regions*, Solid State Commun. **46**, 95 (1983).

[66] H. Lochbihler, *Surface polaritons on gold-wire gratings*, Phys. Rev. B **50**, 4795 (1994).

[67] A. Christ, S. G. Tikhodeev, N. A. Gippius, J. Kuhl, and H. Giessen, *Waveguide-plasmon polaritons: Strong coupling of photonic and electronic resonances in a metallic photonic crystal slab*, Phys. Rev. Lett. **91**, 183901 (2003).

[68] T. Zentgraf, A. Christ, J. Kuhl, and H. Giessen, *Tailoring the ultrafast dephasing of quasiparticles in metallic photonic crystals*, Phys. Rev. Lett. **93**, 243901 (2004).

[69] A. Krishnan, T. Thio, T. J. Kima, H. J. Lezec, T. Ebbesen, P. A. Wolff, J. B. Pendry, L. Martín-Moreno, and F. J. García-Vidal, *Evanescently coupled resonance in surface plasmon enhanced transmission*, Opt. Commun. **200**, 1 (2001).

[70] L. Martín-Moreno, F. J. García-Vidal, H. J. Lezec, K. M. Pellerin, T. Thio, J. B. Pendry, and T. Ebbesen, *Theory of extraordinary optical transmission through subwavelength hole arrays*, Phys. Rev. Lett. **86**, 1114 (2001).

[71] L. Pang, K. A. Tetz, and Y. Fainman, *Observation of the splitting of degenerate surface plasmon polariton modes in a two-dimensional metallic nanohole array*, Appl. Phys. Lett. **90**, 111103 (2007).

[72] F. J. García de Abajo, *Colloquium: Light scattering by particle and hole arrays*, Rev. Mod. Phys. **79**, 1267 (2007).

[73] C. Genet, M. P. van Exter, and J. P. Woerdman, *Fano-type interpretation of red shifts and red tails in hole array transmission spectra*, Opt. Commun. **225**, 331 (2003).

[74] M. Sarrazin, J. P. Vigneron, and J. M. Vigoureux, *Role of Wood anomalies in optical properties of thin metallic films with a bidimensional array of subwavelength holes*, Phys. Rev. B **67**, 085415 (2003).

[75] R. J. C. Spreeuw, R. Centeno Neelen, N. J. van Druten, E. R. Eliel, and J. P. Woerdman, *Mode coupling in a He-Ne ring laser with backscattering*, Phys. Rev. A **42**, 4315 (1990).

[76] R. J. C. Spreeuw, N. J. van Druten, M. Beijersbergen, E. R. Eliel, and J. P. Woerdman, *Classical realization of a strongly driven two-level system*, Phys. Rev. Lett. **65**, 2642 (1990).

[77] S. G. Johnson, M. Ibanescu, M. A. Skorobogatiy, O. Weisberg, J. D. Joannopoulos, and Y. Fink, *Perturbation theory for Maxwell's equations with shifting material boundaries*, Phys. Rev. E **65**, 066611 (2002).

[78] D. S. Kim, S. C. Hohng, V. Malyarchuk, Y. C. Yoon, Y. H. Ahn, K. J. Yee, J. W. Park, J. Kim, Q. H. Park, and C. Lienau, *Microscopic origin of*

surface-plasmon radiation in plasmonic band-gap nanostructures, Phys. Rev. Lett. **91**, 143901 (2003).

[79] G. N. Gol'tsman, O. Okunev, G. Chulkova, A. Lipatov, A. Semenov, K. Smirnov, B. M. Voronov, A. Dzardanov, C. Williams, and R. R. Sobolewski, *Picosecond superconducting single-photon optical detector*, Appl. Phys. Lett. **79**, 705 (2001).

[80] G. N. Gol'tsman, O. Minaeva, A. Korneev, M. Tarkhov, I. Rubtsova, A. Divochiy, I. Milostnaya, G. Chulkova, N. Kaurova, B. M. Voronov, D. Pan, J. Kitaygorsky, A. S. Cross, A. J. Pearlman, I. Komissarov, W. Słysz, M. Węgrzecki, P. Grabiec, and R. R. Sobolewski, *Middle-infrared to visible-light ultrafast superconducting single-photon detectors*, IEEE Trans. Appl. Supercond. **17**, 246 (2007).

[81] H. Takesue, S. W. Nam, Q. Zhang, R. H. Hadfield, T. Honjo, K. Tamaki, and Y. Yamamoto, *Quantum key distribution over a 40-dB channel loss using superconducting single-photon detectors*, Nat. Photon. **1**, 343 (2007).

[82] A. Semenov, A. Engel, K. Il'in, G. N. Gol'tsman, M. Siegel, and H.-W. Hübers, *Ultimate performance of a superconducting quantum detector*, Eur. Phys. J.-Appl. Phys. **21**, 171 (2003).

[83] A. J. Kerman, E. A. Dauler, W. E. Keicher, J. K. W. Yang, K. K. Berggren, G. N. Gol'tsman, and B. M. Voronov, *Kinetic-inductance-limited reset time of superconducting nanowire photon counters*, Appl. Phys. Lett. **88**, 111116 (2006).

[84] M. Ejrnaes, R. Cristiano, O. Quaranta, S. Pagano, A. Gaggero, F. Mattioli, R. Leoni, B. Voronov, and G. N. Gol'tsman, *A cascade switching superconducting single photon detector*, Appl. Phys. Lett. **91**, 262509 (2007).

[85] V. Anant, A. J. Kerman, E. A. Dauler, J. K. W. Yang, K. M. Rosfjord, and K. K. Berggren, *Optical properties of superconducting nanowire single-photon detectors*, Opt. Express **16**, 10750 (2008).

[86] D. Bouwmeester, A. K. Ekert, and A. Zeilinger, *The Physics of Quantum Information*, Springer, 2000.

[87] A. Engel, A. Semenov, H.-W. Hübers, K. Il'in, and M. Siegel, *Fluctuation effects in superconducting nanostrips*, Physica C **444**, 12 (2006).

[88] M. Bell, N. Kaurova, A. Divochiy, G. N. Gol'tsman, J. Bird, A. Sergeev, and A. A. Verevkin, *On the nature of resistive transition in disordered superconducting nanowires*, IEEE Trans. Appl. Supercond. **17**, 267 (2007).

[89] K. M. Rosfjord, J. K. W. Yang, E. A. Dauler, A. J. Kerman, V. Anant, B. M. Voronov, G. N. Gol'tsman, and K. K. Berggren, *Nanowire Single-*

photon detector with an integrated optical cavity and anti- reflection coating, Opt. Express **14**, 527 (2006).

[90] S. N. Dorenbos, *Fabrication and characterization of superconducting detectors for single photon counting*, MSc Thesis, Delft University of Technology, 2007.

[91] A. A. Verevkin, J. Zhang, R. R. Sobolewski, A. Lipatov, O. Okunev, G. Chulkova, A. Korneev, K. Smirnov, G. N. Gol'tsman, and A. Semenov, *Detection efficiency of large-active-area NbN single-photon superconducting detectors in the ultraviolet to near-infrared range*, Appl. Phys. Lett. **80**, 4687 (2002).

[92] A. Korneev, Y. Vachtomin, O. Minaeva, A. Divochiy, K. Smirnov, O. Okunev, G. N. Gol'tsman, C. Zinoni, N. Chauvin, L. Balet, F. Marsili, D. Bitauld, B. Alloing, L. Li, A. Fiore, L. Lunghi, A. Gerardino, M. Halder, C. Jorel, and H. Zbinden, *Single-photon detection system for quantum optics applications*, IEEE J. Sel. Top. Quant. **13**, 944 (2007).

[93] E. Reiger, S. N. Dorenbos, V. Zwiller, A. Korneev, G. Chulkova, I. Milostnaya, O. Minaeva, G. N. Gol'tsman, J. Kitaygorsky, D. Pan, W. Słysz, A. Jukna, and R. R. Sobolewski, *Spectroscopy with nanostructured superconducting single photon detectors*, IEEE J. Sel. Top. Quant. **13**, 934 (2007).

[94] G. R. Bird and M. Parrish, *The wire grid as a near-infrared polarizer*, J. Opt. Soc. Am. **50**, 886 (1960).

[95] D. E. Aspnes, *Local-field effects and effective-medium theory: a microscopic perspective*, Am. J. Phys. **50**, 704 (1982).

[96] J. M. Pitarke and F. J. García-Vidal, *Effective electronic response of a system of metallic cylinders*, Phys. Rev. B **57**, 15261 (1998).

[97] E. D. Palik, *Handbook of Optical Constants of Solids*, volume III, Academic Press, 1998.

[98] K. Tanabe, H. Asano, Y. Katoh, and O. Michikami, *Ellipsometric and optical reflectivity studies of reactively sputtered NbN thin films*, J. Appl. Phys. **63**, 1733 (1988).

[99] W.-J. Lee, J.-E. Kim, H. Y. Park, S. Park, M.-S. Kim, J. T. Kim, and J. J. Ju, *Optical constants of evaporated gold films measured by surface plasmon resonance at telecommunication wavelengths*, J. Appl. Phys. **103**, 073713 (2008).

[100] S. N. Dorenbos, E. Reiger, N. Akopian, U. Perinetti, V. Zwiller, T. Zijlstra, and T. M. Klapwijk, *Superconducting single photon detectors with minimized polarization dependence*, Appl. Phys. Lett. **93**, 161102 (2008).

[101] S. Ramo and J. R. Whinnery, *Fields and Waves in Modern Radio*, John Wiley & Sons, 2^{nd} edition, 1953.

[102] K. E. Kornelsen, M. Dressel, J. E. Eldridge, M. J. Brett, and K. L. Westra, *Far-infrared optical absorption and reflectivity of a superconducting NbN film*, Phys. Rev. B **44**, 11882 (1991).

[103] A. A. Verevkin, A. J. Pearlman, W. Slysz, J. Zhang, M. Currie, A. Korneev, G. Chulkova, O. Okunev, P. Kouminov, K. Smirnov, B. M. Voronov, G. N. Gol'tsman, and R. R. Sobolewski, *Ultrafast superconducting single-photon detectors for near-infrared-wavelength quantum communications*, J. Mod. Optic. **51**, 1447 (2004).

[104] A. Jukna, J. Kitaygorsky, D. Pan, A. S. Cross, A. J. Pearlman, I. Komissarov, O. Okunev, K. Smirnov, A. Korneev, G. Chulkova, I. Milostnaya, B. M. Voronov, G. N. Gol'tsman, and R. R. Sobolewski, *Dynamics of hotspot formation in nanostructured superconducting stripes excited with single photons*, Acta Phys. Pol. A **113**, 955 (2008).

[105] F. Z. Yang, J. R. Sambles, and G. W. Bradberry, *Long-range surface modes supported by thin films*, Phys. Rev. B **44**, 5855 (1991).

[106] Z. Yu, G. Veronis, S. Fan, and M. L. Brongersma, *Design of midinfrared photodetectors enhanced by surface plasmons on grating structures*, Appl. Phys. Lett. **89**, 151116 (2006).

[107] S. Bandiera, D. Jacob, T. Muller, F. Marquier, M. Laroche, and J.-J. Greffet, *Enhanced absorption by nanostructured silicon*, Appl. Phys. Lett. **93**, 193103 (2008).

[108] A. J. Miller, S. W. Nam, J. M. Martinis, and A. V. Sergienko, *Demonstration of a low-noise near-infrared photon counter with multiphoton discrimination*, Appl. Phys. Lett. **83**, 791 (2003).

[109] E. F. Driessen, F. R. Braakman, E. M. Reiger, S. N. Dorenbos, V. Zwiller, and M. J. D. Dood, *Impedance model for the polarization-dependent optical absorption of superconducting single-photon detectors*, Eur. Phys. J.-Appl. Phys. **47**, 1 (2009).

[110] E. Kretschman and H. Raether, *Radiative decay of non-radiative surface plasmons excited by light*, Z. Naturforsch. A **23**, 2135 (1968).

Summary

Coupling light to periodic nanostructures

In this thesis, the interaction of light with a variety of periodic nanostructures is studied. These nanostructures consist of material that is patterned on a (sub)wavelength scale. The periodicity of the pattern can cause a more efficient coupling to a guided or bound mode in the nanostructure. Alternatively, the anisotropy of the individual periods of the structure can cause strong polarization dependence of the optical properties. The thesis consists of three parts, in which these effects are studied in different kinds of periodic nanostructures.

In the first part (Chapters 2–4), so-called photonic-crystal slabs are studied. These slabs, that support at least one guided mode, consist of a high refractive index dielectric material, perforated by an array of holes. In Chapter 2, the reflection spectra from such slabs are discussed. The spectra contain several asymmetric resonances, on top of a slowly-varying background. The line shape of the resonances is explained in terms of a Fano model. In this model, there are two contributions to the reflection spectrum: a direct contribution, in which light is reflected by Fresnel reflection from the layered structure, and a resonant contribution, caused by coupling to a leaky waveguide mode in the slab. These two contributions interfere, which leads to the asymmetric line shape of the resonance. To quantitatively describe measured reflection spectra, loss needs to be included in the model, by adding a loss channel. This gives a model with the loss rate, escape rate, and resonance frequency as adjustable parameters. To predict the resonance frequency, a waveguide model that uses an effective refractive index for the photonic-crystal slab, is introduced. Numerical calculations show that resonances disappear when the

refractive index of the substrate underneath the slab is increased. This is explained by the cut-off condition of higher-order waveguide modes, given by the waveguide model.

The asymmetry of the line shape is determined by the relative phase of the resonant and the direct contribution of the reflection. In Chapter 3, this phase is changed experimentally, by changing the angle of incidence. For p-polarized light, the measured line shape of the resonance changes, from red-tailed asymmetric, to symmetric, to blue-tailed asymmetric, when the angle of incidence is increased from 20° to 80°, across Brewster's angle. With the Fano model of Chapter 2, it is shown that this change of asymmetry originates from a change in sign of the direct reflection, at Brewster's angle.

In Chapter 4, a particular resonance is studied in more detail. A strongly focused beam of monochromatic light is used to illuminate a photonic-crystal slab, and the reflection is measured both in real space and in k-space. A polarization analysis of the k-space images reveals that the resonance is caused by coupling to the TM_0 waveguide mode of the slab. In the real-space images, the resonant and direct contributions to the reflection are spatially separated. Due to this separation, the decay length of the resonance can be determined. This decay length varies with wavelength, and measures up to 7 μm. Combined with the information obtained from the reflection spectrum at normal incidence, this gives an estimate of the group refractive index $n_g = 2.6$, and the phase index $n_{eff} = 1.5$ of the resonant waveguide mode.

The second part of the thesis (Chapters 5-7) discusses experiments with metal hole arrays. These arrays consist of an optically thick gold layer, perforated by a regular array of holes. In the transmission spectra of these structures, resonances are observed that are caused by coupling to surface-plasmon modes on either side of the gold layer. In Chapter 5 the effect of placing a dielectric pillar in each of the holes is studied. Angle-dependent measurements of the transmission spectrum are compared to measurements where these pillars are removed. The pillars enhance the transmission, as well as the interaction between different surface-plasmon modes. The enhanced interaction causes a frequency splitting of 6% for modes on the pillar side of the hole array.

In Chapter 6, the metal hole array is covered with a thin layer of glass. This glass layer diminishes the asymmetry of the structure, and causes the resonances that are caused by coupling to surface plasmons on either side of the structure to become degenerate, when the glass layer is sufficiently thick. Besides the surface-plasmon resonances, a number of sharp dips is observed in the transmission spectra. These dips are caused by coupling to waveguide modes that are contained in the glass layer on top of the hole array, and their

angular dispersion is reproduced in calculations of these modes.

The transition from an asymmetric to a symmetric structure, where the resonances caused by surface plasmons that propagate on either side of the metal layer are frequency-degenerate, is studied in Chapter 7. This is done by immersing the metal hole array in liquids of increasing refractive index. When the index contrast is reduced, an avoided crossing is observed between the surface-plasmon modes on the liquid and glass sides of the metal hole array. Moreover, the line width of one of the resonances increases at the expense of the other, such that there is only a single resonance left when the modes are index matched. A coupled-mode theory with both conservative and dissipative coupling gives a phenomenological description of these observations.

The last part of this thesis describes the absorption of light in a superconducting single-photon detector. This type of detector consists of a meander of very thin, absorbing metal, niobiumnitride. In Chapter 8, the polarization-dependent detection efficiency of such a detector is studied. The parallel-wire structure of the detector induces a strong polarization dependence, which is caused by a higher optical absorption for light that is polarized parallel to the metal wires. A theoretical study of the absorption properties of the meander as a function of film thickness shows that the absorption for parallel-polarized light can be as high as the absorption of a closed film, when the product of filling factor and film thickness is kept constant. By illuminating the detector from the substrate side, the calculated absorption is increased by a factor equal to the refractive index of the substrate.

The final Chapter 9 discusses the absorption of a thin film of NbN as a function of angle of incidence. The measured absorption for *s*-polarized light approaches 100% when the film is illuminated at the critical angle for total internal reflection. The absorption for *p*-polarized light at the same time vanishes. This effect is to design a superconducting single-photon detector which has a calculated broadband absorption coefficient of $> 90\%$ for wavelengths from 700 to 1600 nm, for *s*-polarization.

Samenvatting

Het koppelen van licht aan periodieke nanostructuren

In dit proefschrift wordt de interactie van licht met een aantal verschillende periodieke nanostructuren bestudeerd. Deze nanostructuren bestaan uit materiaal dat een patroon heeft op de schaal van, of kleiner dan, de golflengte van het licht. De periodiciteit van het patroon kan zorgen voor een efficiëntere koppeling naar geleide en gebonden modes in de nanostructuur. Verder kunnen de optische eigenschappen van de structuur sterke polarisatieafhankelijkheid hebben, vanwege de anisotropie van de basiselementen. Het proefschrift bestaat uit drie delen, waarin deze effecten worden bestudeerd voor verschillende soorten periodieke nanostructuren.

Het eerste deel (hoofdstukken 2–4) behandelt zogenaamde fotonisch kristalplakken. Deze plakken, die tenminste één golfgeleidermode toestaan, bestaan uit een materiaal met een hoge brekingsindex, dat geperforeerd is met een gatenrooster. Hoofdstuk 2 beschrijft de reflectie van zulke plakken als functie van de golflengte. De spectra bestaan uit een langzaam veranderende achtergrond met daarop een aantal asymmetrische resonanties. De spectrale vorm van de resonanties kan worden verklaard met een Fano model. In dit model zijn er twee bijdragen aan het reflectiespectrum: een directe bijdrage, waarin licht wordt gereflecteerd door Fresnelreflectie van de gelaagde structuur, en een resonante bijdrage, die wordt veroorzaakt door koppeling aan een mode van de golfgeleider. Om de metingen ook kwantitatief te kunnen beschrijven, is het nodig verlies mee te nemen in het model. Dit kan door het toevoegen van een extra verlieskanaal. Het uiteindelijke model heeft drie vrije parameters: de resonantiefrequentie, de levensduur van de golfgeleidermode, en een parameter

die het verlies beschrijft. Om de resonantiefrequenties te kunnen voorspellen, wordt een golfgeleidermodel beschreven dat een effectieve brekingsindex voor de dielectrische plak gebruikt. Numerieke berekeningen laten zien dat resonanties verdwijnen als de brekingsindex van het substraat onder de plak wordt verhoogd. Zodra de brekingsindex van het substraat groter wordt dan de fase-index van de mode van de golfgeleider, is de mode niet meer gebonden aan de dielectrische plak, en verdwijnt de resonantie.

De asymmetrie van de spectrale vorm van de resonantie wordt veroorzaakt door de relatieve fase van de resonante en de directe bijdragen van de reflectie. In hoofdstuk 3 wordt deze fase experimenteel gevariëerd, door de hoek van inval te veranderen. Wanneer de hoek van inval vergroot wordt van 20° tot 80°, over de Brewsterhoek, verandert de spectrale vorm van de resonantie, van asymmetrisch met een staart in het rood, tot symmetrisch, naar asymmetrisch met een staart in het blauw, voor p-gepolariseerd licht. Met het Fano model van hoofdstuk 2 wordt aangetoond dat deze verandering in asymmetrie veroorzaakt wordt door de tekenwissel van de directe reflectie, die plaatsvindt op de Brewsterhoek.

In hoofdstuk 4 wordt een van de resonanties van een fotonisch kristalplak in meer detail bestudeerd. De fotonisch kristalplak wordt belicht met een sterk gefocusseerde bundel van monochromatisch licht, en de reflectie wordt zowel in plaatsruimte als in impulsruimte bekeken. Een polarisatie-analyse van de afbeelding in de impulsruimte leert dat de resonantie veroorzaakt wordt door koppeling aan de TM_0 golfgeleidermode van de plak. In de afbeeldingen in plaatsruimte zijn de directe en resonante bijdragen aan de reflectie ruimtelijk gescheiden. Door deze scheiding kan de afvallengte van de resonantie bepaald worden. Deze lengte variëert met de golflengte, en bedraagt maximaal 7 μm. Samen met de parameters van de resonantie die bepaald zijn uit het reflectiespectrum bij loodrechte inval, kan hieruit een afschatting gemaakt worden van de groepsbrekingsindex $n_{\mathrm{g}} = 2.6$ en de fase-index $n_{\mathrm{eff}} = 1.5$ van de resonante waveguidemode.

Het tweede deel van het proefschrift (hoofdstukken 5–7) bespreekt experimenten met metaalgatenroosters. Deze roosters bestaan uit een optisch dikke goudlaag, geperforeerd met een periodiek gatenrooster. In de transmissiespectra van deze structuren worden resonanties gezien die veroorzaakt worden door koppeling aan oppervlakteplasmonen aan beide zijden van de goudlaag. In hoofdstuk 5 wordt het effect van het plaatsen van diëlektrische pilaren in de gaten besproken. Hoekafhankelijke metingen van het transmissiespectrum worden vergeleken met metingen waarbij de pilaren verwijderd zijn. De pilaren verbeteren de transmissie, en ook de interactie tussen verschillende oppervlak-

teplasmon modes. De verbeterde interactie veroorzaakt een frequentieopsplitsing van 6% voor modes aan de pilaarkant van het gatenrooster.

In hoofdstuk 6 wordt het metaalgatenrooster bedekt met een dunne laag glas. Deze glaslaag vermindert de asymmetrie van de structuur, en zorgt dat de resonanties die veroorzaakt worden door koppeling naar oppervlakteplasmonen aan weerszijden van de structuur ontaard raken, als het glas voldoende dik is. Naast de oppervlakteplasmonresonanties is een aantal scherpe minima waargenomen in de transmissiespectra. Deze minima worden veroorzaakt door koppeling aan modes van de golfgeleider die gevormd wordt door de glaslaag bovenop het gatenrooster. Dit wordt bevestigd door berekeningen van de hoekspreiding van deze golfgeleidermodes.

De overgang van een asymmetrische structuur naar een symmetrische structuur, waar de resonanties ontaard zijn, is het onderwerp van hoofdstuk 7. Deze overgang wordt bestudeerd door het metaalgatenrooster onder te dompelen in vloeistoffen van oplopende brekingsindex. Wanneer het indexcontrast wordt verminderd, wordt een afstoting waargenomen tussen de resonanties aan de glaskant en de vloeistofkant van het metaalgatenrooster. Bovendien wordt de lijnbreedte van een van de resonanties groter ten koste van de andere, zodat er nog maar een resonantie over is als brekingsindex aan beide zijden van het metaal gelijk is. Een theorie van gekoppelde modes met zowel conservatieve (energie-behoudende) als dissiperende koppeling geeft een fenomenologische beschrijving van deze waarnemingen.

Het laatste deel van dit proefschrift beschrijft de absorptie van licht in een supergeleidende enkelfotondetector. Dit type detector bestaat uit een meander van een zeer dun, absorberend materiaal: niobiumnitride. In hoofdstuk 8 wordt de polarisatie-afhankelijkheid van de detectie-efficiëntie van zo'n detector bestudeerd. De structuur van parallelle draden van de detector zorgt voor een sterke polarisatie-afhankelijkheid. Deze is veroorzaakt door een hogere optische absorptie van licht dat parallel aan de draden gepolariseerd is. Een theoretische studie van de absorptie-eigenschappen van de meander, als functie van de laagdikte, laat zien dat de absorptie voor parallel gepolariseerd licht net zo hoog kan zijn als de absorptie van een gesloten laag, zolang het product van vulfractie en laagdikte constant gehouden wordt. Door de detector door het substraat te belichten, kan de berekende absorptie verhoogd worden met een factor gelijk aan de brekingsindex van het substraat.

Het laatste hoofdstuk 9 bespreekt de absorptie van een dunne laag niobiumnitride als functie van de hoek van inval. De gemeten absorptie voor *s*-gepolariseerd licht nadert 100% als de laag wordt belicht op de kritische hoek voor totale interne reflectie. Daarentegen verdwijnt de absorptie voor

p-gepolariseerd licht onder deze condities. Dit effect wordt gebruikt voor een ontwerp voor een enkelfotondetector, die een berekende absorptiecoëfficient van $> 90\%$ heeft voor golflengtes van 700 tot 1600 nm, voor s-polarisatie.

Curriculum Vitæ

Eduard Frans Clemens Driessen

13–10–1979	Born in Utrecht
1991–1997	Grammar school, Christelijk Gymnasium, Utrecht
1997–2005	M.Sc. Applied Physics, Technische Universiteit Delft *Master Thesis: Nonlinear dynamics of the inductive SQUID: prospects for qubit measurement. Advisor: Prof.dr.ir. J. E. Mooij*
2005–2009	Ph.D. Research, Universiteit Leiden *Thesis: Coupling light to periodic nanostructures. Advisors: Prof.dr. J. P. Woerdman and Dr. M. J. A. de Dood*

List of publications

Journal articles

- A. Lupaşcu, E. F. C. Driessen, L. Roschier, C. J. P. M. Harmans, and J. E. Mooij, *High-contrast dispersive readout of a superconducting flux qubit using a nonlinear resonator*, Physical Review Letters **96**, 127003 (2006).

- J. Eroms, L. C. van Schaarenburg, E. F. C. Driessen, J. H. Plantenberg, C. M. Huizinga, R. N. Schouten, A. H. Verbruggen, C. J. P. M. Harmans, and J. E. Mooij, *Low-frequency noise in Josephson junctions for superconducting qubits*, Applied Physics Letters **89**, 122516 (2006).

- E. F. C. Driessen, D. Stolwijk, and M. J. A. de Dood, *Asymmetry reversal in the reflection from a two-dimensional photonic crystal*, Optics Letters **32**, 3137–3139 (2007). (*Chapter 3 of this thesis*)

- M. J. A. de Dood, E. F. C. Driessen, D. Stolwijk, M. P. van Exter, *Observation of coupling between surface plasmons in index-matched hole arrays*, Physical Review B **77**, 115437 (2008). (*Chapter 7 of this thesis*)

- D. Stolwijk, E. F. C. Driessen, M. A. Verschuuren, G. W. 't Hooft, M. P. van Exter, and M. J. A. de Dood, *Enhanced coupling of plasmons in hole arrays with periodic dielectric antennas*, Optics Letters **33**, 363–365 (2008). (*Chapter 5 of this thesis*)

- E. F. C. Driessen and M. J. A. de Dood, *The Perfect Absorber*, Applied Physics Letters **94**, 171109 (2009). (*Chapter 9 of this thesis*). This

Letter was reviewed in *De Pers* of June 24, 2009, and (among other) on the websites of *Science Daily* and *Materials Research Society*.

- E. F. C. Driessen, F. R. Braakman, E. M. Reiger, S. N. Dorenbos, V. Zwiller, and M. J. A. de Dood, *Impedance model for the polarization dependence of NbN superconducting single photon detectors*, The European Physical Journal - Applied Physics 47, 10701 (2009). (*Chapter 8 of this thesis*)

- A. Lupaşcu, P. Bertet, E. F. C. Driessen, C. J. P. M. Harmans, and J. E. Mooij, *One- and two-photon spectroscopy of a flux qubit coupled to a microscopic defect*, submitted to Physical Review Letters, arXiv:0810.0590v1 [cond-mat.supr-con].

Conference proceedings

- M. J. A. de Dood, E. F. C. Driessen, D. Stolwijk, M. P. van Exter, M. A. Verschuuren, and G. W. 't Hooft, *Index matching of surface plasmons*, Proceedings of the SPIE **6987**, 698713 (2008). (*Chapter 6 of this thesis*)

- E. F. C. Driessen, P. O. M. Heemskerk, D. Stolwijk, E. W. J. M. van der Drift, and M. J. A. de Dood, *Asymmetry reversal and waveguide modes in photonic crystal slabs*, Proceedings of the SPIE **6989**, 69890G (2008). (*Chapter 2 of this thesis*)

Patent

- E. F. C. Driessen and M. J. A. de Dood, *Thin film radiation detector*, UK patent application no. 0900534.9, filed 14 January 2009 by Leiden University and FOM foundation. (*Based on Chapter 9 of this thesis*)

Acknowledgements

At the last page of this thesis, there is only one thing left to do. That is to thank everyone who, one way or another, made a contribution to this thesis. It will be impossible to mention all of them here, but a few should not go unnoticed.

The scientific part of this thesis would have never been possible without the technical assistence of, and scientific discussions with many people over the past four years. With the risk of forgetting someone, I'd like to thank (in alphabetical order) Paul Alkemade, Arno van Amersfoort, Koos Benning, Jaap Bij, Jos Disselhorst, Michiel de Dood, Sander Dorenbos, Emile van der Drift, Martin van Exter, Federica Galli, Steven Habraken, Rob van der Heijden, Gert 't Hooft, Paul Junger, Jennifer Kitaygorsky, Teun Klapwijk, Marco van der Krogt, Ewie de Kuyper, Harold Linnartz, Wolfgang Löffler, Hans Mooij, René Overgauw, Elisabeth Reiger, Raymond Schouten, Marc Verschuuren, Marc Zuiddam, Arjen van Zuuk, and Val Zwiller for their technical support, their expertise, and their thoughts about the experiments.

No less important were the students I have been working with, Arthur Zonnenberg, Daniël Stolwijk, Peter Heemskerk, Floris Braakman, and Rick Leijssen. Each one of you, in his own way, made a large contribution to the research we have been doing the last years. This lead, or will lead, Rick, to a fair amount of scientific publications, but more importantly, I enjoyed working together. I learned a lot from working with you, and can just hope to have returned the favor.

The group members of the quantum optics group contributed by the nice atmosphere in the group, and all the discussions (both about physics and about "the rest of the world") we had during coffee and tea breaks. You made the life in between the experiments a lot more agreeable, and for that I thank you. Here, I want to mention explicitly Steven Habraken and Bart-Jan Pors.

Last, but definitely not least, I want to thank my family and friends for the times when I was not occupied in the lab. They made it possible to take my focus away from the lab, and think of things completely different. Most of all I thank Marta, for being understanding whenever I was indecisive on near-future plans, bad-tempered because of an experiment that wouldn't work out, or just telling the same unintelligible and over-detailed story about my research over and over again. Without you, working on this thesis would have been a lot less pleasant, if not impossible.